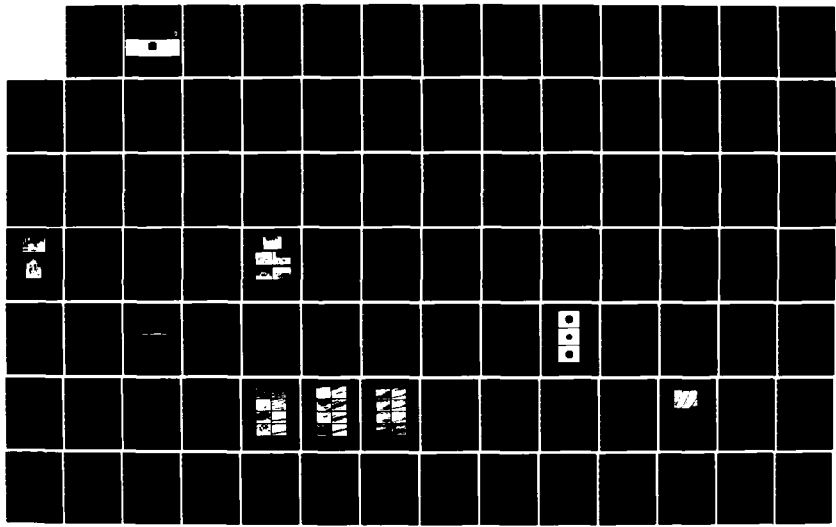
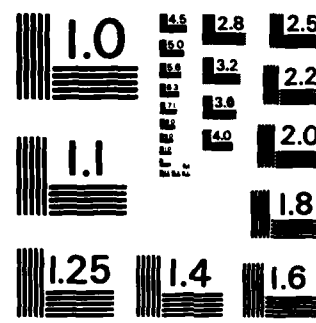


AD-A148 143 THE FUNDAMENTALS OF DISLOCATION TRANSPORT OF HYDROGEN 1/2  
IN BCC IRON(U) CARNEGIE MELLON UNIV PITTSBURGH PA DEPT  
OF METALLURGICAL ENGI.. C HWANG ET AL. OCT 84 TR-18  
UNCLASSIFIED N00014-75-C-0265 F/G 11/6 NL





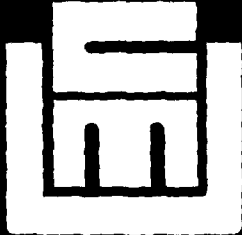
MICROCOPY RESOLUTION TEST CHART  
NATIONAL BUREAU OF STANDARDS-1963-A

AD-A148 143

(1)

APPROVED FOR PUBLICATION  
RELEASE DIST. UNLIMITED

DTIC  
ELECTED  
NOV 29 1984  
S E D



Carnegie-Mellon University  
PITTSBURGH, PENNSYLVANIA

CARNEGIE INSTITUTE OF TECHNOLOGY  
DEPARTMENT OF METALLURGICAL ENGINEERING  
AND MATERIALS SCIENCE

DTIC FILE COPY

|  |
|--|
| DISTRIBUTION STATEMENT A                               |
| Approved for public release;<br>Distribution Unlimited |

84 11 14 164

Carnegie-Mellon University  
Report Number 036-099-18

Technical Report No. 18

to

Office of Naval Research under  
Contract N00014-75-C-0265, NR 036-099 (C-MJ)

The Fundamentals of  
Dislocation Transport of Hydrogen  
in BCC Iron

by

Cherngye Hwang  
Dept. of Metallurgical Engineering & Materials Science  
Carnegie-Mellon University  
Pittsburgh, PA 15213

Submitted in partial fulfillment of the requirements for the degree  
of Doctor of Philosophy at Carnegie-Mellon University



APPROVED FOR PUBLIC  
RELEASE DIST N UNLIMITED

|                    |                          |
|--------------------|--------------------------|
| Accession For      |                          |
| NTIS GRA&I         | <input type="checkbox"/> |
| DTIC TAB           | <input type="checkbox"/> |
| Unannounced        | <input type="checkbox"/> |
| Justification      | <input type="checkbox"/> |
| By                 |                          |
| Distribution/      |                          |
| Availability Codes |                          |
| Dist               | AVAIL and/or<br>Special  |
| A-1                |                          |

October 1984

Distribution of this document is unlimited  
This work was sponsored by the Metallurgy Branch of the  
Office of Naval Research

DTIC  
ELECTRONIC  
S E NOV 20 1984

|  |  |
|--|--|
| DISTRIBUTION STATEMENT A                               |  |
| Approved for public release;<br>Distribution Unlimited |  |

# **THE FUNDAMENTALS OF DISLOCATION TRANSPORT OF HYDROGEN IN BCC IRON**

by  
**Cherngye Hwang**

Department of Metallurgical Engineering  
and Materials Science  
Carnegie-Mellon University  
Pittsburgh, Pennsylvania 15213  
September, 1984

Submitted in partial fulfillment of the requirements for the degree  
of Doctor of Philosophy at Carnegie-Mellon University

## Table of Contents

|  |           |
|--|-----------|
| <b>1. Introduction</b>   | <b>1</b>  |
| <b>2. Literature Review</b>  | <b>5</b>  |
| 2.1. Hydrogen Transport in Iron  | 5         |
| 2.2. Dislocation Dynamics in BCC Iron Crystals                                 | 13        |
| 2.3. Hydrogen Effect on Dislocation Dynamics in BCC Iron                       | 19        |
| <b>3. Research Objectives and Experimental Approaches</b>                      | <b>22</b> |
| <b>4. EXPERIMENTAL PROCEDURES</b>  | <b>24</b> |
| 4.1. Overview  | 24        |
| 4.2. Composition and Heat Treatment of Materials                               | 24        |
| 4.2.1. Single Crystal Material   | 24        |
| 4.2.2. Polycrystalline Material  | 25        |
| 4.3. Single Crystal Orientation Determination                                  | 25        |
| 4.4. Straining Permeation Test   | 27        |
| 4.4.1. Permeation Apparatus  | 27        |
| 4.4.1.1. Overview  | 27        |
| 4.4.1.2. Electrochemical Cells   | 31        |
| 4.4.2. Tensile Straining   | 35        |
| 4.4.3. Recording   | 39        |
| 4.5. Straining Permeation Test Procedures                                      | 43        |
| 4.5.1. Straining after Obtaining A Steady State Permeation Flux                | 44        |
| 4.5.2. Straining Prior to Starting the Permeation Test                         | 45        |
| 4.6. Supersaturation Study   | 47        |
| <b>5. RESULTS AND DISCUSSION</b>   | <b>50</b> |
| 5.1. Single Crystal Orientation Determination                                  | 50        |
| 5.1.1. Slip System Determination   | 58        |
| 5.2. Possible Surface Effects on Straining Permeation Test                     | 65        |
| 5.3. Straining Permeation Tests for Single Crystals                            | 69        |
| 5.3.1. Qualitative Description of Straining Permeation and Flux Phenomena      | 70        |
| 5.3.2. Quantitative Analyses   | 78        |
| 5.3.2.1. Data Analyses Techniques  | 80        |
| 5.3.2.2. Effect of Strain Rate   | 87        |
| 5.3.2.3. Effect of Hydrogen Concentration                                      | 97        |
| 5.3.2.4. Effect of Temperature   | 98        |
| 5.3.2.5. Summary   | 100       |
| 5.3.2.6. Trapping Effect   | 101       |
| 5.4. Straining Permeation Tests for Polycrystalline Specimens                  | 103       |
| 5.4.1. Hydrogen Flux Behavior during Straining                                 | 103       |
| 5.4.2. Microstructural Effects on the Apparent Diffusivity of Hydrogen in Iron | 107       |
| 5.4.3. Effectiveness of Hydrogen Transport during Plastic Deformation          | 107       |

|   |     |
|---|-----|
| 5.5. A Descriptive Model for Dislocation Transport of Hydrogen during Plastic Deformation | 112 |
| 5.6. Hydrogen Supersaturation Associated with Dislocation Transport                       | 116 |
| 5.6.1. Evidence by Transmission Electron Microscopy                                       | 116 |
| 5.6.2. The Morphology of Cracks Induced by Hydrogen Supersaturation                       | 127 |
| 5.6.2.1. Cracks Induced by Cathodic Hydrogen Charging                                     | 128 |
| 5.6.2.2. Cracks induced by Combined Straining and Hydrogen Charging                       | 128 |
| 6. Conclusion   | 135 |
| 7. Recommendations for Future Work  | 139 |
| 8. References   | 142 |
| Appendix A. Model Calculation and Computer Programs                                       | 154 |
| Appendix B. Dislocation Line Direction and Burgers Vector Orientation Determination       | 162 |
| B.1. Dislocation Line Direction Determination   | 162 |
| B.2. Burgers Vector Determination   | 164 |

## List of Figures

|                     |   |    |
|---------------------|---|----|
| <b>Figure 2-1:</b>  | The maximum resolved shear stress slip systems at different tensile axis orientation, predicted by Schmid's factor, using {112} and {110} as slip planes and <111> as slip direction.   | 15 |
| <b>Figure 2-2:</b>  | Orientation dependence of stress-strain curves of iron single crystals at 298 K.(133)   | 16 |
| <b>Figure 2-3:</b>  | Effects of deformation temperature on the stress-strain curves of iron crystals.(128)   | 18 |
| <b>Figure 4-1:</b>  | The angular relationship of standard Laue X-ray diffraction method.(172)  | 26 |
| <b>Figure 4-2:</b>  | The overall straining permeation test set-up for this study.  | 28 |
| <b>Figure 4-3:</b>  | The flux versus time curve for permeation test; the breakthrough time $t_b$ and lag time $t_{Lag}$ are defined in the figure.   | 29 |
| <b>Figure 4-4:</b>  | The electrochemical cells used for the straining permeation test in this study.   | 32 |
| <b>Figure 4-5:</b>  | The single crystal specimen configuration used in the straining permeation test. A: tensile specimen holder, B: single crystal. The exposed area on the single crystal during test, $0.32 \text{ cm}^2$ , is indicated in the figure. The hydrogen flux reported in this thesis is a direct measurement from this constant area for the single crystal tests. | 34 |
| <b>Figure 4-6:</b>  | The block diagram for slow strain rate tensile testing device designed and constructed in this study.   | 37 |
| <b>Figure 4-7:</b>  | The special grip system designed and used in this study. Note that the electric insulation of specimen from the entire machine is provided by the lava tube in the pin-load holes.  | 38 |
| <b>Figure 4-8:</b>  | The response of strip chart recorder (Omniscribe model #B5217-5) for various input frequencies of identical saw-tooth signals. The true signal is shown in the 0.01 Hz response.  | 40 |
| <b>Figure 4-9:</b>  | Comparison of the identical hydrogen flux recorded by computer and strip chart recorder for different periods of hydrogen flux during the straining permeation test. (a) background, (b) hydrogen flux in the absence of straining, (c) hydrogen flux during straining.   | 41 |
| <b>Figure 4-10:</b> | The background fluctuation range for the single crystal straining permeation test. This also represents the resolution for quantitative analysis of hydrogen flux by dislocation transport. Note: $1.0E10 \text{ atom H/sec} = 1.0 \times 10^{10} \text{ atom H/sec}$ .   | 44 |

|                     |  |    |
|---------------------|--|----|
| <b>Figure 4-11:</b> | A test procedure for consecutive straining and static permeation tests.  | 46 |
| <b>Figure 5-1:</b>  | Laue patterns for three crystals used in this study. The numbered spots were indexed in the Figure 5-2.  | 51 |
| <b>Figure 5-2:</b>  | The stereographic projections deduced from Laue pattern shown in Figure 5-1.   | 52 |
| <b>Figure 5-3:</b>  | Stereographic projections plotted by a computer for three identical zone axes as those in Figure 5-2.  | 55 |
| <b>Figure 5-4:</b>  | Three crystal orientations used in this study, with the predicted primary slip systems. (a) screw orientation, (b) mixed orientation, (c) edge orientation.  | 59 |
| <b>Figure 5-5:</b>  | Single crystal specimen used to study the slip system.   | 60 |
| <b>Figure 5-6:</b>  | Single crystal surfaces showing slip traces at different total strain for "screw orientation" crystal.   | 61 |
| <b>Figure 5-7:</b>  | Single crystal surfaces showing slip traces at different total strain for "mixed orientation" crystal.   | 62 |
| <b>Figure 5-8:</b>  | Single crystal surfaces showing slip traces at different total strain for "edge orientation" crystal.  | 63 |
| <b>Figure 5-9:</b>  | TEM bright field images showing dislocation structure in two differently oriented single crystals after about 5% strain. The majority of dislocations in both cases are screw in character. (a) screw orientation, (b) edge orientation.   | 66 |
| <b>Figure 5-10:</b> | Possible dislocation loop configuration on the primary slip plane for differently oriented single crystals.  | 67 |
| <b>Figure 5-11:</b> | The anodic surface effect due to dynamical straining of single crystal and polycrystalline iron at various strain rates.   | 68 |
| <b>Figure 5-12:</b> | SEM micrograph accompanied with X-ray of Pd signal showing the rupture of Pd layers after straining.   | 69 |
| <b>Figure 5-13:</b> | Typical changes of steady state hydrogen flux due to concurrent plastic deformation for screw orientation single crystal.  | 71 |
| <b>Figure 5-14:</b> | Typical changes of steady state hydrogen flux due to concurrent plastic deformation for mixed orientation single crystal.  | 76 |
| <b>Figure 5-15:</b> | Typical changes of steady state hydrogen flux due to concurrent plastic deformation for edge orientation single crystal.   | 77 |
| <b>Figure 5-16:</b> | Curve stripping method used in separating hydrogen flux transported by dislocations from the total flux.   | 82 |
| <b>Figure 5-17:</b> | The hydrogen flux behavior showing the range of trapping effect during straining permeation tests at different strain rates. (a) $\epsilon = 8 \times 10^{-6} \text{ sec}^{-1}$ , (b) $\epsilon = 8 \times 10^{-7} \text{ sec}^{-1}$ , (c) $\epsilon = 8 \times 10^{-8} \text{ sec}^{-1}$ , (d) $\epsilon = 1.6 \times 10^{-8} \text{ sec}^{-1}$ . | 83 |
| <b>Figure 5-18:</b> | Hydrogen flux behavior showing the dislocation transport effect during straining permeation tests at different conditions indicated by the associated codes. Note: $1.0E10 \text{ atom H/sec} = 1.0 \times 10^{10} \text{ atom H/sec}$ .   | 85 |
| <b>Figure 5-19:</b> | Average hydrogen transport rates based on per unit time for various tests indicated by special codes. Note: $1.0E10 \text{ atom H/sec} = 1.0 \times 10^{10} \text{ atom H/sec}$ .  | 88 |

|                     |  |     |
|---------------------|--|-----|
| <b>Figure 5-20:</b> | Average hydrogen transport rates based on per unit strain for various tests indicated by special codes.<br>Note: $1.0E10$ atom H/sec = $1.0 \times 10^{10}$ atom H/sec.  | 90  |
| <b>Figure 5-21:</b> | Strain rate effect on hydrogen transport rates by different dislocation types for different testing conditions. (a) screw dislocation, (b) mixed dislocation, (c) edge dislocation. Note: $1.0E10$ atom H/sec = $1.0 \times 10^{10}$ atom H/sec. | 91  |
| <b>Figure 5-22:</b> | Hydrogen concentration in the dislocation core at steady state as a function of velocity.(95)  | 94  |
| <b>Figure 5-23:</b> | The lattice hydrogen concentration effect on hydrogen transport rates by different dislocations. Note: $1.0E10$ atom H/sec = $1.0 \times 10^{10}$ atom H/sec.  | 99  |
| <b>Figure 5-24:</b> | A double slip crystal orientation used to study the trapping effect.   | 102 |
| <b>Figure 5-25:</b> | The trapping effect due to strain induced sessile dislocations for single crystals oriented for single and multiple slips.   | 103 |
| <b>Figure 5-26:</b> | Changes in the steady state permeation flux of hydrogen from the un-strained state due to concurrent plastic deformation.  | 104 |
| <b>Figure 5-27:</b> | Strain rate dependence of normalized flux with respect to the steady state flux prior to straining. The time shown is the period after the cessation of straining.   | 105 |
| <b>Figure 5-28:</b> | The microstructural change sequence as a function of tensile strain.   | 108 |
| <b>Figure 5-29:</b> | The apparent diffusivity in the absence of straining, as a function of tensile strain.   | 109 |
| <b>Figure 5-30:</b> | Strain rate dependence of the apparent hydrogen diffusivity ratio with and without concurrent plastic deformation.   | 110 |
| <b>Figure 5-31:</b> | The modified hydrogen flux profile for three different modelling conditions as indicated.  | 115 |
| <b>Figure 5-32:</b> | Dislocation structure in the hydrogen charged region of a "screw dislocation" single crystal at about 5% strain.   | 117 |
| <b>Figure 5-33:</b> | Dislocation structure in the hydrogen free region of the same single crystal in Figure 5-32.   | 118 |
| <b>Figure 5-34:</b> | (a) SEM micrograph of silicon rich spherical particle. (b) Energy dispersive spectrum (EDS) of the particle in (a).  | 119 |
| <b>Figure 5-35:</b> | A collection of the dislocation structures around spherical particles found in the hydrogen free region of a "screw orientation" single crystal at about 5% total strain.  | 121 |
| <b>Figure 5-36:</b> | A collection of the dislocation structures around spherical particles found in the hydrogen charged region of the same single crystal in Figure 5-35.  | 122 |
| <b>Figure 5-37:</b> | A sketch of dislocations on different slip systems participating in the strain localization structure. See Appendix B for detailed analyses.   | 124 |
| <b>Figure 5-38:</b> | The orientation relationships between the strain localization direction on the (110) plane and the tensile axis.   | 125 |

- Figure 5-39:** Light micrograph of surface blisters on a (110) plane, 129 resulting from hydrogen charging.
- Figure 5-40:** Internal cracks underneath the surface blisters shown in 130 Figure 5-39.
- Figure 5-41:** Internal cracks on a (001) plane of the same crystal in 131 Figure 5-40 resulting from hydrogen charging.
- Figure 5-42:** A sketch of hydrogen-charging induced surface blisters 132 and internal cracks, with the proper indexed orientation relationship.
- Figure 5-43:** The early stage of the (110) surface blister formation 133 of a SET single crystal specimen.
- Figure A-1:** A small cube within the specimen showing the 154 constituents of its total hydrogen concentration.
- Figure B-1:** TEM bright field image of dislocation tangled structure 163 associated with spherical particles. (a)  $\langle\bar{1}\bar{1}0\rangle$  zone axis, (b)  $\langle\bar{1}\bar{1}1\rangle$  zone axis.
- Figure B-2:** TEM bright field image of dislocation tangled structure 166 associated with spherical particles. (a)  $\vec{g} = [1\bar{1}0]$ , (b)  $\vec{g} = [011]$ , (c)  $\vec{g} = [101]$

## List of Tables

|                   |  |     |
|-------------------|--|-----|
| <b>Table 2-1:</b> | Penetration depth ratios for $(Dt)^{1/2}$ versus dislocation sweep-in transport of hydrogen in iron and nickel base alloys.(94)  | 10  |
| <b>Table 2-2:</b> | Values of the time constant, $\tau$ , in seconds, as a function of the binding, $E_B$ , and the hydrogen diffusivity, $D_H$ .(105)   | 11  |
| <b>Table 2-3:</b> | Trapping energy of various possible traps in iron.(24)   | 12  |
| <b>Table 5-1:</b> | Summary of different crystal orientation used in this study.   | 50  |
| <b>Table 5-2:</b> | Temperature range (K) below which the cross slip of screw dislocations is unlikely in bcc crystals.  | 64  |
| <b>Table 5-3:</b> | An estimation of average dislocation velocities and mobile dislocation densities for three consecutive straining permeation tests  | 73  |
| <b>Table 5-4:</b> | Summary of straining permeation tests, giving the relation between test condition and designated code.   | 78  |
| <b>Table 5-5:</b> | Nominal strain rates measured from LVDT for all the tests conducted in this part of study.   | 79  |
| <b>Table 5-6:</b> | A comparison of dislocation velocity and kink velocity at different strain rates assuming a constant mobile dislocation density of $10^6 \text{ cm}/\text{cm}^3$ .   | 95  |
| <b>Table 5-7:</b> | Approximate break-through time for significant dislocation transport of hydrogen flux.   | 96  |
| <b>Table 5-8:</b> | Steady state lattice hydrogen diffusion fluxes and strains before each straining permeation test.  | 97  |
| <b>Table 5-9:</b> | Temperature dependence of hydrogen transport rate by screw and edge dislocations. The strain rate used is $1 \times 10^{-5} \text{ sec}^{-1}$ and the charging current density is $0.5 \text{ mA}/\text{cm}^2$ . | 100 |
| <b>Table B-1:</b> | Three different slip systems identified in the dislocation tangled structure   | 165 |

## ACKNOWLEDGEMENTS

The author would like to acknowledge the help and guidance of many people who have made numerous contributions to this thesis, most notably his thesis advisor, Professor I.M. Bernstein. Thanks are due also to Professors A.W. Thompson, J.K. Tien and W.C. Johnson, who provided many helpful suggestions. The helpful critiques provided by Prof. W.W. Mullins, S. Mahajan and F. Prinz were also appreciated.

I would like to thank Dr. W.Y. Choo, Mr. G.S. Frankel and Dr. M. Hashimoto for many stimulating discussions through the course of this study. I would also like to acknowledge many helpful conversations with Drs. D. Nguyen, Federico G.-Solana, Professors H. Dong, X. Tang. Special thanks are due to Dr. M.F. Stevens, who helped in many ways, and always managed to keep things in their proper perspective.

I would like to thank the Office of Naval Research for its financial support of this research, and U.S. Steel Corp. for providing the single crystal specimens.

I would like to thank G. Biddle and P. Huckestein for machining various testing equipments, and R. Miller for purchasing assistance. Also, the help of E. Danielson in designing the slow strain rate testing device and electrochemical cells is greatly appreciated. Thanks are also due to Pete Kullen for photographic assistance.

The support and concern of my family helped tremendously in the completion of this endeavor. I especially would like to thank my parents for their constant encouragement throughout my academic career, and their love and care throughout my life. My family has truly been a great help.

I would finally like to thank my wife, Meiyun; without her sacrificial help and love, this thesis could never be accomplished. I also like to thank my daughter, Jennifer, for her patience and smile.

## ABSTRACT

The detailed characteristics of hydrogen transport by mobile dislocations during plastic deformation in bcc single crystal and polycrystal pure iron has been studied. Single crystals with a proper combination of surface orientation and tensile axis were used to separately study the hydrogen transport rates by screw, edge and mixed dislocations. This study was carried out experimentally through the use of a pair of sophisticated electrochemical cells incorporated with a specially constructed slow strain rate tensile testing device. The experimental uncertainties involved in the measurement of hydrogen flux have also been carefully analyzed and reduced to a minimum, so that the data obtained were able to be accurately interpreted. Parameters such as strain rate, lattice hydrogen concentration and temperature were varied to systematically study their functional relationships to dislocation transport.

It was found that qualitatively the hydrogen flux transported by dislocations intimately reflects the dislocation egression on the monitored crystal surface. Quantitatively, the hydrogen transport rate increases with decreasing strain rate; the edge kinks appeared to possess the greatest capability of transporting hydrogen at the lowest strain rate ( $1.6 \times 10^{-8} \text{ sec}^{-1}$ ) employed. In addition, an insignificant effect of lattice hydrogen concentration on dislocation transport was observed, and was attributed to the kinetic nature of this transport process where equilibrium between hydrogen concentration on the dislocations and in the lattice is unlikely to be established. A minimal temperature effect on dislocation transport rate was also observed within a narrow temperature range, from  $12^\circ\text{C}$  to  $78^\circ\text{C}$ , consistent with the expectation that the extra thermal energy provided by increased temperature was too small to alter the interaction between hydrogen and mobile dislocations.

The competition between hydrogen transport by mobile dislocations and the trapping effect by newly generated sessile dislocations was studied, primarily by using polycrystal iron specimens. A simple model describing this combined effect of trapping and transport was also developed, which showed that transport can co-exist with the trapping even at the early strain history of the material when the dislocation multiplication rate is very high. However, the combined flux indicates that at small strains the trapping effect is dominant.

Dislocation structures formed with and without the presence of dislocation transported hydrogen in single crystals were also examined by transmission

electron microscopy. The former case was found to greatly enhance the tendency for strain localization associated with inclusion particles, which are believed to be strong hydrogen traps. Dislocation structures associated with this strain localization phenomenon were analyzed; the origin of this localized strain was then studied and related to the role of hydrogen supersaturation due to dislocation transport. The consequent crack initiation associated with the interaction of hydrogen during straining was also studied. The complex and as yet incompletely understood interrelationships between dislocation transport of hydrogen, hydrogen supersaturation, strain localization and hydrogen-induced crack initiation were presented and discussed.

## Chapter 1 Introduction

Hydrogen embrittlement has long been recognized as being a major factor in the premature failure of various materials, and considerable understanding of this phenomenology of the process has been achieved in recent years. Major reasons for the wide interest in hydrogen effects in materials stems in part from the variety of environments from which hydrogen may be absorbed by a metal host and the subsequent degradation of most important alloy systems.

Hydrogen may enter a metal from the gas phase through surface dissociation or it may be absorbed from the surface as the result of cathodic half-cell reactions accompanying electrochemical corrosion. Consequently, hydrogen may embrittle a material by causing a fracture mode change (i.e. from ductile to brittle) or it may affect the plasticity of the material without causing a fracture mode change(1, 2). Both manifestations have been observed in iron alloys and extensive research has been conducted in an attempt to clarify the different responses. However, the hydrogen effect on fracture mechanisms is still poorly understood and while many different theories have been proposed, such as high pressure molecular hydrogen bubble formation(3-6), surface adsorption effects(7-9), lattice decohesion mechanisms(10-12), and plastic deformation effects(13-21), no consensus or agreement currently exists. Plausibly, it is generally believed that one or more of these proposed different mechanism could operate simultaneously to cause the final fracture; under certain circumstance a particular mechanism may be dominant, whereas for other conditions, a different mechanism controls.

Despite the controversy concerning embrittlement mechanisms, a great deal of information relevant to the kinetics of embrittlement in iron and steels has still been established. One remarkable and telling kinetic characteristic is that the sensitivity to hydrogen embrittlement depends strongly on strain rate and temperature(22). It is widely believed that the observation of a ductility

minimum usually near room temperature and of an inverse dependence of ductility on strain rate, reflects the importance of hydrogen transport kinetics to either crack initiation sites or growing cracks. These effects are explained as follows: a common suggestion is that a critical hydrogen concentration exists for embrittlement(23), which may depend on the local stress. At low temperature the hydrogen mobility is limited and the critical hydrogen concentration cannot be achieved due to insufficient time. At high temperatures, the required critical hydrogen concentration at failure sites cannot be reached due to the lost trapping ability of hydrogen at failure sites, because of its additional thermal energy. Similarly, at high strain rates, the transport of hydrogen to critical locations is not sufficiently rapid to allow a critical concentration of hydrogen to be maintained at the growing crack and the hydrogen effect is again not significant. From these somewhat unusual dependencies of hydrogen on temperature and strain rate, it is fair to conclude that hydrogen embrittlement is often dominated by kinetic processes and therefore that the understanding of hydrogen transport kinetics is of great and perhaps paramount importance in developing a successful understanding of the multiplicity of hydrogen effects in materials.

Among various operative transport modes, the possible occurrence and mechanism of transport of hydrogen by mobile dislocations has recently drawn special attention, both because of recent theoretical advances and of experimental observations that cannot be simply rationalized if hydrogen moved only by lattice diffusion(24). A transport mode of this type is of importance to hydrogen embrittlement processes because it potentially provides a means by which hydrogen can affect properties in materials where diffusion and/or solubility is very low, or in a hydrogen gas atmosphere test for which equilibrium concentrations are usually very small, except at very high pressure.

Numerous research efforts have concentrated on this kinetic-based transport phenomenon; experimental observations found in support of the occurrence and importance of dislocation transport can be summarized as follows:

- Accelerated hydrogen uptake occurred in the plastically deformed gauge length of stainless steel, even though no significant lattice diffusion is occurring(25-30).

- In ductile fracture processes, hydrogen is thought to be transported to and enriched at microvoids or inclusions, leading to a change in the rate of void nucleation and growth, and thus to more rapid ductile rupture(31-50).
- The enhanced penetration of hydrogen due to dislocation transport has been suggested as an essential element in explaining the accelerated fatigue crack growth rates in hydrogen(51-57).
- Dislocation transport may also be involved when hydrogen participates in stress corrosion cracking, particularly when the cracking rates exceed either lattice diffusion rate or local dissolution kinetics(37).

Therefore, it is clear that an understanding and establishment of the occurrence of dislocation transport of hydrogen can provide an important component in attempts to rationalize the validity of various hydrogen embrittlement phenomena. It should also be noted that fast transport of hydrogen to innocuous hydrogen sinks may also result in a decrease in the lattice hydrogen concentration(36), thus reducing the susceptibility of materials to hydrogen embrittlement.

As listed above, while there are various experimental implications associated with the occurrence of dislocation transport and its associated mechanisms, little work has been published on the manifestation of the phenomenon, and even less quantitative details. This thesis intends to improve the understanding of the possible occurrence of this process in iron, primarily by studying the dislocation transport behavior of hydrogen in single crystals, where the proper selection of tensile orientation and crystal surface plane will allow a clear separation of the hydrogen carrying ability of edge and screw dislocation during straining (plastic deformation), and thus provide a means to study enhanced transport by each dislocation type.

Additionally, recent studies of the processes involved in hydrogen induced fracture have also suggested that one of the major effects of hydrogen absorption is the promotion of strain localization(40, 58-60). The evidence for hydrogen enhanced strain localization, including cracks following characteristic slip traces(58) and multiple Luders band formation(61), implies that interaction between dislocations and hydrogen can play an important role in strain localization processes. Dynamic high voltage electron microscopy studies(62) of fracture in an in situ hydrogen environment also reveals that the

major effect of hydrogen is the redistribution of the slip into a more localized plastic zone in contrast to the more diffuse and broader plastic zone formed during identical tests in vacuum. Fundamental understanding of this phenomenon has been limited both experimentally and theoretically, although there are some intriguing preliminary experimental results. For example, the occurrence of TiC particle-associated hydrogen induced localized micro-twinning formation in a particular crystallographic orientation(63), suggests hydrogen induced localization of this phenomenon. More pointedly, the present study revealed that dislocation formation around strong hydrogen traps can be very localized and further the operating slip system(s) in the vicinity of the traps can be very different from that of the surrounding matrix. These observations provided the opportunity to explore the possible origins of strain localization whose occurrence could lead to the final hydrogen-assisted fracture process. The possibilities explored included pressurization due to hydrogen gas enrichment in internal traps such as microvoids or inclusions, or an enhanced transient concentration build-up at such traps. The occurrence of either could either modify the local stress field thus altering the final dislocation morphology or could directly affect the Peierls stress for the operation of different slip systems.

## Chapter 2 Literature Review

In an attempt to review the literature relevant to this study, it is necessary to address two relatively independent fields: hydrogen transport phenomena in iron and the dynamical movement of various types of dislocations in pure iron. The plan of this chapter is to selectively examine the published research in these areas, but relate these to the focus of this research, the interaction between hydrogen and dislocations during plastic deformation.

In the following, the hydrogen transport through iron lattice, particularly by dislocation sweeping will first be reviewed and the experimental implications and theoretical developments of this phenomenon summarized, and the possibility of consequent hydrogen supersaturation then discussed. Further, to correlate the hydrogen transport and dislocation behavior, dislocation dynamical behavior with and without the presence of hydrogen in iron will then be presented.

### 2.1. Hydrogen Transport in Iron

It has been well accepted that the static transport of hydrogen through crystalline materials occurs primarily by lattice diffusion(64), with a possible contribution(65) from either grain boundary diffusion or from other short-circuit diffusion paths. The effect of crystal defects such as microvoids, inclusions, grain boundaries, dislocations, on such transport mechanisms has been widely studied(66-77), and these defects, designated as "traps", have been found to invariably delay the measured hydrogen diffusion rate.

It has also been discussed extensively in a number of reviews (78-79), and shown experimentally(25,80), that when a crystal contains both dislocations and hydrogen interstitial atoms, an interaction or binding between the two can

occur, fundamentally because the total free energy of the crystal will be lowered when hydrogen atoms migrate to the expanded region of edge dislocations or to the non-dilatational stress fields of screw dislocations(79). In either case, dislocation atmospheres could form and during subsequent plastic deformation, the hydrogen atoms associated with the dislocations can be dragged or swept by moving dislocation, but only for the proper combination of temperature and strain rate(24,81). The atmosphere can then be "stripped off" and deposited at microstructural imperfections such as grain boundaries, inclusions, microvoids etc.(66); and if these locations are the critical precursor centers for hydrogen cracking or fracture then an enhanced susceptibility to embrittlement could occur(82).

In support of the above scenario and considerations, there are a number of studies that can be cited. Bastien and Azou(83-84) first suggested that dislocations could transport a hydrogen atmosphere at rates far faster than the lattice diffusion rate and that this hydrogen could be trapped in voids, possibly leading to the development of internal pressure and an enhancement of failure. This idea was experimentally supported twenty five years later by Donovan(80,85), who showed that concurrent plastic deformation increased the tritium release rate from the surface of Armco iron by a factor of four. Using an external hydrogen atmosphere, Louthan et al(25) suggested that for otherwise equivalent conditions, tritium penetrated much more deeply into stainless steel during concurrent plastic deformation than for elastic deformation. Besides the interpretation of hydrogen being transported by moving dislocations, they also considered the possibility that lattice hydrogen uptake was enhanced by the formation of clean (oxide free) surface steps due to the associated plastic deformation. By studying different surface finishes they found that the enhanced surface entry was not significant, providing stronger support for the former possibility that dislocation transport of hydrogen can indeed occur during plastic deformation.

An even more direct measurement of enhanced diffusivity of hydrogen during concurrent plastic deformation was suggested by the results of Kurkela and Latanision(86-87) using electrochemical permeation techniques. They found an increase of five orders of magnitude in the effective hydrogen diffusivity at room temperature for nickel alloys during plastic deformation compared to static measurements in the same alloys. However, these finding have recently

been questioned by Otsuka et al(88) and by Johnson(89), who suggested instead that current-induced Joule heating of the sample could also give rise to a similar flux behavior, whose increase would now be attributable to a temperature rise rather than to any enhanced dislocation transport of hydrogen(86-87). Joule heating originates from the charging current passing through the solution and specimen and is proportional to  $I^2R$ ; where I is the charging current and R is the total combined resistance of solution and specimen. Since the diffusivity and solubility of hydrogen in metal are both very sensitive to temperature, a small increase in temperature could cause a detectable and often large increase in the hydrogen permeability in metal. Joule heating was considered to be a potential problem in Kurkela and Latanisions' experiments because the charging current density used was very high ( $>50$  mA/cm<sup>2</sup>), resulting in an increase in hydrogen flux comparable to the normally observed flux ( $<0.2\mu\text{A}/\text{cm}^2$ ) in nickel at constant room temperature(86). Thus while the observed flux increase was attributed by Kurkela and Latanision to dislocation transport, it was more rationally explainable by the temperature dependence of the hydrogen permeability.

Lin et al (89) and Frankel et al(90) have carried out additional permeation tests on nickel and have verified the presence of a Joule heating ambiguity confirming that Joule heating could indeed be a problem depending on the exact nature of the experimental set-up (e.g. vertical cells vs. horizontal cells) and the magnitude of the charging current density. In fact, by using smaller charging current densities and by circulating the electrolytes during the test to reduce local Joule heating problems, Frankel et al(91) have shown that in single crystal nickel specimens dislocation transport of hydrogen appears quite likely, although the magnitude of the observed effect is much smaller than previously reported.

In a set of preliminary experiments for the present work, we have conducted straining permeation tests(92), which supported the occurrence of dislocation transport of hydrogen in bcc polycrystalline iron. Hashimoto and Latanision(93) recently carried out a detailed calculation of the transport phenomenon of hydrogen during plastic deformation in Armco iron and showed that while the trapping effect is dominant during plastic deformation, enhanced transport can co-exist. They analyzed the results using a modified McNabb and Foster's relation(71), taking into account the mobile dislocation activities during

plastic deformation and found, in agreement with others(81,94), that when the dislocation multiplication rate is slow and hence trapping effects are less important, dislocation transport of hydrogen can be much more prevalent. Hashimoto(95) has also performed atomistic model calculations based on a modified Yoshinaga and Morozumi's model(96), which uses an imaginary tetragonal interstitial lattice to simulate the interaction between interstitial carbon atoms and dislocations. A computer solution of a set of ordinary differential equations describing the interaction of hydrogen in an array of interstitial sites with hydrogen associated with a moving trap led to the conclusion that hydrogen transport by mobile dislocation is possible and can lead to large supersaturations at near interfacial traps even when the lattice hydrogen concentration is much too low to rationalize the supersaturation. Thus at higher hydrogen concentrations, the importance of dislocation transport may be to sustain a higher hydrogen concentration associated with those dislocations involved in the cracking process, enhancing embrittlement. This could be exacerbated by the dislocation mobility itself being enhanced by the associated hydrogen atmosphere, as experimentally observed by Tabata et al(97) and Kimura et al(98), and theoretically rationalized by Louthan(99).

To completely understand the interrelationships between dislocation transport mechanism and hydrogen enhanced fracture process, a well planned, reliable experimental approach is essential. The experimental method usually used to study dislocation transport of hydrogen is to electrochemically measure the permeation flux passing through a thin specimen during concurrent straining. However, the interpretation of results is complicated by the enormous trapping effect of the rapidly increasing sessile dislocation density during plastic deformation, which could mask any enhanced transport. However, the importance of this transport mechanism to any resultant fracture processes may not be simply connected to the net flux. Instead it could be the transient redistribution(100) of hydrogen within the specimen where crack initiation sites (usually stronger, more irreversible, traps(49,66)) accumulate an enhanced transient concentration build-up. If this exceeds the local critical hydrogen concentration for fracture initiation, an enhanced susceptibility to embrittlement could occur. Although direct experimental evaluations of the occurrence, nature and importance of these kinetic supersaturation concepts have not yet been firmly established, there are a number of theoretical treatments, in particular

the stripping model by Tien et al(81,94,101-102) and the annihilation model by Hirth and Johnson(103-104), which have attempted to examine the consequences of transient build-up and decays in local hydrogen concentrations.

The stripping model considers as a prime assumption, that hydrogen transport by dislocation sweeping can occur to fixed stationary sites (traps). Three rate controlling processes, i.e. adsorption from the input hydrogen atmosphere, grain boundary barrier exchange, and penetration distance were evaluated, and it was shown that since the first two processes are extremely fast, neither free surfaces nor grain boundaries are effective rate controlling barriers to hydrogen transport, and thus dislocation transport itself is rate determining. To determine the maximum depth to which hydrogen could penetrate by dislocation transport, the Boltzmann's equation, viz

$$C = C_0 \cdot \exp(-E_b/kT) \quad (2.1)$$

was used to represent the hydrogen concentration associated with mobile dislocation, and the Einstein-Stokes relation

$$v = M \cdot F = (D_H/kT) \cdot F \quad (2.2)$$

was used to relate the dislocation velocity to the driving force and mobility of hydrogen in the lattice.

In these relations, C is the hydrogen concentration associated with dislocations;  $C_0$  is the nearby lattice hydrogen concentration;  $E_b$  is the bonding energy between hydrogen and a dislocation of a given type; k is the Boltzman constant; T is the absolute temperature; v is the average dislocation velocity; and M is the mobility of hydrogen in lattice, equal to  $D_H/kT$  ( $D_H$  is the lattice hydrogen diffusivity); and F is the driving force acting on the dislocation.

The maximum transport rate was determined from the critical dislocation velocity, defined as the velocity beyond which the hydrogen atmosphere can no longer keep up with the moving dislocation. By using crude, but reasonable numerical data for all the necessary parameters, Tien et al were able to predict that a significant amount of hydrogen could be captured by traps due to dislocation sweeping and that this amount was much larger than the departure rate of hydrogen by diffusion leakage into the surrounding matrix. In such cases, supersaturation of hydrogen can thus occur based totally on kinetic reasons.

As an extension of this model, Tien et al(81) have calculated the penetration distance due to dislocation sweeping as:

$$X_c = V_c * t_p \quad (2.3)$$

where  $V_c$  is average mobile dislocation velocity and  $t_p$  is the duration of plastic deformation. The corresponding penetration distance by lattice diffusion alone is:

$$X_D = 4 * (D_H * t_p)^{1/2} \quad (2.4)$$

where  $D_H$  is the lattice diffusivity of hydrogen atoms.

The ratio,  $X_c/X_D$  can thus be calculated, as shown in Table 2-1 for different alloy systems. It is apparent that except at extremely short times, dislocations can carry hydrogen much more deeply into the material than lattice diffusion can, particularly in iron based alloys. Correspondingly, due to the large difference of hydrogen arrival and departure rates at trap sites, the resultant hydrogen supersaturation at a given trap site can be very high.

Table 2-1: Penetration depth ratios for  $(Dt)^{1/2}$  versus dislocation sweep-in transport of hydrogen in iron and nickel base alloys.(94)

| <u>t(sec)</u>      | <u>f</u> | <u><math>\bar{x}_c/\bar{x}_D</math> Fe-Base</u>         | <u><math>\bar{x}_c/\bar{x}_D</math> Ni-Base</u>          | <u><math>\bar{x}_c/\bar{x}_D</math> Monel</u>           |
|--------------------|----------|---|--|---|
| 1 hr               | 1 CPH    | $2.0 \times 10^5$                                       | $2.0 \times 10^3$  | $6.3 \times 10^3$                                       |
| 60                 | 1 CPM    | $2.6 \times 10^4$                                       | $2.6 \times 10^2$  | $8.2 \times 10^2$                                       |
| 1                  | 1 Hz     | $3.3 \times 10^3$                                       | $3.3 \times 10^1$  | $1.1 \times 10^2$                                       |
| $2 \times 10^{-2}$ | 60 Hz    | $4.3 \times 10^2$                                       | $4.3 \times 10^0$  | $1.4 \times 10^1$                                       |
| $1 \times 10^{-3}$ | 1 kHz    | $1.1 \times 10^2$                                       | $1.1 \times 10^0$  | $3.3 \times 10^0$                                       |
| $1 \times 10^{-4}$ | 10 kHz   | $3.3 \times 10^1$                                       | $3.3 \times 10^{-1}$                                     | $1.1 \times 10^0$                                       |
|                    |          | <u>D    <math>10^{-6} \text{cm}^2/\text{sec}</math></u> | <u>D    <math>10^{-10} \text{cm}^2/\text{sec}</math></u> | <u>D    <math>10^{-9} \text{cm}^2/\text{sec}</math></u> |

In contrast, the annihilation model(103-104) considers that hydrogen is

transported to deposition sites (usually dislocation-dislocation annihilation sites) by dislocation drag and then leakage of the hydrogen occurs from the deposition sites by lattice diffusion. Under the critical assumption of maintaining steady state, the kinetic supersaturation was evaluated from a balance between hydrogen arrival and departure rate, for both internal and external hydrogen sources, and for smooth sections and crack geometries. Having calculated the excess hydrogen concentration at the annihilation site, by equating the arrival rate of hydrogen to the steady state hydrogen diffusion leakage rate from the annihilation site to the external free surface (considered to be the nearest hydrogen sink), they concluded that the excess hydrogen concentration in all cases is very small, ranged from  $10^{-1}$  to  $10^{-5}$  for the term  $(C_1 - C_0)/C_0$ , where  $C_1$  and  $C_0$  are hydrogen concentration at trap and in the lattice respectively, and thus enrichment was unlikely. It is worth noting that the steady state assumption is totally in contrast to the former model, where the arrival rate of hydrogen to the crystal discontinuity can be much greater than the departure rate in the time interval considered, as discussed by Bernstein and Thompson (100). Hence the steady state is specially excluded.

Table 2-2: Values of the time constant,  $\tau$ , in seconds, as a function of the binding,  $E_B$ , and the hydrogen diffusivity,  $D_H$ .(105)

| $-E_B$ (eV)<br>$D_H$ ( $\text{cm}^2/\text{s}$ ) | 0.3                | 0.4                | 0.5                             | 0.8                  |
|---|--------------------|--------------------|---------------------------------|----------------------|
| $10^{-5}$                                       | 265                | $8 \times 10^5$    | $2.4 \times 10^9$<br>(76 years) | $6.2 \times 10^{19}$ |
| $10^{-10}$                                      | $2.65 \times 10^6$ | $8 \times 10^9$    | $2.4 \times 10^{13}$            | $6.2 \times 10^{23}$ |
| $10^{-12}$                                      | $2.65 \times 10^8$ | $8 \times 10^{11}$ | $2.4 \times 10^{15}$            | $6.2 \times 10^{25}$ |

Recently, Nair et al (105) have compared both kinetic models and refined the stripping model by using a more rigorous mathematical treatment; their results confirmed that enrichment was indeed feasible. Table 2-2 shows typical supersaturation results obtained by Nair et al, where  $\tau_0$  is the time constant for achieving steady state. When the testing time is much less than  $\tau_0$  (i.e. a large  $\tau_0$ ), the leakage rate of hydrogen is much less than the arrival rate of hydrogen at the trap, hence accumulation of hydrogen occurs and so does supersaturation. On the other hand, if the testing time is much larger than  $\tau_0$  (i.e. a small  $\tau_0$ ), steady state is readily achieved and supersaturation is highly unlikely. It is clear, from Table 2-2, that in a high diffusivity matrix such as iron ( $D_H = 10^{-6} \text{ cm}^2/\text{sec}$ ), supersaturation can be obtained if the binding energy between hydrogen and trap is higher than 0.3 eV which is about the binding energy between hydrogen and a microvoid in iron (Table 2-3). A even larger  $\tau_0$  can be obtained for a binding energy of about 0.8 eV which is about the binding energy between a carbide interface and hydrogen.

Table 2-3: Trapping energy of various possible traps in iron.(24)

| TRAP SITE                          | BINDING ENERGY (kJ/mole) | (eV)         |
|------------------------------------|--------------------------|--------------|
| H-dislocation elastic              | 0 to 20.2                | 0 to 0.21    |
| H-Ti                               | 26.1                     | 0.27         |
| H-void                             | 28.6                     | 0.30         |
| H-dislocation core (screw)         | 20 to 30                 | 0.21 to 0.31 |
| H-dislocation core (mixed)         | 58.6                     | 0.61         |
| H-grain boundary                   | ~58.6                    | 0.61         |
| H-AlN interface                    | 65                       | 0.675        |
| H-free surface                     | 70.7                     | 0.73         |
| H- $\text{Fe}_3\text{C}$ interface | $\geq 84$                | $\geq 0.87$  |
| H-TiC interface                    | 94.6                     | 0.98         |

From the above considerations, it is clear that current theories of kinetic supersaturation have several critical assumptions such as trap geometries, strength of the dislocation-hydrogen interactions etc., and thus require

convincing analytical and experimental justification, if they are to be further applied. Further, whether this enrichment can produce local pressurization or other manifestations of internal damage depends upon the details of the microstructure. For example, if there are microvoids or decohered particles present, hydrogen recombination is possible, and pressurization can possibly occur. Alternatively a high local hydrogen concentration may encourage localized dislocation mobility, causing enhanced plastic instability and thus result in premature failure by a process akin to strain exhaustion(23,24).

In summary, limited experimental observations have suggested the occurrence of a causal relationship between hydrogen transported by mobile dislocations and an increase in the material's hydrogen susceptibility. This is believed to be the case even if concurrent to dislocation transport, significant trapping effects occur, as evidenced from various straining permeation experiments(95, 106-107). While this trapping effect must be taken into account to accurately simulate all possible interactive dislocation effects during plastic deformation(95, 106-107), experimental conditions which minimize the trapping effect are essential to independently understand the transport nature of mobile dislocations. In addition, the possible occurrence of hydrogen supersaturation associated with dislocation transport needs to be more carefully documented and, if possible, related to our current understanding of hydrogen embrittlement processes. These, in brief, are the prime goals that we wish to accomplish in this thesis.

## 2.2. Dislocation Dynamics in BCC Iron Crystals

To further clarify the dislocation transport phenomenon in iron, dislocation behavior during plastic deformation must be clearly identified and described. In addition, since it has been recently recognized that hydrogen may affect dislocation dynamics(97,98), the following review will be organized as follows: The general dislocation dynamics in bcc iron crystals will first be presented, and then hydrogen effects on various aspects of dislocation dynamics, such as dislocation mobility, work hardening behavior and strain localization will then be discussed.

### Slip System

The deformation of body centered cubic crystals, especially iron, has been a favorite subject of many investigators since the early work of Taylor and Elam(108). Studies have focused on operating slip systems(109-111), and on the occurrence of twinning or fracture(112-114). It is now well established that bcc crystals slip in the  $\langle 111 \rangle$  direction on specific planes contained in the  $\langle 111 \rangle$  zone. However, the operative slip plane is apparently not unique, with a number of possibilities proposed(109-114). The consensus is that there are three types of slip planes possible, namely {110}, {112} and {123}, which can be operative, depending not only on the crystal orientation but also test conditions. For example, various investigators(115-117) have shown that the operative slip system can be a strong function of purity, alloy content, deformation temperature and strain rate. Based on the geometrical consideration between tensile axis and various possible slip systems, Schmid(118) developed a critical resolved shear stress criterion, which predicted that under uniaxial tension or compression, any slip system in the crystal with a resultant shear stress exceeding some critical value will be activated. Therefore, the particular operating slip system can be determined totally on a geometric basis by finding the slip system with the maximum resolved shear stress. This well-known Schmid's law has been successfully applied to fcc crystals where only one type of slip plane ({111}), and slip direction  $\langle 110 \rangle$  is possible. However, for bcc crystals, it has been found that predictions based on Schmid's law were not always obeyed in a number of bcc metals, especially at low temperature(116,119). In contrast, Keh(120) found that for iron single crystals oriented such that the maximum resolved shear stress falls on the {112} $\langle 111 \rangle$  slip systems, Schmid's law predictions are always obeyed for both single or double slip orientations, tested at temperatures between 473 K and 77 K, including room temperature. This findings have now also been verified by others(98,121) and in the present study.

Following the Schmid's factor approach for predicting the critical resolved shear stress (CRSS), Kelly and Groves(122) calculated the most probable slip systems for different tensile axes, using the combination of two most commonly observed slip planes, {110} and {112}, and the accepted  $\langle 111 \rangle$  slip direction. Figure 2-1 shows an expansion of their unique triangle construction which allows easy recognition of the predicted operating slip

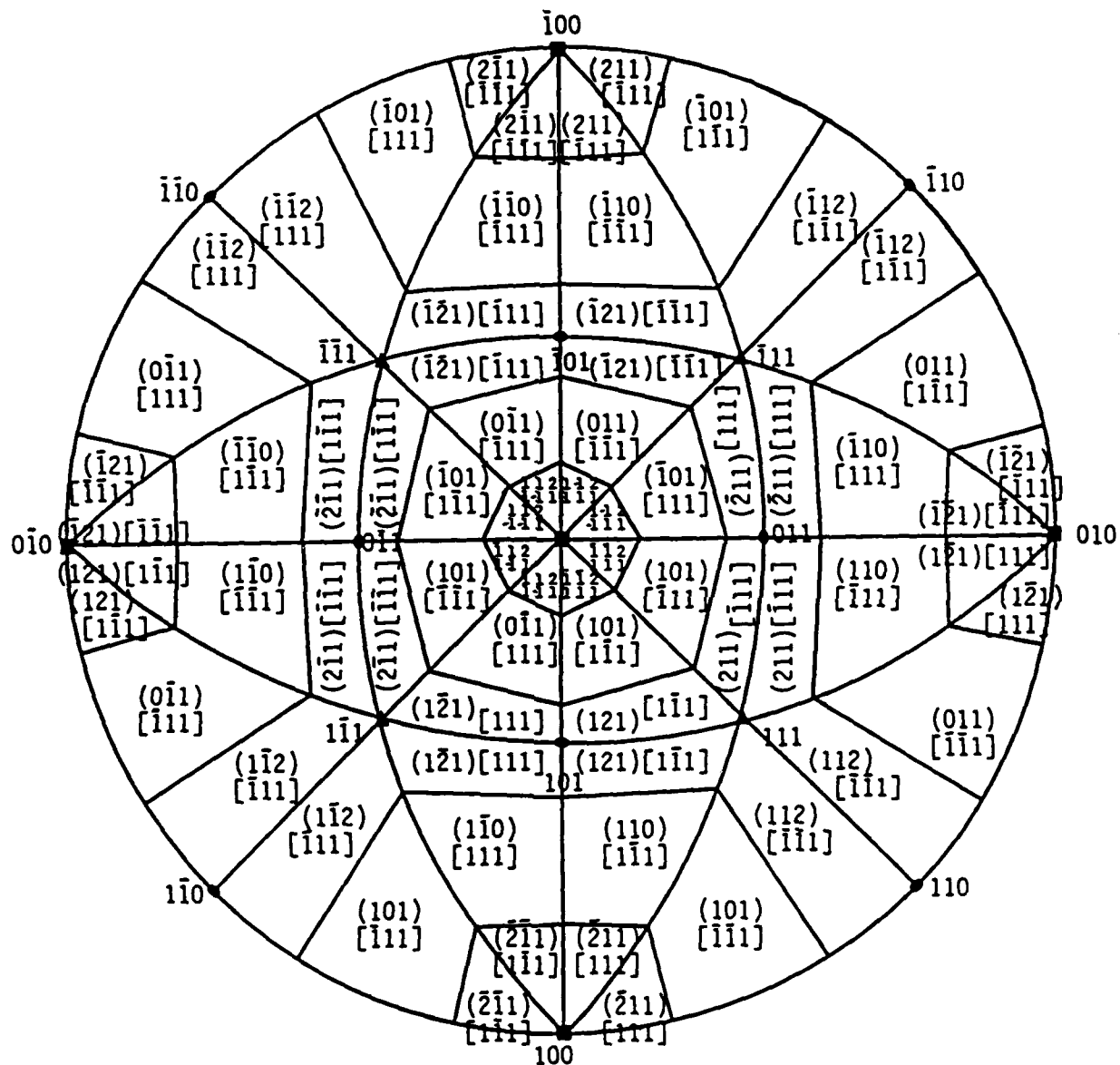


**Figure 2-1:** The maximum resolved shear stress slip systems at different tensile axis orientation, predicted by Schmid's factor, using  $\{112\}$  and  $\{110\}$  as slip planes and  $\langle 111 \rangle$  as slip direction.

system under any particular tensile axis orientation. Unlike the fcc crystals which have only one unique slip system within the unit triangle, there are now three different zones inside a given triangle, with three different slip systems possible. It should also be noted that on both sides of the  $\langle 110 \rangle$ - $\langle 111 \rangle$  boundary, the slip system is identical, leading to an ideal single slip orientation for {112} slip along this boundary, as supported by the results of Keh(120) and others(98,121).

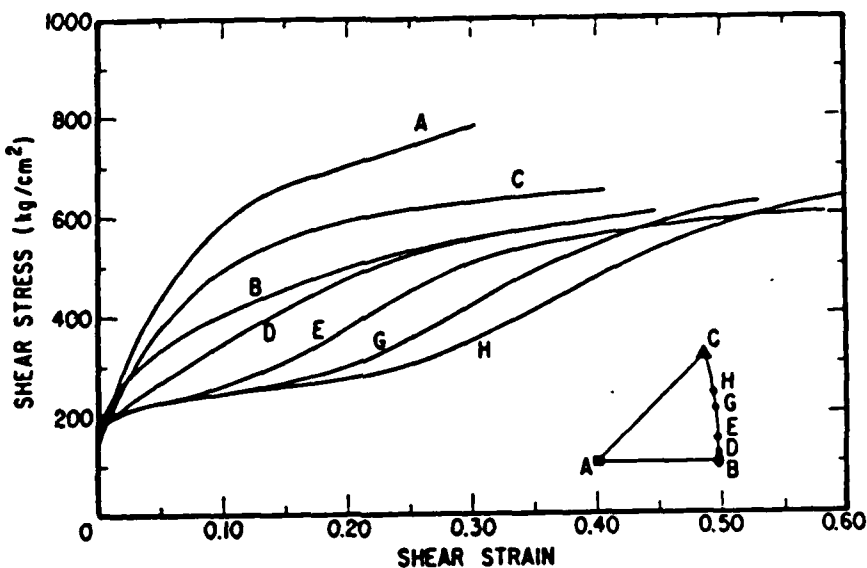


Figure 2-2: Orientation dependence of stress-strain curves of iron single crystals at 298 K.(133)

#### Work Hardening

The room temperature three stage work hardening behavior in bcc metals was first investigated by Mitchell et al(123) in niobium; subsequently, similar observations were made in iron(120), in tantalum(124), and in molybdenum(125). In particular, it has been shown that the work hardening behavior of iron single crystals at room temperature is very orientation dependent(120,126-127). Parabolic stress-strain curves were observed for crystals oriented for multiple slip while for crystals with tensile axes inside the unit triangle or along the  $\langle 110 \rangle$ - $\langle 111 \rangle$  boundary, the stress-strain curves are characterized by a three

stage hardening process, similar to that in fcc crystals. In crystals oriented for such single slip, the work hardening rate and the extent of the easy glide region can vary considerably from orientation to orientation(128-129). For example, as shown in Figure 2-2; crystal B is in a double-slip orientation which does not show an easy glide stage I region; for other orientations, the further the tensile axis is from crystal B (e.g. orientation H), the more pronounced is the three stage hardening behavior. This change of work hardening behavior with crystal orientation, has been suggested by Keh(120) to be due to differences in the Schmid's factor ratio of the major secondary slip system compared to the primary slip system. As the orientation moves away from crystal B, this ratio decreases from 1 to 0.46 for orientation H, and concurrently the stage I extention increases and its slope decreases. The low work hardening rate in stage I is believed due to the small secondary dislocation density that develops, since the work hardening rate in iron crystals undergoing three stage hardening has been shown to be proportional to the ratio of secondary to primary dislocation densities(130).

#### Temperature Effect

The temperature dependence of yield and flow stresses has also been extensively studied(121,128,131). Most observations revealed that bcc metals in general have a large temperature dependence of both the yield and flow stress, and this is frequently attributed to the large Peierls-Nabarro stress inherent in the bcc lattice at low temperature(121,131). The work hardening behavior of iron single crystals also varies a great deal with the deformation temperature; an example of this can be seen in Figure 2-3. The three stage hardening behavior becomes less pronounced as the temperature is lowered below ambient; above 298 K the easy glide region and stage II are both restricted(128). This can be rationalized as follows: At higher temperatures, dynamic recovery sets in at an earlier stage of deformation and three stage hardening becomes less pronounced. At temperatures lower than 298 K, the work hardening behavior was affected by the lattice frictional stress; again, three stage hardening was absent.

#### Impurity Effect

There have also been detailed studies concerning the dislocation

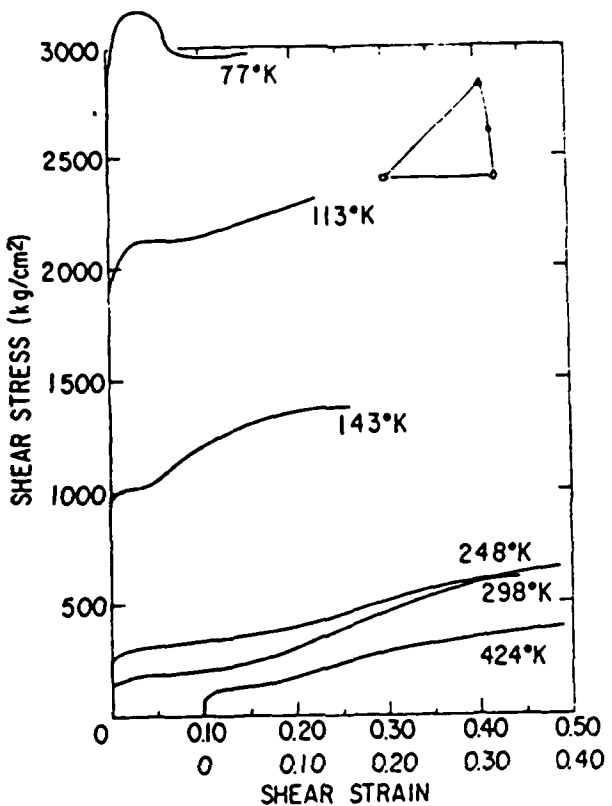


Figure 2-3: Effects of deformation temperature on the stress-strain curves of iron crystals.(128)

configurations developed during plastic deformation in iron with different impurity levels(130-134). The general agreement from these studies is that, for crystals plastically deformed at room temperature with tensile axes in the three stage hardening orientation, the purer crystal exhibits clusters of primary edge dipoles of varying length and width lying in the slip plane in stage I, with the total secondary dislocation density only a small fraction (10 to 20 %) of the primary dislocation density. The lack of primary screw dislocations on the slip plane is usually attributed to screw dislocation segments being annihilated by cross slip and as a result only edge dislocation segments which have become immobilized remain on the slip plane(135). In contrast, in the less pure crystals, long primary screw dislocations are a common feature observed in stage I deformation(130,136). The precipitates or solute clusters present in these less pure crystals apparently hinder the annihilation of screw dislocations(134,137-138), presumably by inhibiting cross slip. At lower temperature, the long jogged screw dislocations formed during deformation in

both pure and less pure crystals are a general feature of single crystal iron(137) and other bcc metals(123-125), and are attributable to the mobility difference between edges and screws at temperatures where the flow stress increases rapidly.

### 2.3. Hydrogen Effect on Dislocation Dynamics in BCC Iron

Recently, since the interaction between hydrogen and dislocations was recognized as possibly having an important role in hydrogen-assisted failure processes, considerable interest developed in ascertaining whether or not there is an intrinsic effect (e.g. a hydrogen-induced reduction of the Peierls force) and/or an extrinsic effect (e.g. hydrogen-induced inhibition or enhancement of dislocation pinning) on dislocation behavior. In particular, hydrogen has been reported to cause both hardening and softening in iron(139-141), depending on the impurity level, testing temperature, single crystal orientations etc.. Kimura et al(98,139,141-144) have made a thorough study on this subject and concluded that in a high purity iron, the presence of hydrogen can evoke a remarkable softening effect between 200 K and 296 K, whereas at temperature below 200 K, a hardening effect becomes dominant. Further, for single crystals oriented in the single slip orientation, hydrogen enhances the extent of easy glide strain near room temperature. At temperatures lower than room temperature, hydrogen can also change the work hardening characteristic of iron crystals; for example, at 200 K, the stress strain curve of hydrogen charged iron single crystals show three stage hardening, while that of hydrogen free iron single crystals are parabolic(98), for identical orientations. This phenomenon has been attributed to an effect of hydrogen on dislocation mobility, relating it to the well known fact that at room temperature the velocity of edge dislocations is much faster than that of screw dislocations in iron(98,145-146). Since the onset of stage II work hardening can be triggered by the relative mobilities between primary screw dislocations and secondary edge dislocations, when the latter are activated, the stage II hardening can be initiated, as the dislocation interaction rate increases.. Kimura et al(98,147-148) have speculated that hydrogen at the dislocation core reduces the Peierls stress of a screw dislocation while hindering the mobility of edge dislocations, hence effectively enlarging the difference in mobility between primary screw dislocation and secondary edge dislocation, and inhibiting the stage II hardening till larger strains.

By using single crystals carefully aligned for double slip, Kimura et al(98) have also found that under hydrogen charging condition, when the crystal surface is aligned such that screw dislocations can easily escape from the crystal (i.e. the primary Burgers vector is parallel to the crystal surface), the dislocation multiplication rate is slower and the easy glide region enlarged. This observation supports the common observation that at room temperature the plastic deformation of impure iron is governed mostly by screw dislocation movement. This aspect will be discussed in detail when the dependence of hydrogen transport rate on dislocation type is presented.

A direct observation of hydrogen enhancement of screw mobility in iron has also been reported by Tabata et al(62,97), using an *in situ* tensile stage in the HVEM, although, as with other observations(98), the cause is unclear.

#### Strain Localization

Another possible effect of hydrogen on plastic deformation behavior is the enhancement of strain localization (or plastic instability). It is generally recognized that for ductile or quasi-cleavage fracture, localization of the plastic flow invariably precedes the final fracture processes. The localization plastic flow can be in the form of necking, shear band (Luders band) developments or slip band formation in the grain(58). Conditions for initiating these forms of local unstable plastic flow, in particular under uniaxial tension, has been formulated by Hart(149), based on the dependencies of flow stress on work hardening rate and strain rate sensitivity. He has formulated a general criterion for plastic instability, later shown(150-151) to apply to both geometrical and deformation defects in a tensile specimen.

The characteristic directions for localized strain are normally along the pure shear (i.e. no normal strain) directions. Based on an isotropic ideal plastic assumption, this is found in uniaxial tension to be about 55° away from tensile axis. This pure shear direction will match with the maximum shear direction under plane strain stress state conditions(152-158). It should be noted, however, that a real material can exhibit localized plastic flow along these calculated directions only when it obeys the dynamic ideal plastic stress state, and in addition it must also have a low work hardening rate and a low strain rate sensitivity of stress(149). Various studies have concentrated on the

formation of this strain localization phenomenon; different theories such as shear banding(159-160), bifurcation of plastic flow (corresponding to the localized plastic deformation into a planar band(154-156)) etc., have been proposed. However the exact mechanism for the onset of this instability is still uncertain(161-162).

The onset and extent of plastic instability was experimentally found to be enhanced by the presence of hydrogen. This was manifested by concentrated shear along characteristic slip traces, in contrast to uniform flow in an uncharged, otherwise identical, specimen(40-41,58), or to the formation of multiple criss-cross Luders bands, compared to a single band for the uncharged case(61). This has led to various speculations(40-41,58,61,163) of hydrogen's effect on strain response and microstructure.

An explanation based on the enhancement of highly localized dislocation motion by hydrogen was first proposed by Beachem(16), based on careful fractographic examination. Other studies on hydrogen enhanced strain localization have concentrated on macroscopic stress strain behavior and surface roughening effects(164-165), while yet others have relied on direct microstructure observations(62). In addition, *in situ* observations of crack propagation led to the conclusion that the crack initiation sites are the dislocation cell walls (i.e. dense dislocation tangled structure) which form at or near the crack tip by absorbing or emitting dislocations(166-168). While this phenomenon was observed under both vacuum and hydrogen atmospheres, in the later case, localized plasticity became more pronounced. This was believed due to a mutually-enhancement of the interaction between hydrogen and dislocation motion. This is also supported by the linear irreversible thermodynamic argument of Louthan(99) who argued that the symmetry of the Onsager coefficients can be applied to hydrogen transport by mobile dislocations; while the dislocation motion can transport hydrogen, the redistribution of hydrogen in of itself can also enhance dislocation motion. Therefore, the combination of a hydrogen concentration gradient and dislocation motion should promote strain localization. This type of analysis predicts that strain localization should be most apparent in the presence of a steep hydrogen concentration gradient as has been observed by Onyewuenyi and Hirth(58).

## Chapter 3

### Research Objectives and Experimental Approaches

As the study and theory of hydrogen embrittlement has developed, more and more researchers have found that for the usually cited cases where fracture is macroscopically totally brittle, considerable plasticity can still be involved in the fracture process, especially localized to the near surface region(37). This finding has suggested that both hydrogen-induced plasticity and associated interactions between hydrogen and dislocations are extremely important in most hydrogen-assisted fracture processes. Numerous studies have concentrated on this subject and recently many aspects have been investigated in detail; for example, work hardening/softening behavior(98), temperature effects(98) and trapping and transport phenomenon(95,169-170). For the last of these, the location and strength of hydrogen trapping sites have been studied by such diverse techniques as electrochemical permeation and autoradiography techniques. Hydrogen-related transport during plastic deformation is also of great interest, as is the trapping of hydrogen at stationary and mobile dislocations. Most recently, the possibility of mobile dislocation transport of hydrogen has drawn special attention as a way to correlate experimental findings where the measured hydrogen transport rate is much faster than lattice diffusion(47,57). Such transport could also lead to the supersaturation of hydrogen within the lattice at specific sites and there has been considerable theoretical discussion on this topic(81,103,105). A prime motive of this research study is to further improve our understanding of the condition for, and the characteristic nature of, hydrogen transport by dislocations, and in particular to evaluate as quantitatively as possible the transport rate as a function of dislocation character in iron, as well as to identify consequential microstructure changes due to this transport mechanism.

In order to accomplish this multi-purpose project, a carefully devised experimental plan was essential to avoid pitfalls in experimental technique and

interpretation. Drawing on considerable past experience(171), the electrochemical straining permeation technique was selected as the most reliable and flexible means to measure the hydrogen transport rate. To separate effects of dislocation type and to further classify observed differences, selected high purity iron single crystals with various combinations of tensile axis and surface orientation were employed, to ensure that during plastic deformation only one type of dislocations will predominantly intersect the monitored crystal surface. Three different combinations of tensile axis and surface orientation were prepared so that the response of screw, mixed and edge dislocations could be independently studied.

The success of this experimental study enabled us to elucidate the characteristic nature of dislocation transport of hydrogen in iron at, and near, room temperature, as a function of such obviously important variables as strain rate and hydrogen concentration. Further we were also able to relate the consequences of this transport process to the possible substeps leading to hydrogen induced strain localization, cracking and embrittlement in ferrous alloys.

## Chapter 4

# EXPERIMENTAL PROCEDURES

### 4.1. Overview

In order to precisely study if and how hydrogen is transported by dislocations in iron, it is important that the dislocation dynamics in the material are well known. To achieve this goal, high purity iron single crystals of different orientations were chosen to minimize the complexities of impurity and grain boundary effects on subsequent dislocation behavior. Further, a specific combination of crystal orientation, tensile axis and surface orientation can be selected to give rise to different types of dislocations intersecting the specimen surface of interest, thus permitting the relative contribution of different dislocation types on hydrogen transport mechanism to be separately studied.

To complement the above study, polycrystalline pure iron was also evaluated, in particular to characterize the combined effects of hydrogen trapping and transport by mobile and stationary dislocations. The relative importance of these two counter effects was evaluated from measurements of apparent diffusivities with and without straining.

### 4.2. Composition and Heat Treatment of Materials

#### 4.2.1. Single Crystal Material

Iron single crystal plates, 2.5 cm wide, 0.2 cm thick and of various lengths were previously prepared from strain annealed Ferrovac E or Plast iron<sup>1</sup>. Further purification, primarily of carbon, was achieved by decarburization in a wet hydrogen atmosphere for 120 hours at 1033 K, and annealing at 1123

---

<sup>1</sup>These crystals were provided by the Fundamental Research Laboratory of the US Steel Corp.

K under dry hydrogen for one hour. These treatments resulted in an interstitial atom content below 100 wt. ppm, consisting of approximately 18 wt. ppm C, 70 wt. ppm O (almost all insoluble), and 8 wt. ppm N.

The crystals were cut to the desired orientation using either an Isomet<sup>2</sup> diamond saw or a spark cutter with a molybdenum blade; the invariably present thin deformed layer on the surface was subsequently removed by chemical polishing in a 92% H<sub>2</sub>O<sub>2</sub> plus 8% HF solution. This polishing treatment also resulted in a mirror-like surface finish, making it readily amenable for subsequent surface plating with Pd, as described in Section 4.4.1.2.

#### 4.2.2. Polycrystalline Material

The material in this case was also Ferrovac E iron, a purified grade containing initially approximately 50 wt. ppm C, 10 wt. ppm N and 18 wt. ppm O as the major impurities. The pure iron plate, with an initial thickness of about 0.2 cm, was cold rolled to 0.05 cm and then annealed in argon at 1073 K for one hour to obtain an average recrystallized grain size of about 100  $\mu$ m. Specimens with a gauge length of 4 cm and a width of 2.5 cm were then prepared with the surface finish procedure and Pd plating identical to that for the single crystals.

#### 4.3. Single Crystal Orientation Determination

Because single crystals are usually anisotropic, it is necessary to obtain an accurate knowledge of their orientation so that experiments can be conducted along known crystallographic direction and planes. Three main X-ray methods are commonly used in determining crystal orientation: the back-reflection Laue, the transmission Laue, and the diffractometer method(172). The first of these is the most widely used because it requires no special specimen preparation.

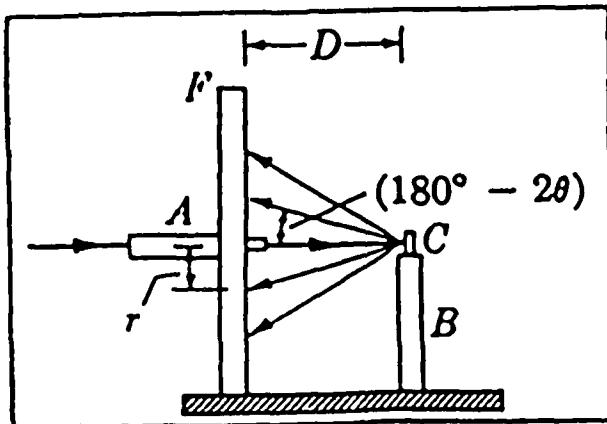
In the back-reflection Laue method a white radiation beam generated from a heavy metal target, usually tungsten, is used and is impinged onto the

---

<sup>2</sup>Trade name of low speed saw made by Buehler LTD.

single crystal at a fixed Bragg angle. The photographic film is placed between the single crystal and the X-ray source; the incident beam passes through the center of the film, and the beams diffracted from particular planes in a backward direction are recorded. Laue spots are often formed by overlapping reflections of different orders; for example, the 100, 200, 300, --- reflections are all superimposed since the corresponding planes are all parallel. In other word, the position of any Laue spot on the film is unaltered by a change in plane spacing.

Since the orientation of the specimen is to be determined from the location of the Laue spots on the film, it is necessary to orient the specimen relative to the film in some known manner. Usually, it is convenient to mount sheet or plate specimens with a known plane parallel to the plane of the film and one edge of the sheet or plate parallel to an edge of the film. The Bragg angle  $\theta$  for any spot is found, as illustrated in Figure 4-1, from the relation



**A:** X-ray Source    **B:** Specimen Stage    **C:** Specimen  
**F:** Film

Figure 4-1: The angular relationship of standard Laue X-ray diffraction method.(172)

$$\tan(180-2\theta) = r/D \quad (4.1)$$

where  $r$  = distance of spot from center of film and  $D$  = specimen to film distance (usually 3 cm).

The determination of the crystal orientation from the position of the back-reflection Laue spots on the film is accomplished by determining the orientation of the normal to the planes causing each spot, because the plane normal always bisects the angle between the incident and diffracted beam. A graphical method of determining the plane normal in space using its angular coordinates has been devised by Greninger(173), in which the two dimensional angular relationships obtained from the Laue spots are mapped onto a stereographic projection, and the crystal orientation can then be readily determined. For the case of a low index zone axis (i.e. crystal plane), the symmetry of the Laue pattern can also be used as a short cut method to fix the crystal orientation.

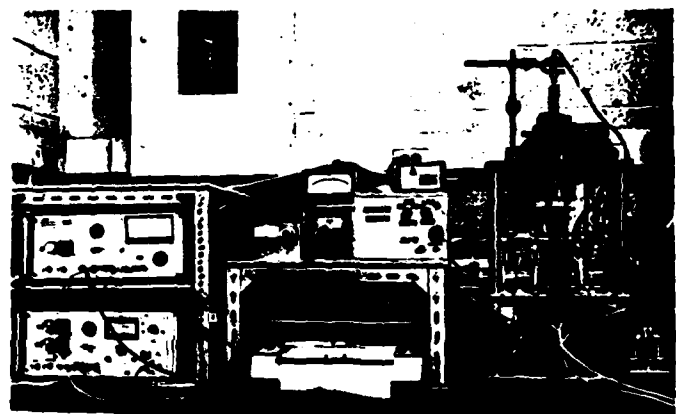
#### 4.4. Straining Permeation Test

The straining permeation test was the major test approach in this thesis to study hydrogen transport mechanisms. Figure 4-2 shows the overall set-up: It is composed of three major sub sections; electrochemical cells to provide a sensitive, controllable means of generation and detection of hydrogen, a straining component involving a tensile test device (e.g. Instron) and a recording component, either an analog recording device such as a strip chart recorder or a computer data acquisition system. To illustrate in detail how these three sub-sections are incorporated for the straining permeation test, they will each be described in detail in the following sections.

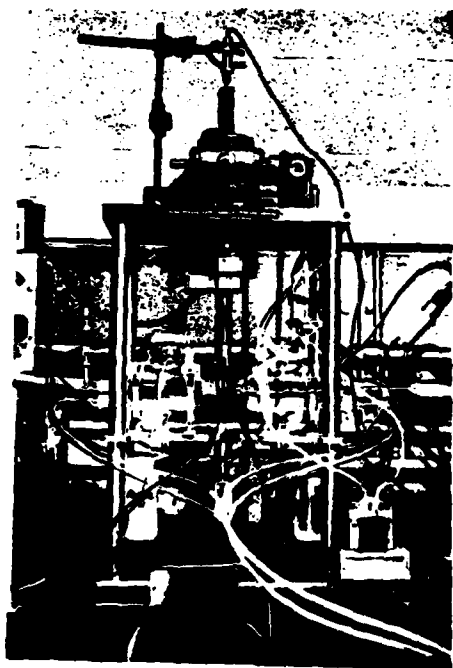
##### 4.4.1. Permeation Apparatus

###### 4.4.1.1. Overview

The hydrogen permeation set-up is composed of two separate electrochemical cells joined together by a thin tensile specimen sheet. The specimen acts as the working electrode for both cells; on the one side, hydrogen is generated electrochemically, while on the other a sufficient oxidation potential (versus hydrogen) is applied to oxidize all atomic hydrogen coming out of the specimen surface, in order to maintain a null concentration



(A)



(B)

**A : Overall Set-up      B : Straining Device**

Figure 4-2: The overall straining permeation test set-up for this study.

of hydrogen on the surface. This fixed boundary condition imposes a known driving force for hydrogen to diffuse down the concentration gradient within the specimen, manifested by a hydrogen flux on the specimen surface where the oxidation current is then equivalent to the hydrogen flux, so long as hydrogen is the only oxidizable species.

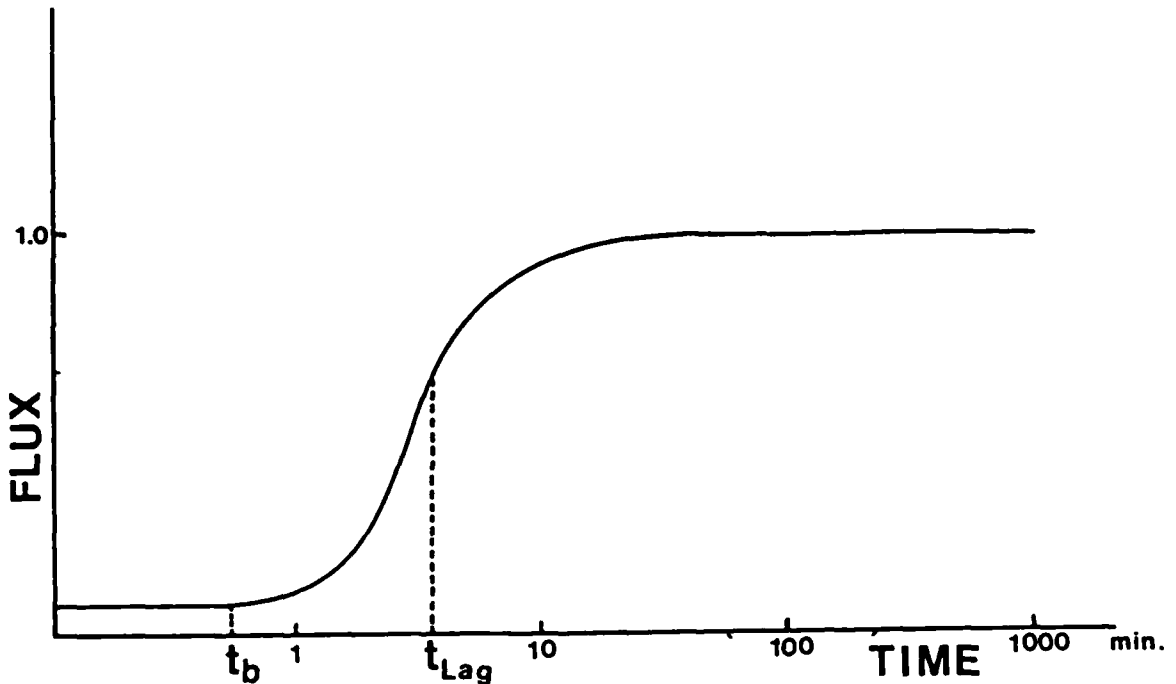


**Figure 4-3:** The flux versus time curve for permeation test; the breakthrough time  $t_b$  and lag time  $t_{Lag}$  are defined in the figure.

The associated hydrogen diffusivity and solubility related to this one-dimensional diffusion process for the known experimental initial and boundary conditions, can be solved using Fick's first and second laws. It should be noted, however, that these solutions assume a pure lattice diffusion process, while in our case, the presence of numerous crystal imperfections interfere with the lattice diffusion process. Consequently, a modified Fick's law has been developed(71,76-77,174) to deal with these complicated effects arising from hydrogen being trapped for varying times at a spectrum of defects. While considerable efforts have been devoted to characterize and predict these

trapping effects(66-77), a unified theory is not yet available. Nevertheless, the apparent hydrogen diffusivity can be calculated regardless of the detailed diffusion processes. Two analytical techniques are most often used to yield this apparent diffusivity, through the analysis of the flux versus time curve, as illustrated in Figure 4-3, the time-lag and breakthrough time methods. The time-lag method uses the fact that the integrated quantity  $Q_t$  of diffusing species to pass through a membrane in time  $t$  is given by(175):

$$Q_t = DC_o/L \times [ t - L^2/6D ] \quad (4.2)$$

where  $C_o$  is the fixed input concentration,  $D$  is the apparent diffusivity and  $L$  is the specimen thickness. The intercept on the time axis of the resultant  $Q_t$  versus  $t$  functionality plot is defined as:

$$t_{\text{Lag}} = L^2/6D \quad (4.3)$$

Additionally, the breakthrough time may be used to calculate the apparent diffusivity. This time is defined as the time at which the first measurable hydrogen is detected from the output side of the membrane, given by

$$t_b = L^2/15.3D \quad (4.4)$$

It should be noted again that these analytical expressions shown above are derived based on the ideal one-dimensional lattice diffusion process (i.e. unmodified Fick's laws), and should yield identical solutions only for a perfect lattice and the absence of surface control. However, as discussed above, the different trap populations invariably present make this unlikely, and lead to these time delays reflecting different rate paths. Therefore, it is most important to choose a consistent method for data comparison. For example, the time-lag method usually reflects more completely the integrated effects of trapping since it samples a considerable time portion of the entire diffusion process, prior to attaining steady state. In contrast, the breakthrough time represents only the very early stage of the diffusion process making it very sensitive to the different diffusion mechanism operating. For example, if there are fast hydrogen transport mechanisms (e.g. dislocation transport) operating, the breakthrough time will be dominated by this measure and will reflect little or no information on lattice diffusion rates. Comparison of the two can of course be of considerable value in differentiating between fast and slower diffusion events.

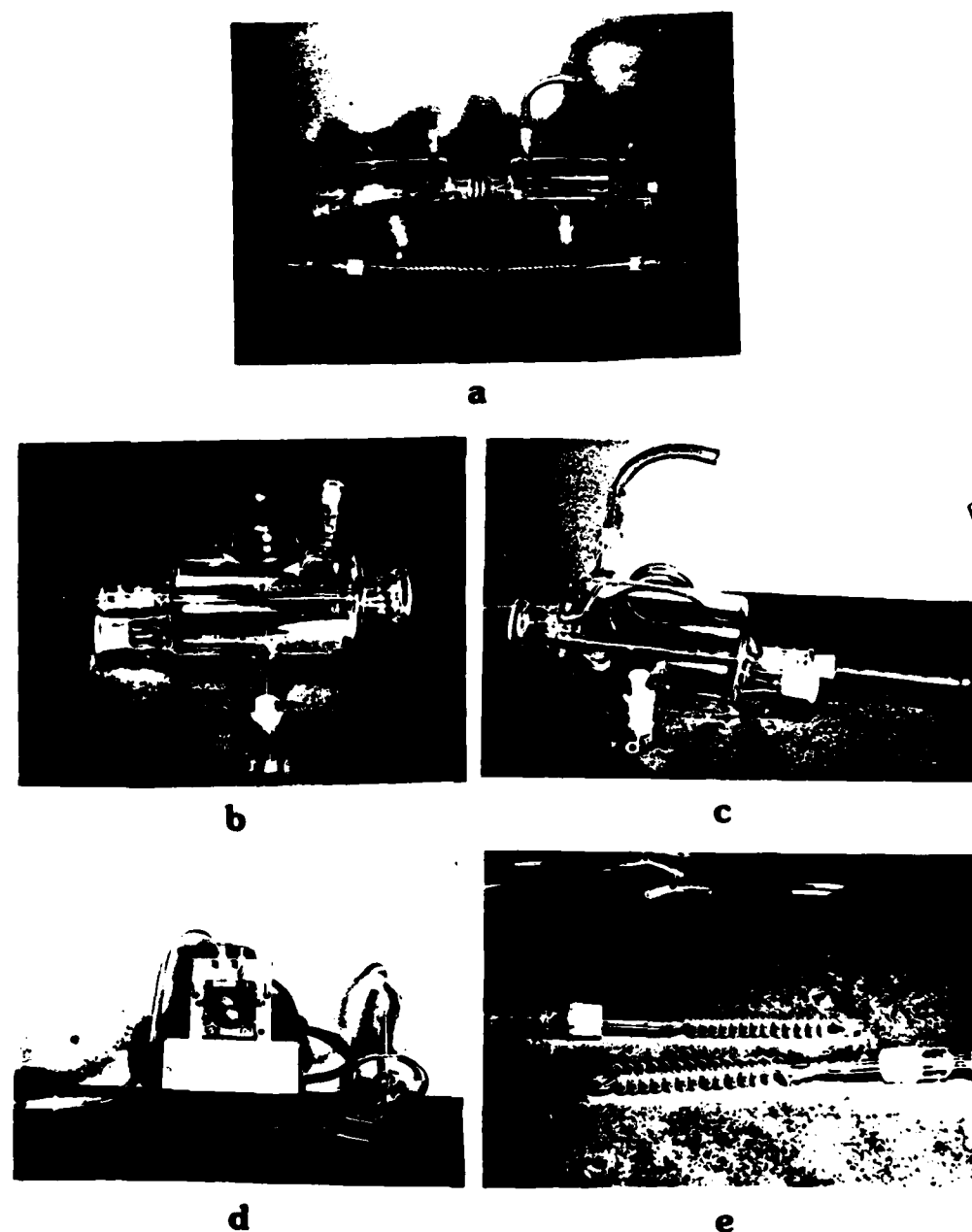
#### 4.4.1.2. Electrochemical Cells

This type of permeation apparatus used was originally developed by Devanathan and Stachurski in 1962 for measuring hydrogen diffusivity in Pd(176). It has recently been modified by Kurkela and Latanision(86,88) and in this study to allow the imposition of concurrent elastic and plastic deformation, so that the contribution to the hydrogen flux by moving dislocations can be evaluated.

Figure 4-4 shows the components of the electrochemical cells designed and used in this study. Two identical cells were made for both the anodic and cathodic sides; the cylindrical portion of the cell is capable of holding a large amount of solution (about 500 ml). All accessories were installed and sealed to prevent any solution degradation caused by long time exposure to the air during the test. A Luggin probe, eliminating the IR drop through solution, provides a close control of the surface potential in conjunction with a calomel electrode and potentiostat. A circulating pump is also employed, via a small probe in close proximity to the specimen surface; the pump circulates the solution from the bulk to the near specimen surface region, reducing any mass transport bottle-necks during the electrochemical reaction. Finally, a thin wall sealed glass heat exchanger was also included for stabilizing the solution temperature by circulating a constant temperature fluid without contamination of the reaction solution. A thermometer was also inserted into the cathodic side of the cell near the specimen surface region for accurate temperature reading, as indicated in Figure 4-4.

High purity (Fisher certified grade) 0.1N NaOH solution was used for the anodic and cathodic electrolytes, and platinum wires were used for necessary counter electrodes. This pair of electrochemical cells were installed on a rack attached to the straining device, as shown in Figure 4-2, which could be independently aligned to minimize possible distortion of the thin sheet specimen due to misalignment or movement of the cells during straining.

In order to apply concurrent straining during the permeation test, the single crystal was chemically shaped to form a gauge section with a reduced thickness of about 0.4 mm, a gauge length of 14 mm and a width of 8 mm,



(a): ELECTROCHEMICAL CELLS (b): ANODIC CELL (c): CATHODIC CELL

(d): CIRCULATION PUMP (e): HEAT EXCHANGERS

Figure 4-4: The electrochemical cells used for the straining permeation test in this study.

by selectively covering the surface with MICCROSTOP<sup>3</sup> and polishing in 92% H<sub>2</sub>O<sub>2</sub> plus 8% HF solution. This single crystal was then attached to a pair of special tensile specimen holders (1040 steel) as shown in Figure 4-5. A high strength solder containing a small amount of silver was carefully applied, using a pre-aligned fixture and a high power (230 watt) soldering gun, to the connected areas to provide necessary strength. Finally the input and output specimen surfaces were electroplated with a 100  $\mu\text{m}$  thick palladium layer using a commercially available palladium plating solution, Palladax VI<sup>4</sup>, at a temperature of 308 K and a current density of 107.6 A/m<sup>2</sup>. This procedure produced a thin and pore free adherent Pd layer on the single crystal surface, a condition shown to provide predictable and controllable electrochemical conditions(171).

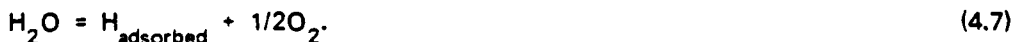
Since the specimen surface (Pd) and counter electrode (Pt) are noble metals, the electrochemical reactions involved are associated only with water electrolysis in a basic solution. On the hydrogen charging side (cathodic cell), the reaction on the specimen surface is:



while the counter part of this reaction on Pt electrode is



therefore, the total reaction is:



This reaction was driven by a galvanostatic set-up using a Princeton Potentiostat-Galvanostat model 371, capable of providing a constant current through the cell and of maintaining the exact level of current flow for the entire test period (stability is better than 1  $\mu\text{A}/\text{day}$ ), a requirement essential to ensuring the boundary conditions for the test.

<sup>3</sup> an insulation lacquer made by Michigan Chrome and Chemical Co.

<sup>4</sup> Trade name of a palladium electro-plating solution made by SEL-REX Division of Oxymetal Industries Corporation.

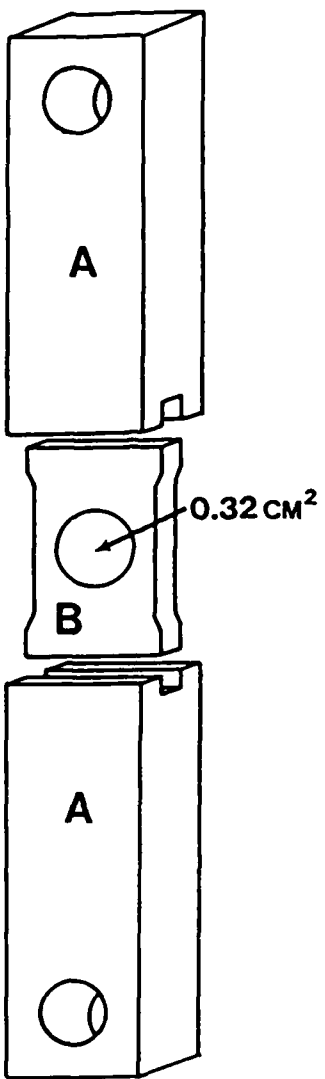


**Figure 4-5:** The single crystal specimen configuration used in the straining permeation test. A: tensile specimen holder, B: single crystal. The exposed area on the single crystal during test,  $0.32 \text{ cm}^2$ , is indicated in the figure. The hydrogen flux reported in this thesis is a direct measurement from this constant area for the single crystal tests.

The anodic cell reaction is the reverse of the cathodic cell reaction; viz:  
on the specimen:



and on the Pt electrode:



This reaction was controlled by a potentiostatic set-up using a Princeton Potentiostat model 173 together with a model 376 current converter. This combination provided the accuracy (better than  $0.002 \mu A$ ) and stability (better than  $10 \mu V/\text{day}$  and  $1 \mu V/K$ ) necessary for detecting the small oxidation currents during the permeation test, which were a direct measure of the hydrogen flux.

These reactions are believed to be the only major ones operating, although others are possible depending on the impurity level of the solution. This is especially true on the cathodic side of the specimen, since for a cathodic overpotential of more than 1.0 volt versus SCE (saturated calomel electrode) applied to the specimen surface, any impurity more noble to water will be reduced and could be coated onto the surface. The most troublesome species in this regard in the solution is the oxygen generated on the counter electrode, which could possibly migrate to the specimen surface and be reduced, thereby altering the surface hydrogen concentration. This in turn would affect the subsequent calculation of the hydrogen permeation parameters. To eliminate this problem, high purity nitrogen gas was purged into the solution before and during the test. This standard deaeration procedure effectively prevented oxygen from reaching the specimen surface.

#### 4.4.2. Tensile Straining

Most of the polystalline iron specimens and initial experiments on single crystals were carried out on an Universal Instron Testing Device (model 1125), capable of performing a variety of tests including tension, torsion and compression. This machine has several shortcomings; first, it proved difficult to physically incorporate into it the necessary electrochemical cells; and

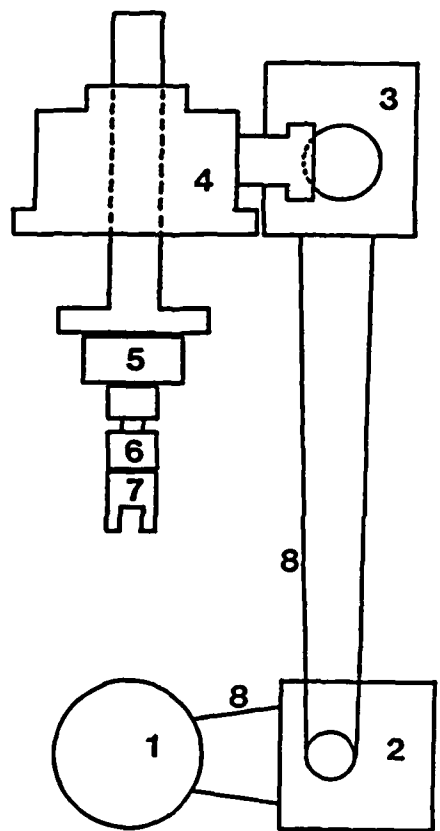
second, the load capacity is 10,000 kg, far higher than is needed for the straining permeation test, even with the available electronic load reduction; and finally, and most importantly, the slowest crosshead speed is 0.05 mm/min., which for a specimen with 1.5 cm gauge length, means that the minimum initial strain rate is only about  $5 \times 10^{-5} \text{ sec}^{-1}$ . While a built-in electronic device can produce a one order of magnitude slower cross head speed (or a strain rate of about  $5 \times 10^{-6} \text{ sec}^{-1}$ ), the resultant crosshead motion is unfortunately non-uniform and jerky. While this system was employed for polycrystalline iron where the higher loads and higher strain rates employed were more compatible with the machine characteristics, the Instron was inappropriate for the more delicate single crystals, particularly since we required a wider range of strain rates.

Due to the discussed difficulties of using the Instron for straining permeation tests especially at very slow strain rates, a slow strain rate testing device was designed and constructed to provide much more accurate measurements of experimental data. In brief, this device used reducing gear boxes to slow down a D.C. motor, whose speed could also be varied by a potentiometer; the components are illustrated in Figure 4-6. A variable speed motor is connected to a multi-ratio speed reducer capable of reducing in stepwise fashion the motor speed from 1:1 to 1:1000; a fixed ratio speed reducer (1:900) is then connected to this multi-ratio speed reducer, and a machine screw Jactuator<sup>5</sup> is driven by this fixed ratio speed reducer to provide the final crosshead movement. The Jactuator itself is equipped with anti-back lash nuts to prevent any free vertical movement, and further is keyed to prevent any rotation and possible associated bending or fluctuating stresses. These requirements are critical to ensure smooth slow movement of the Jactuator during the straining permeation test.

A load cell with maximum load capacity of 1136 kg (2500 lb) is connected to the inverted Jactuator plate and specimen loading was carried out using the specially designed grips shown in Figure 4-7, which combined electrical insulation, with pin loading to minimize bending during the tensile straining. The continuous chain-driven mechanism also ensured the smooth movement of the crosshead, even at very slow strain rates. The entire load

---

<sup>5</sup>Trade name of actuators made by Duff-Norton Company.



- 1 : D.C. MOTOR
- 2 : MULTI-RATIO REDUCER
- 3 : FIXED-RATIO REDUCER
- 4 : JACTUATOR
- 5 : LOAD CELL
- 6 : UNIVERSAL JOINT
- 7 : GRIP

Figure 4-6: The block diagram for slow strain rate tensile testing device designed and constructed in this study.

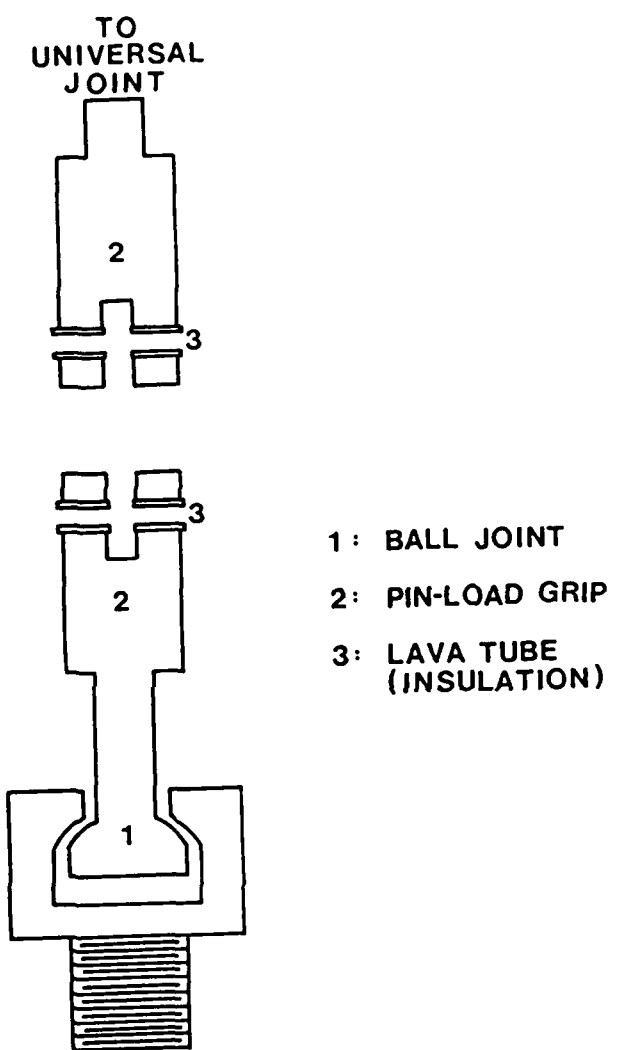


**Figure 4-7:** The special grip system designed and used in this study. Note that the electric insulation of specimen from the entire machine is provided by the lava tube in the pin-load holes.

train was supported by four 2.54 cm diameter tool steel rods mounted between two 2.54 cm thick high strength steel (4340) plates (see Figure 4-2). This high stiffness frame is capable of sustaining much higher load than encountered in the tensile straining of the single crystals.

Additionally, to accurately detect the crosshead speed, a LVDT (Linear Voltage Displacement Transducer) was mounted in parallel with the loading line, for measurement of both crosshead speed and strain rate. With this set-up, an initial strain rate range of  $1 \times 10^{-8} \text{ sec}^{-1}$  to  $1 \times 10^{-4} \text{ sec}^{-1}$  was achievable, covering the desirable strain rates needed for the straining permeation test.

#### 4.4.3. Recording

Most data were recorded by an Omniscribe strip chart recorder whose accuracy is limited by the mechanical time constant of the recording pen. If the signal change rate (i.e. hydrogen flux) is faster than the pen motion, the recorded data will be truncated at both ends leading to inherent errors. Examples to test this possibility are shown in Figure 4-8, where a signal function generator was used to generate saw-tooth signals of various frequencies; the recorded signal on the strip chart recorder can be compared to the true signal, and it is apparent that if the frequency is higher than 0.1 Hz, the recorded data are inaccurate.

In order to better monitor the hydrogen flux, a fast computer data acquisition system was used in several tests in conjunction with the strip chart recorder. A comparison of the recorded data for these two recording systems is shown in Figure 4-9. It is clear that the computer data acquisition system detects much more detailed background noise than does the chart recorder. However, the recorded real data seems to be identical, indicating that the strip chart recorder provides an adequate response time for recording the hydrogen flux during straining permeation test, for our experimental conditions. In fact, it may be better in the sense that the background noise is being filtered during the recording period.

To improve further the resolution of the recorder, a zero-suppression device was used to suppress the zero point on the chart, so that only a small

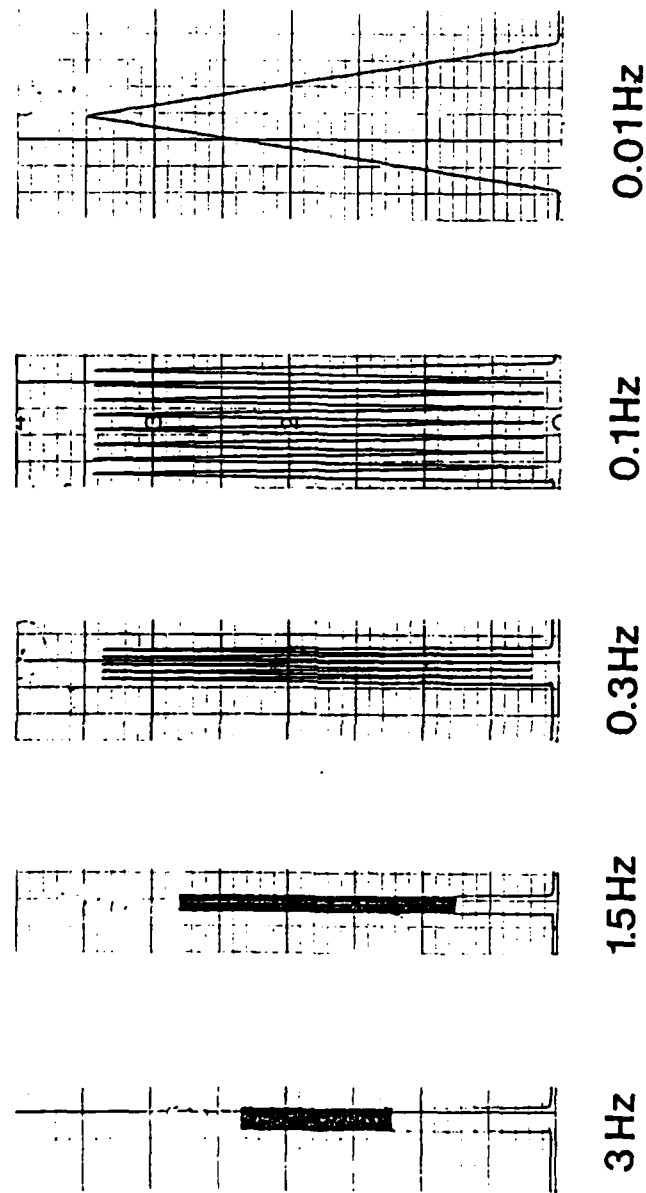
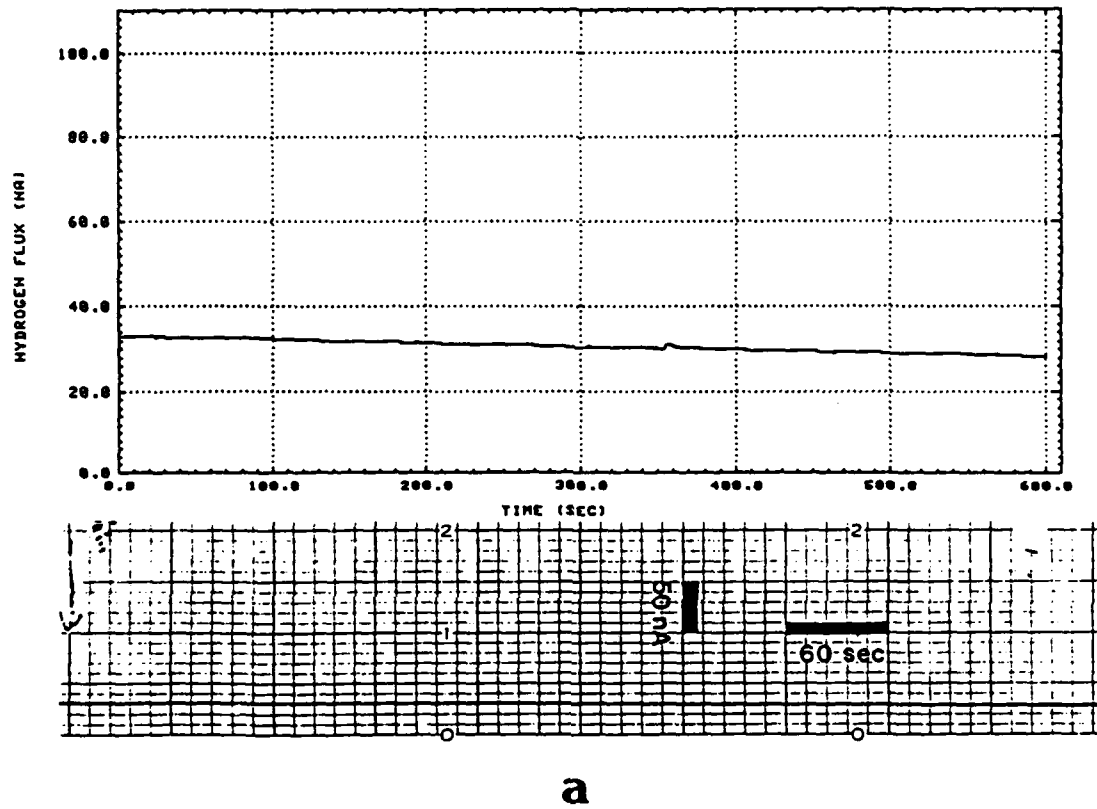


**Figure 4-8:** The response of strip chart recorder (Omniscribe model #B5217-5) for various input frequencies of identical saw-tooth signals. The true signal is shown in the 0.01 Hz response.



a

Figure 4-9: Comparison of the identical hydrogen flux recorded by computer and strip chart recorder for different periods of hydrogen flux during the straining permeation test. (a) background, (b) hydrogen flux in the absence of straining, (c) hydrogen flux during straining.

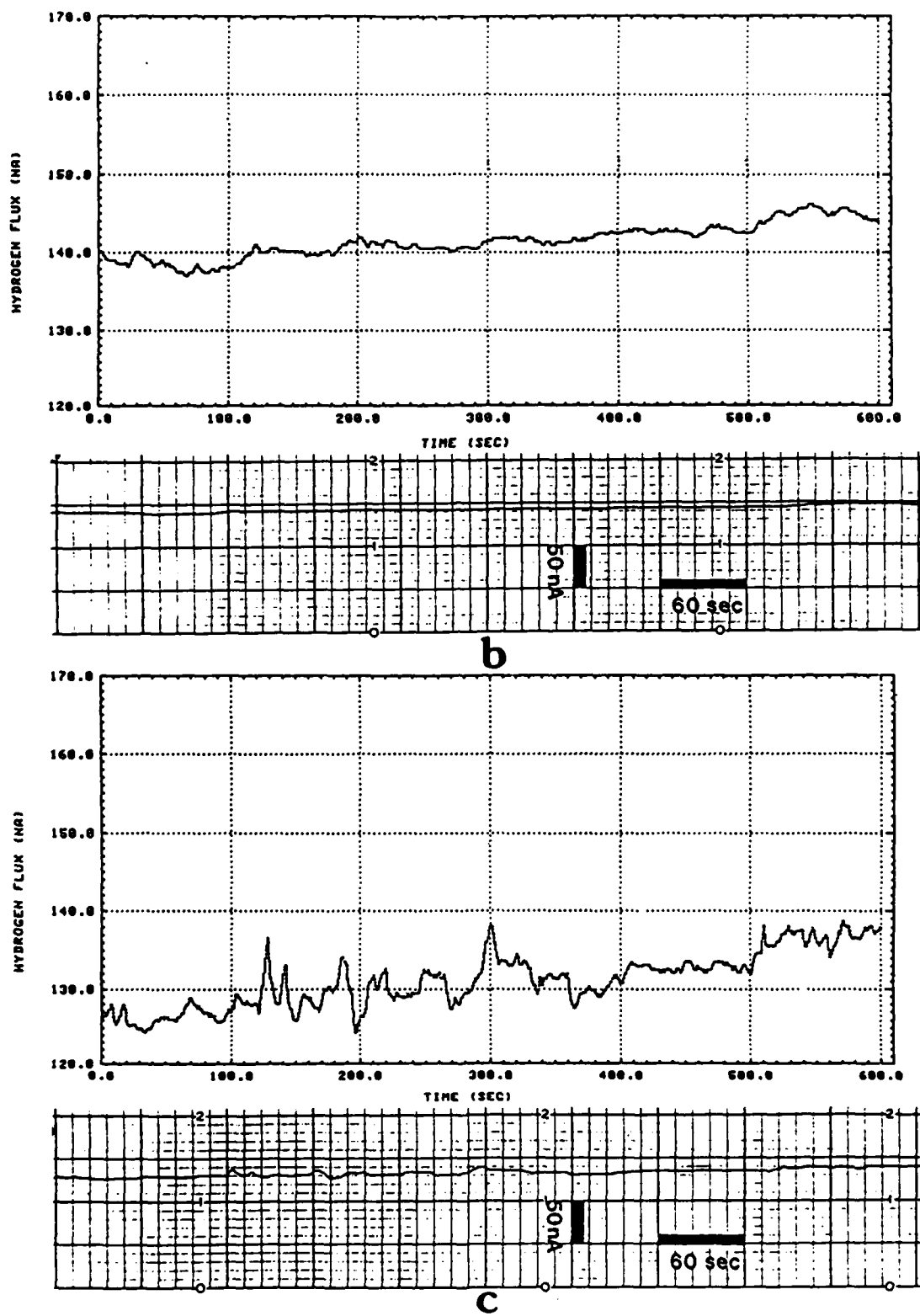


Figure 4-9: Comparison of the identical hydrogen flux recorded by computer and strip chart recorder for different periods of hydrogen flux during the straining permeation test. (a) background, (b) hydrogen flux in the absence of straining, (c) hydrogen flux during straining.

portion of the total flux is recorded, therefore effectively enlarging the scale on the chart. In the single crystal permeation tests, the full scale of the chart is always kept at  $0.5 \mu\text{A}$ , and the amount of hydrogen flux being suppressed is adjusted and recorded in each test to keep the remaining hydrogen flux within  $0.5 \mu\text{A}$ . The resulting resolution of the output flux, using this technique is better than  $0.005 \mu\text{A}$ , which is readily achievable by the electronic devices employed, while also being in a range suitable for detecting any small fluctuation in the hydrogen flux, associated, for example, with dislocation egress. However, this technique will also amplify any noise present, especially when the recorded flux is only a small portion of the total flux (e.g. in the case of higher steady state hydrogen flux with high charging current density). The control and understanding of the origin of the background noise (fluctuation) is very important, because it fixes the absolute resolution of the analysis technique adopted to separate the dislocation transport part of flux from the total hydrogen flux, and the approach used will be described in detail in chapter 5. By way of introduction, the nature of background fluctuations, and these are shown in Figure 4-10, have been carefully classified for different total hydrogen fluxes. It was found that the fluctuation are always of magnitude less than  $0.01 \mu\text{A}$ , which corresponds to a variation in hydrogen flux of about  $1 \times 10^{-13}$  mole H/sec (or  $6 \times 10^{10}$  atom H/sec) from a simple calculation, using Faraday's law. This value will then be the resolution we can have for the quantitative analysis on hydrogen transport rate.

#### 4.5. Straining Permeation Test Procedures

There are operationally many different ways to carry out the straining permeation tests, besides varying strain rate, temperatures etc.. For example, one can begin the straining part before or after the permeation part. Furthermore, since the permeation component also consists of several different regions of flux phenomena, such as breakthrough period, rising and decay transient, and steady state, it is necessary to carefully choose the proper combination and sequencing of strain and permeation in order to obtain easily interpretable results.

In this thesis work, we have selected two main types of permeation tests, in which the crystal orientation, strain rate and hydrogen concentration have also been systematically controlled. The purpose, rationale and the

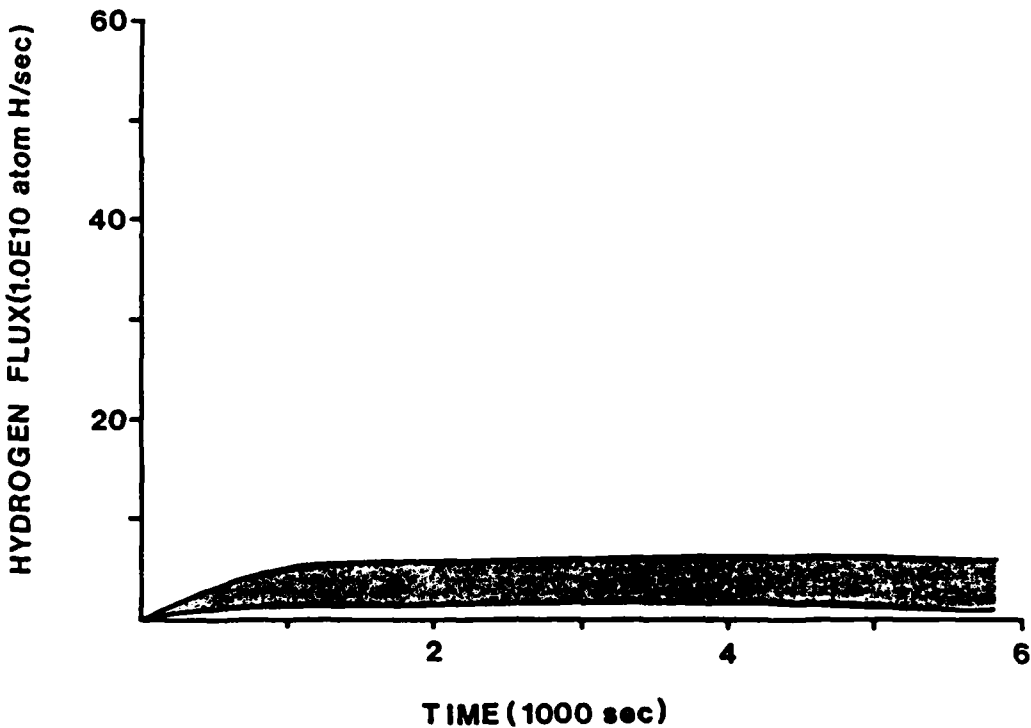


**Figure 4-10:** The background fluctuation range for the single crystal straining permeation test. This also represents the resolution for quantitative analysis of hydrogen flux by dislocation transport. Note:  $1.0\text{E}10 \text{ atom H/sec} = 1.0 \times 10^{10} \text{ atom H/sec}$ .

advantages of choosing these combinations will now be discussed, as well as the necessary precautions associated with each test type.

#### 4.5.1. Straining after Obtaining A Steady State Permeation Flux

In order to explicitly study the mechanism of dislocation transport of hydrogen, other transport mechanisms should either be excluded or kept constant throughout the entire test. While it is impossible to prevent lattice diffusion, at the least, its contribution should be maintained at a constant value. The complication of a non-steady state lattice diffusion was avoided by starting the straining after obtaining the steady state lattice diffusion.

The detailed procedure is as follows: Initially, cathodic charging with hydrogen is carried out with no strain imposed on the specimen, until a steady

state permeation flux is obtained. At steady state, all deep traps are irreversibly filled with hydrogen at the temperature of interest, while weaker traps have an instantaneous population of hydrogen dictated by the reversible equilibrium established between these traps and the lattice(45). Following the attaining of steady state, straining of the specimen was initiated with the cathodic charging current maintained and the hydrogen flux was then continuously monitored throughout the entire test. This procedure was repeated several times often employing a changing strain rate and/or charging current density (i.e. hydrogen concentration) on the same specimen. Between each test, a sufficient time interval was allowed to re-obtain a new steady state flux. In some cases, because of uncertainties due to a somewhat unstable background, especially when the scale was enlarged to obtain a better flux resolution, (section 4.4.3), a fixed time period of about 12 hours was used instead and the very small ( $\sim 1 \times 10^{-4} \mu\text{A}/\text{min.}$ ) increasing or decreasing flux rate was taken as a constant and subtracted during the data analysis.

#### 4.5.2. Straining Prior to Starting the Permeation Test

This technique was used to obtain the apparent diffusivity of hydrogen during plastic deformation, accounting not only for the hydrogen transport rate but also for the concurrent hydrogen trapping rate by newly generated dislocations during plastic deformation.

The detailed test procedure is illustrated in Figure 4-11. Since the apparent diffusivities with and without straining were needed to assess the effectiveness of dislocation transport of hydrogen, two consecutive tests with and without straining were performed, within a narrow total strain range to avoid any complications due to microstructural changes during straining. The straining permeation apparatus was stabilized so that a background current of less than  $0.1 \mu\text{A}/\text{cm}^2$  was obtained. Straining was then imposed on the specimen until plastic yielding ensued, and then the cathodic charging current was imposed while the straining was maintained. The breakthrough time of hydrogen flux was recorded and the first test terminated. Following at least a 12 hour degassing period to ensure that the same initial test condition (essentially very few hydrogen remained in lattice) is obtained, a conventional static permeation test was then conducted. The breakthrough time for the latter test was also recorded and the ratio of apparent diffusivities with and

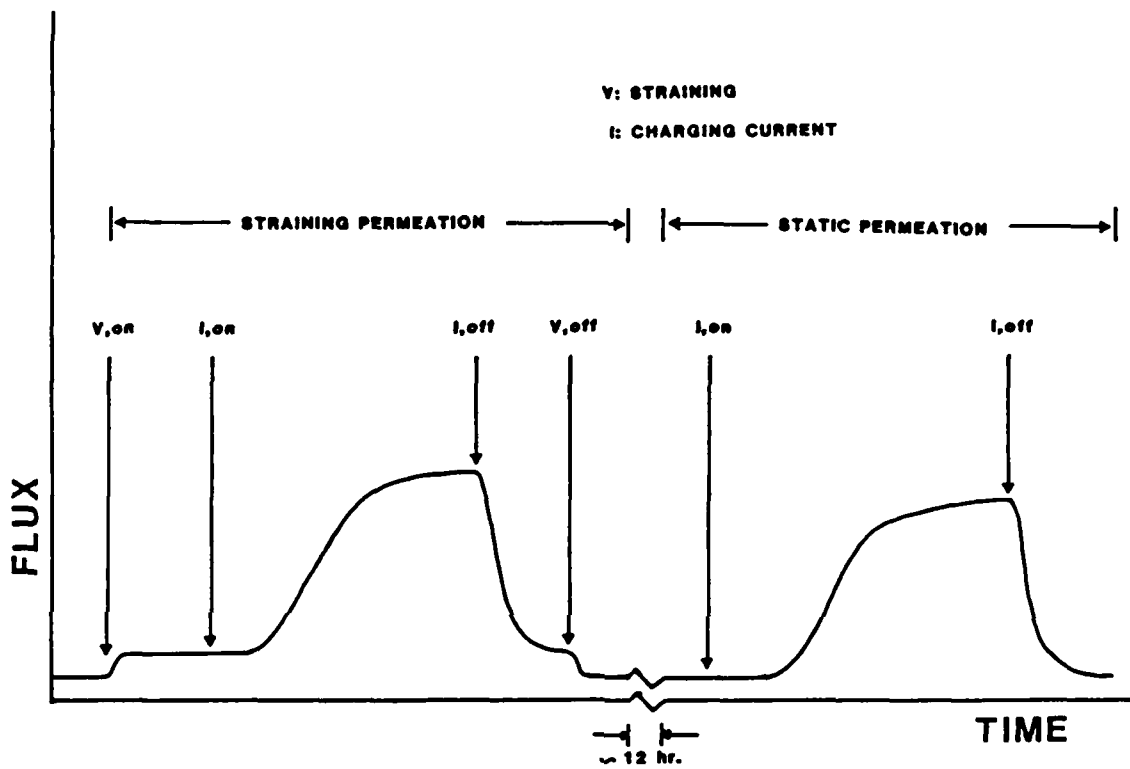


Figure 4-11: A test procedure for consecutive straining and static permeation tests.

without straining, calculated from breakthrough time, was evaluated. This test procedure was repeated at least three times and the order of straining permeation and static permeation exchanged to reduce the data scatter and any ambiguity due to the minor differences in the microstructure resulting from different strains.

#### 4.6. Supersaturation Study

In the course of this study, various characterization techniques were employed as necessary to study the possibility of hydrogen supersaturation at potential failure sites, associated with dislocation transport of hydrogen.

The charging conditions used in the straining permeation test are not sufficient to cause any hydrogen supersaturation(177), at least as manifested by surface blisters or cracks. However, by studying the dislocation structure present after the straining permeation test, using transmission electron microscopy, possible changes of dislocation structure particularly associated with potential crack initiation sites could serve as evidence for the presence of supersaturation effects, perhaps leading to strain localization.

Transmission electron microscopy was conducted on both a JEOL 100C and 120CX instrument. Specimens taken from straining permeation tests were first removed from the holder and mechanically thinned on 600 grit sand paper followed by chemically thinning in a 92%  $H_2O_2$  plus 8% HF solution to a thickness of 0.10 to 0.13 mm. At this point, 3 mm diameter discs were carefully cut, using standard TEM foil disc puncher, from both the center area where hydrogen charging was performed and the hydrogen free peripheral area within the gauge section. Note that both charged and uncharged specimens were cut from the same specimen; thus the specimen preparation history and the total strain were identical; the only difference between them is that during straining one was continuously charged with hydrogen and the other was not.

Final preparation was carried out on a FISCHIONE<sup>6</sup> twin-jet electro-polisher, until a perforation on the order of 100-800  $\mu m$  in diameter was made. The electrolyte employed was 70% methanol plus 30% nitric acid at a

---

<sup>6</sup>Trade name of E.A. Fischione Instrument Manufacturing.

temperature of -60 °C to -50 °C. The operating potential was 10-15 V and the optimum specimen current was found to be 10 mA. Upon perforation, the specimen was thoroughly rinsed in methanol and stored in ethanol prior to examination, in order to minimize oxidation. Alternatively, other electrolytes consisting of sodium chromate plus glacial acetic acid (room temperature polishing) or consisting of perchloric acid plus butanol and methanol (subzero temperature polishing) were used(195) to ensure the absence of polishing-induced microstructural artifacts. It was found that the microstructure was unaltered by polishing technique; however the first solution gave the best resultant thin foils.

Since the specimens were strained within the stage I work hardening range, the primary slip system should be dominant in the dislocation structure, and its presence was used to identify the thin foil orientation with respect to the tensile axis on the original single crystal. The orientation relationship of the subsequent microstructure features could then be uniquely determined.

To further correlate changes in such microstructural features as dislocation arrays to hydrogen effects, single crystal specimens with known orientations were heavily charged in a 1N sulfuric acid plus 10mg/l  $\text{As}_2\text{O}_3$  poision solution at  $20 \text{ mA/cm}^2$  for various times ranging from 1 hour to 24 hours. This charging condition has been shown to exceed the critical hydrogen concentration for generating surface blisters and internal/external cracks(178-180). By studying the locations and shapes of these defects as well as the propagation path and mechanism, the characteristic features of defects induced by hydrogen cathodic charging could be determined and compared to TEM results. This activity was performed using light microscopy and a CamScan series IV scanning electron microscope operating at 25 kV.

Finally, the rod specimen used for determining the crystal orientation (see section 5.1) was also employed to further study the comparative nature of hydrogen induced defects as revealed by TEM and SEM. The rod was used for a straining electrode test (SET) in a 0.1N NaOH solution at  $0.5 \text{ mA/cm}^2$  charging current density and at  $8 \times 10^{-7} \text{ sec}^{-1}$  strain rate, strained to about 3% total strain (10 hours). Following this, the rod was subsequently charged with hydrogen in 1N sulfuric acid plus 10 mg/l  $\text{As}_2\text{O}_3$  poision solution at  $30 \text{ mA/cm}^2$ . This charging process employed was to accelerate and to closely

monitor any surface blistering or crack formation, and to study the initiation stage of such damage. Surface defects were observed using the techniques mentioned above, and the different types of damages for both heavily hydrogen charged and straining plus hydrogen charging were analyzed and compared.

## Chapter 5

### RESULTS AND DISCUSSION

#### 5.1. Single Crystal Orientation Determination

The most convenient technique used to identify single crystal orientations is the back-reflection Laue X-ray diffraction which can be applied to specimens of various sizes and thicknesses. In the present work this was carried out using a tungsten target, operated at 40kV and 35mA.

**Table 5-1:** Summary of different crystal orientation used in this study.

| <u>Crystal</u> | <u>Tensile Axis</u> | <u>Surface Plane</u> | <u>Slip System</u> | <u>Schmid's Factor</u> |
|----------------|---------------------|----------------------|--------------------|------------------------|
| SCREW          | [553]               | (110)                | (112)[111]         | 0.45                   |
| EDGE           | [233]               | (311)                | (211)[111]         | 0.43                   |
| MIXED          | [323]               | (331)                | (121)[111]         | 0.43                   |

Table 5-1 summarizes the orientation relationships of the single crystals used in this thesis. Laue diffraction patterns are indexed in Figure 5-1, together with the associated stereographic projections, as shown in Figure 5-2. The stereographic projections, generated by a computer program using similar zone axes to the crystal surfaces, are shown in Figure 5-3. This program, available in many computer software libraries, is capable of plotting various zone axis stereographic projections for different crystal structures and has been used to confirm the indices in the stereographic projection derived from Laue patterns. Comparing the projections in Figure 5-2 and Figure 5-3, it is clear that within a few degrees of mismatch, the experimentally identified crystal orientations are correct. Observed differences are inevitable due to difficulties in accurately aligning the specimen mounting device, or to the crystal surface being slightly off the determined orientation. It is believed that in either case, this will not cause problems in subsequent interpretation.

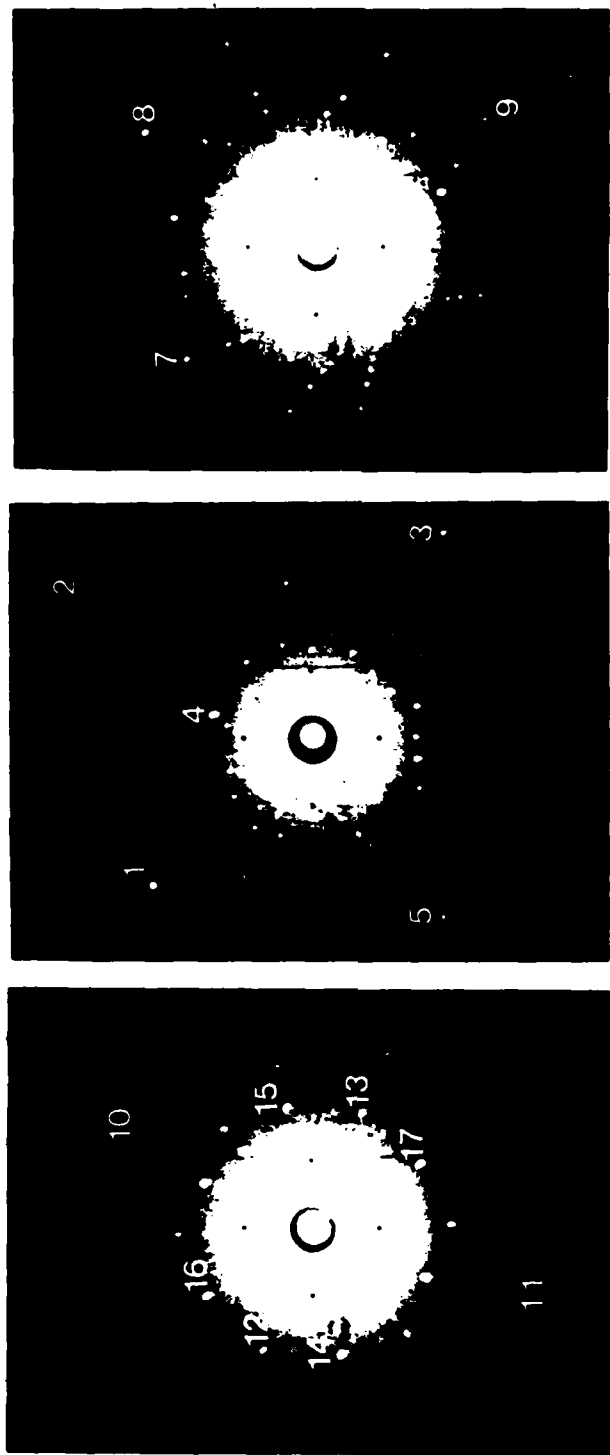


**Figure 5-1:** Laue patterns for three crystals used in this study. The numbered spots were indexed in the Figure 5-2.

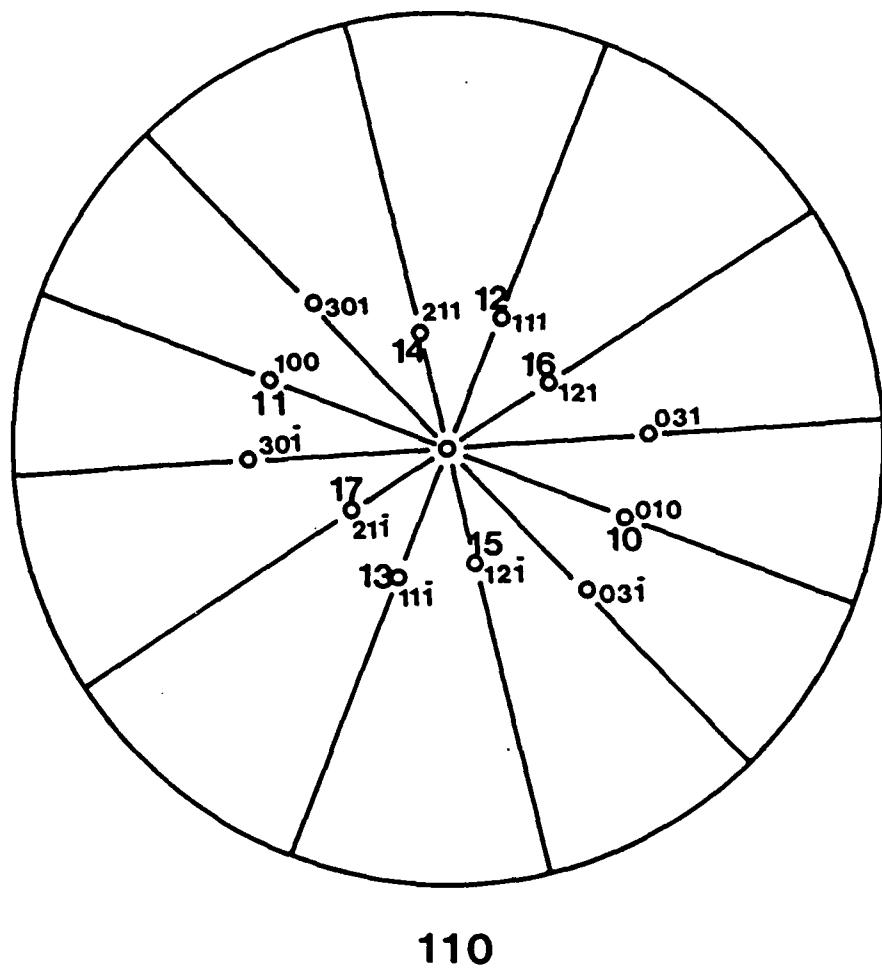


Figure 5-2: The stereographic projections deduced from Laue pattern shown in Figure 5-1.

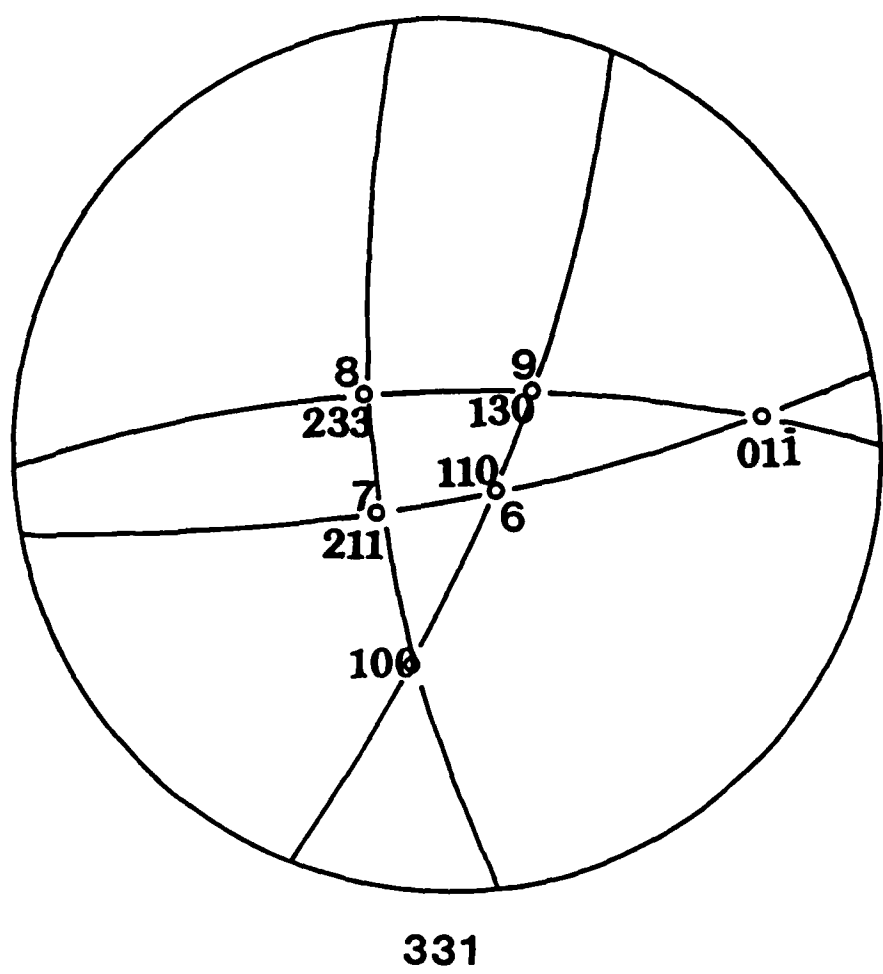
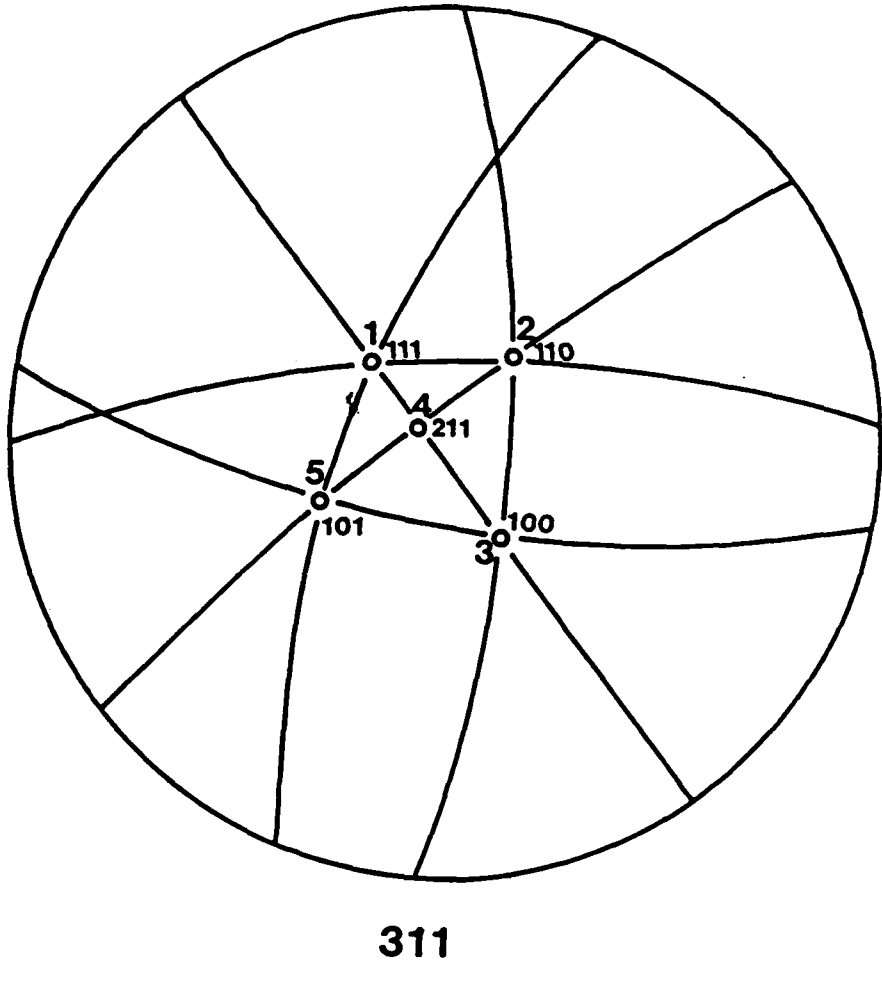


Figure 5-2: The stereographic projections deduced from Laue pattern shown in Figure 5-1.



**Figure 5-2:** The stereographic projections deduced from Laue pattern shown in Figure 5-1

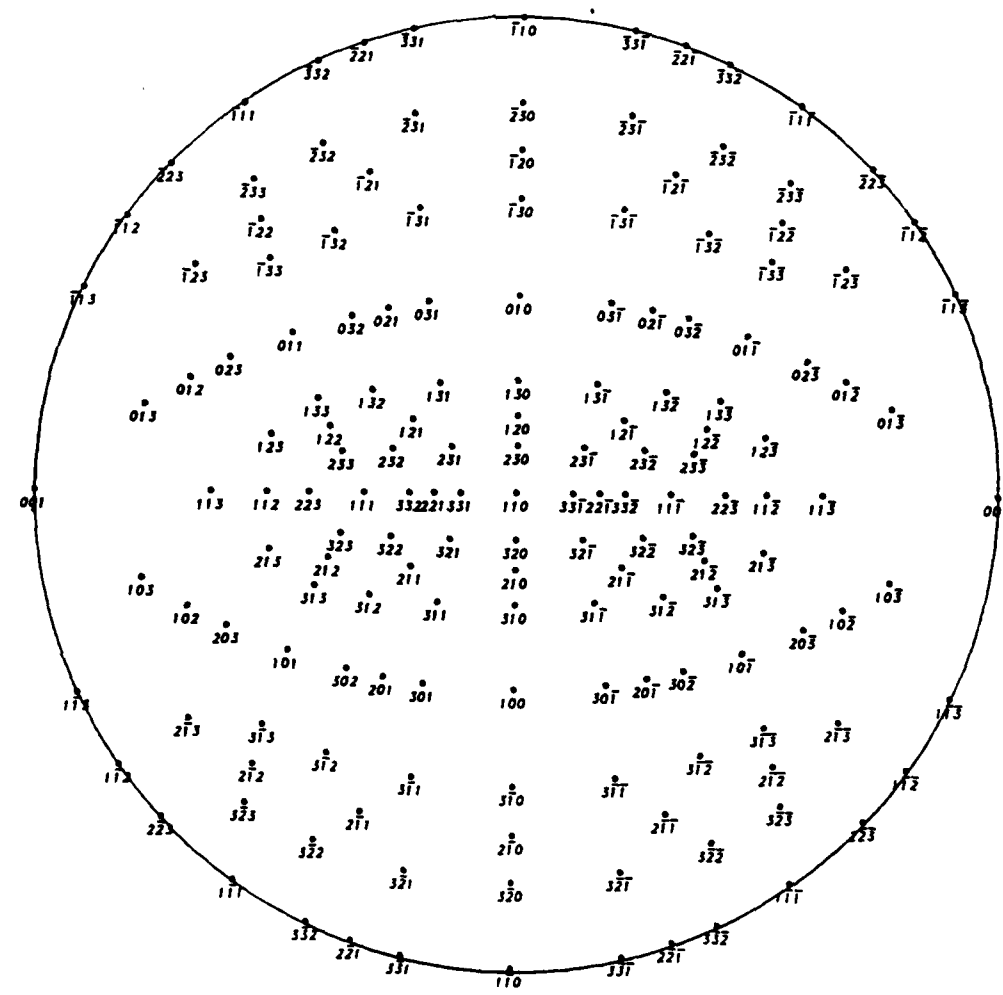
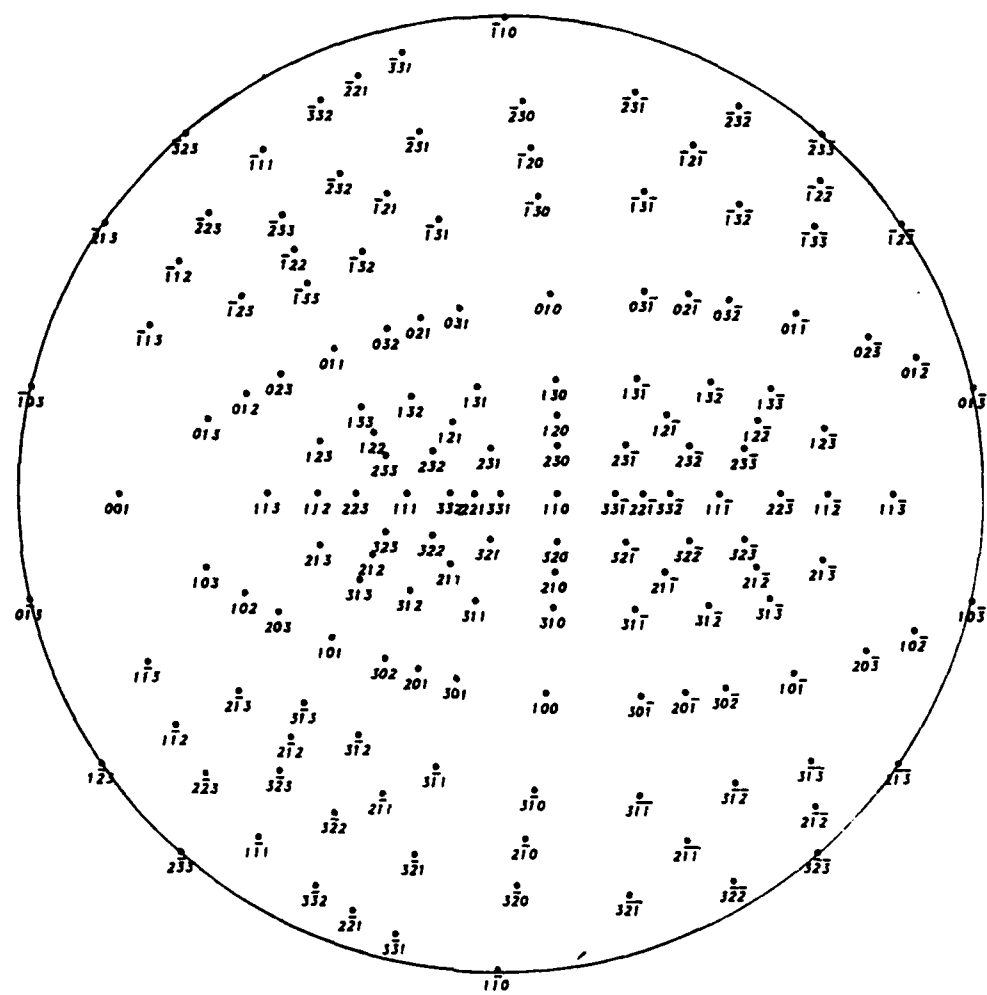


Figure 5-3: Stereographic projections plotted by a computer for three identical zone axes as those in Figure 5-2.



**Figure 5-3:** Stereographic projections plotted by a computer for three identical zone axes as those in Figure 5-2.

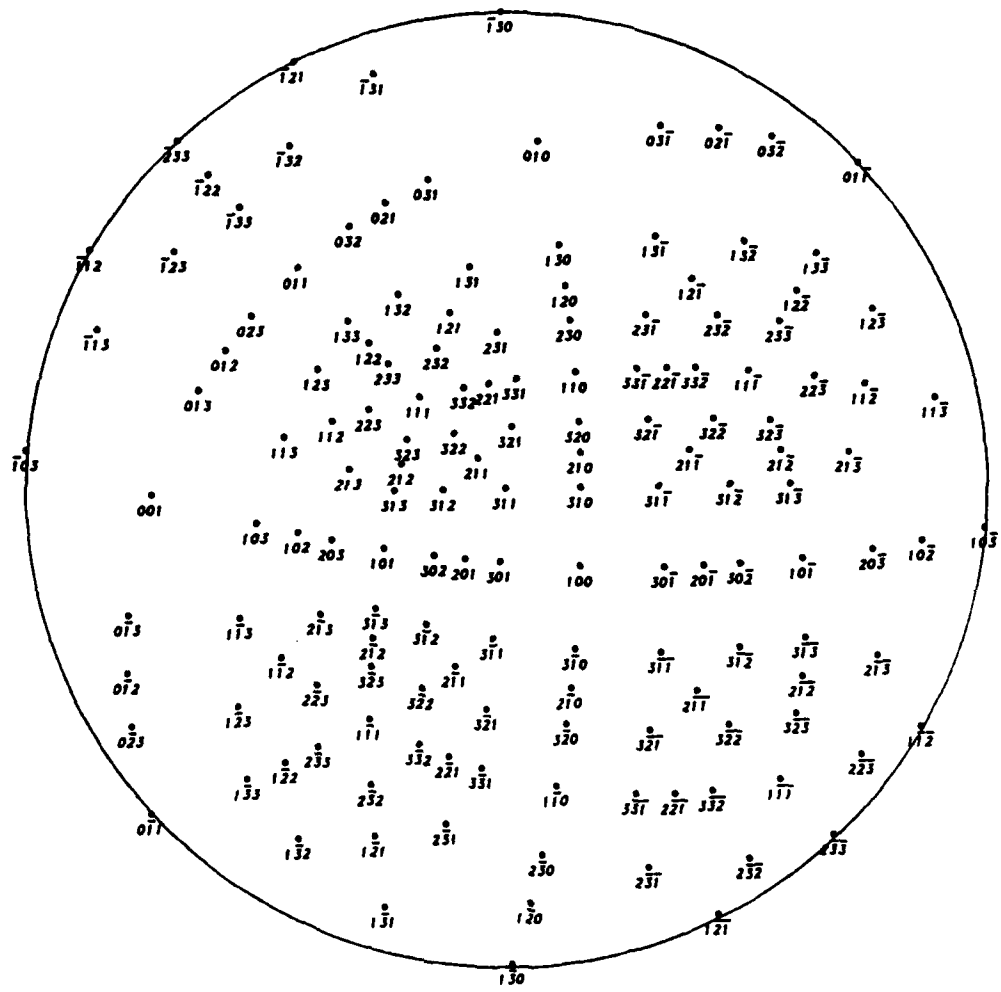


Figure 5-3: Stereographic projections plotted by a computer for three identical zone axes as those in Figure 5-2

The results shown above provide confidence that the crystal surface is identified, thus allowing the proper tensile axis to be selected and crystal surface accurately prepared by cutting to the desired orientation combinations required for this study.

Figure 5-4 shows the three combinations of surface orientation and tensile axis, together with the primary slip system predicted from Schmid's factor for each case; this is also summarized in Table 5-1. To illustrate the choice for the type of dislocations intersecting the crystal surface during plastic deformation, consider the "screw orientation" crystal. The intersection between the predicted slip plane and the surface plane is [111] which is parallel to the predicted Burgers vector, and therefore the dislocation segments exiting the crystal surface have to be screw in character. Similar arguments can be applied to the other two orientations of choice; e.g. in "edge orientation" crystals, the intersection of the crystal surface and the predicted slip plane is perpendicular to the predicted Burgers vector, whereas in "mixed orientation" crystals, the same intersection is 45° away from the predicted Burgers vector.

#### 5.1.1. Slip System Determination

The next step was to confirm the operative slip systems for each of the specimens used to study the dislocation transport phenomenon, to ensure that the hydrogen-carrying dislocations exiting from the output surface of a straining permeation test are of the proper type. To accomplish this, the single crystals were cut to the predetermined orientations, with a final specimen size of 0.2 cm square cross section and 3 cm in length, and were then chemically shaped, using the solution previously described, to form a 1.5 cm gauge length, as shown in Figure 5-5. These specimens were subjected to intermittent straining steps of 0.2%, 0.5%, 1.0%, 2.0%, 5.0%, 10.0%, and 20.0%. At each strain step, two mutually perpendicular surfaces were examined by scanning electron microscopy and analyzed to identify the dominant slip system. This was accomplished by using standard analyses of surface slip traces, taking into account necessary corrections for tilts within the SEM. This analysis was aided by the presence of two parallel razor blade marks placed on both single crystal surfaces perpendicular to the tensile axis, which served the purpose of providing a simple means of returning to the same

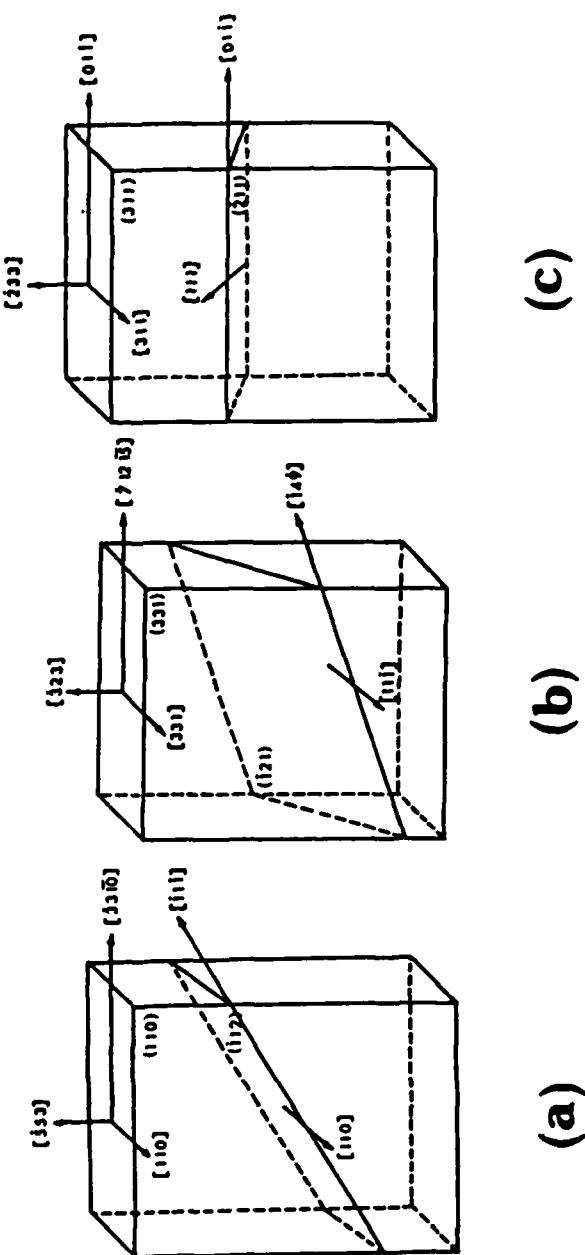


Figure 5-4: Three crystal orientations used in this study, with the predicted primary slip systems. (a) screw orientation, (b) mixed orientation, (c) edge orientation.

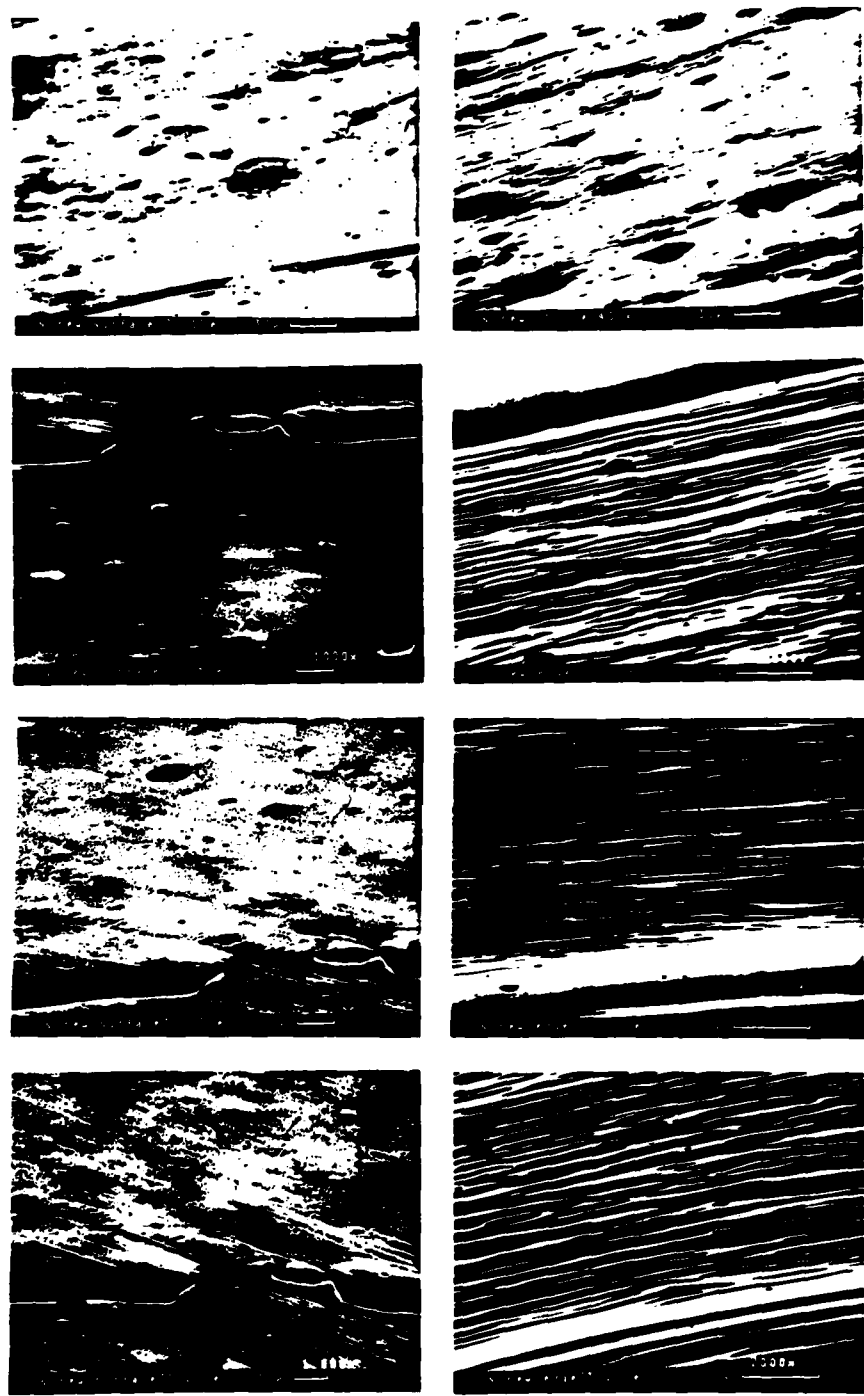


Figure 5-6: Single crystal surfaces showing slip traces at different total strain for "screw orientation" crystal.

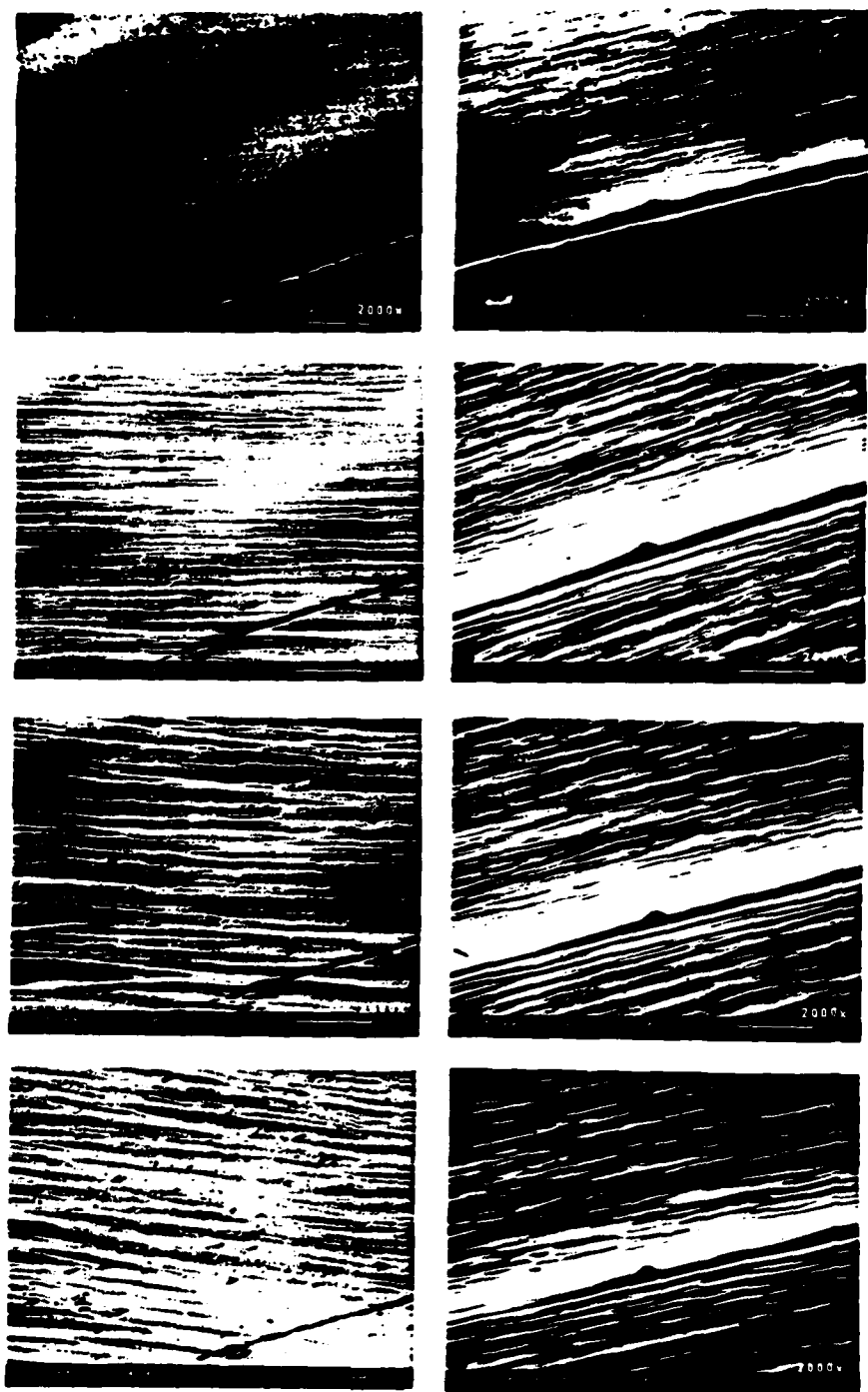
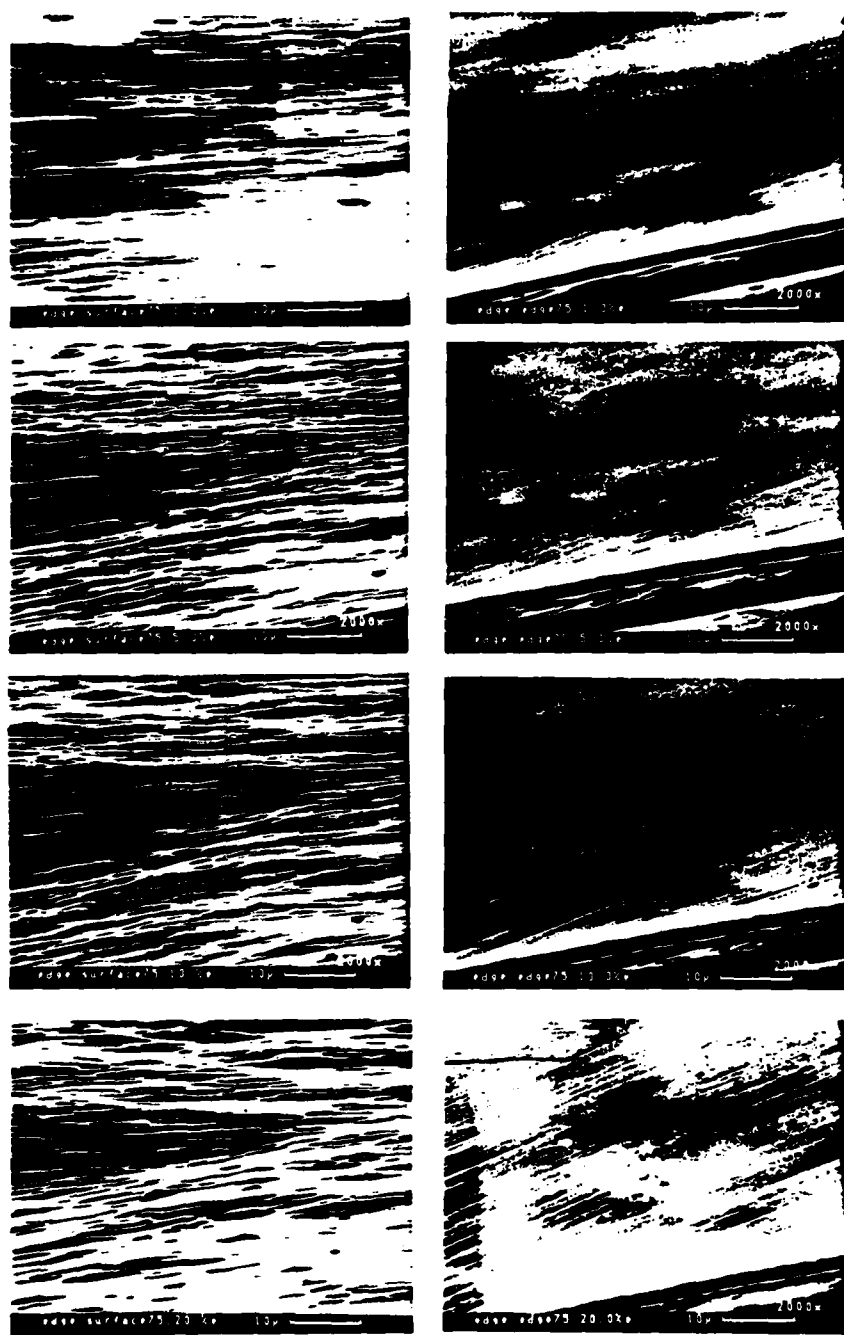


Figure 5-7: Single crystal surfaces showing slip traces at different total strain for "mixed orientation" crystal.



**Figure 5-8:** Single crystal surfaces showing slip traces at different total strain for "edge orientation" crystal.

**Table 5-2:** Temperature range (K) below which the cross slip of screw dislocations is unlikely in bcc crystals.

| <u>Fe</u> | <u>V</u> | <u>Nb</u> | <u>Ta</u> | <u>Mo</u> | <u>W</u> |
|-----------|----------|-----------|-----------|-----------|----------|
| 200-300*  | 77-300   | 230       | 300       | 350-400   | >300     |

\* Depending on the purity of crystals; the purer the crystal, the lower the temperature.(98,120)

It is also important to be able to accurately describe both the individual and interactive dislocation behaviors during plastic deformation at room temperature. From numerous literature studies(124,181-185), it is clear that for the bcc crystal structure screw dislocations move more slowly than edge dislocations at temperatures lower than and generally including room temperature(120). During plastic deformation edge and other non-screw dislocations segments will thus move out of the specimen at the very early stages of plastic deformation; the screw dislocations left behind or subsequently generated will then contribute to and largely control the subsequent plastic flow and macroscopic mechanical properties. The temperature regions where this phenomenon has been observed for different bcc materials are summarized in Table 5-2, and for iron room temperature is within this behavior regime.

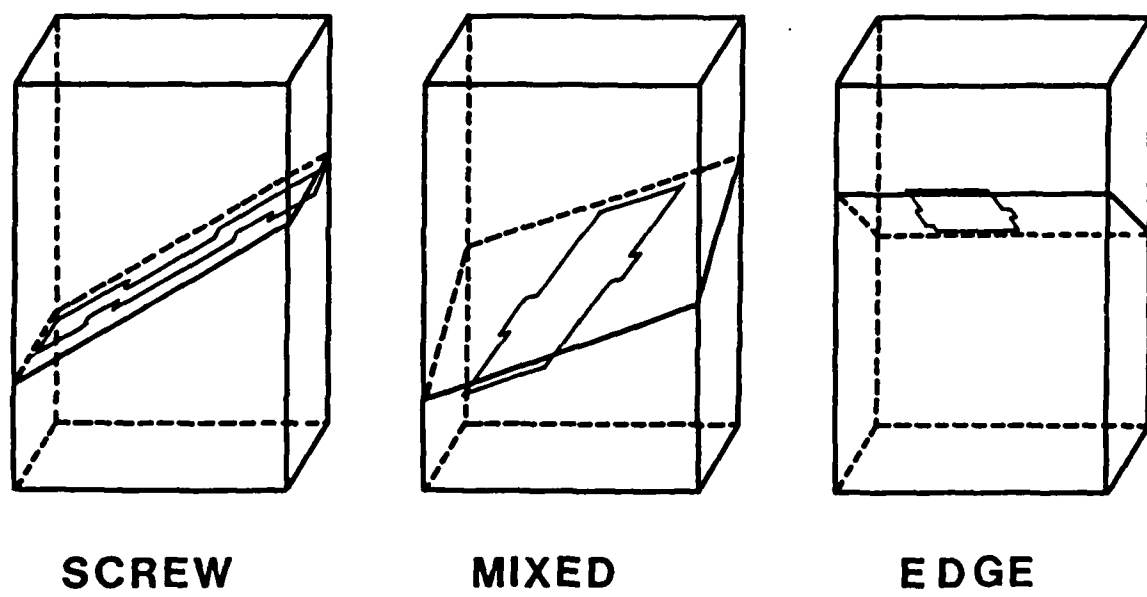
To validate this prediction for the present study, TEM was performed on several differently oriented single crystals to identify the types of dislocation present at different strain levels. Our findings are consistent with the literature predictions. As shown in Figure 5-9, the majority of dislocation lines are always parallel to the  $\langle 111 \rangle$  direction, implying that they are screw in character. Another observation worthy of mention is that in those crystals oriented such that edge dislocations intersect the specimen surface, the dislocations remaining within the crystal are very short and tend to line up on the same slip plane. It is believed that these screw segments penetrate the thin foil from top to bottom, and thus their length is determined by the foil thickness. In contrast, for those crystal surfaces oriented for screw intersection, the dislocation lines are much longer and cover a large area of the foil, consistent with predictions. In other words, since plastic deformation is controlled by the motion of screw dislocations, the remaining dislocation lines available for observation will always be screw in character no matter how the crystal is oriented. To reinforce this point, Figure 5-10 shows in

sketch form the expected dislocation configurations for edge and screw oriented during the easy glide strain region when only primary slip should be predominant.

### 5.2. Possible Surface Effects on Straining Permeation Test

Although the conventional permeation test was established more than twenty five years ago(176), incorporation of this technique with straining (straining permeation test) is a rather non-standard testing technique. Questions concerning it have been raised and discussed(86-90) and make it clear that to successfully adopt this technique a number of concerns and precautions are needed. The most critical and potentially greatest problem is the possible presence of uncontrollable surface effects during straining(92). Since the electrochemical properties of the dynamically strained surface may be very different from that of a static surface, it is thus important to independently investigate surface effects in order to ensure unambiguous interpretation of the results.

The surface effect tests were carried out using identical specimens and techniques as for the straining permeation test, except that there was no hydrogen introduction; i.e. no charging current was applied to the cathodic surface of the specimen during the entire test. Hence, any change in anodic current monitored on the output surface can be legitimately ascribed to a strain-induced surface effect. The results of these tests for single crystals, as well as for polycrystalline iron, are shown in Figure 5-11. Before the onset of abnormal noise (whose appearance was very irregular and which always occurred at strains greater than ever used in the straining permeation studies), the anodic current slowly increases without showing any observably distinct noise. The rising rates of these so-called "background" currents are much slower than those ever observed in changes of the steady state flux due to the straining, especially for the case of higher strain rates, as will be presented shortly. Therefore, for this kind of test, any surface reaction effects induced by the straining appear to be insignificant. Further, the integrity of the palladium layer on both the input and output surfaces was studied by SEM and X-ray surface chemical analysis before and after the abnormal flux occurred. It was concluded that the abnormal behavior invariably starts at the onset of rupture of the coated palladium layer, as



**SCREW**

**MIXED**

**EDGE**

**Figure 5-10:** Possible dislocation loop configuration on the primary slip plane for differently oriented single crystals.

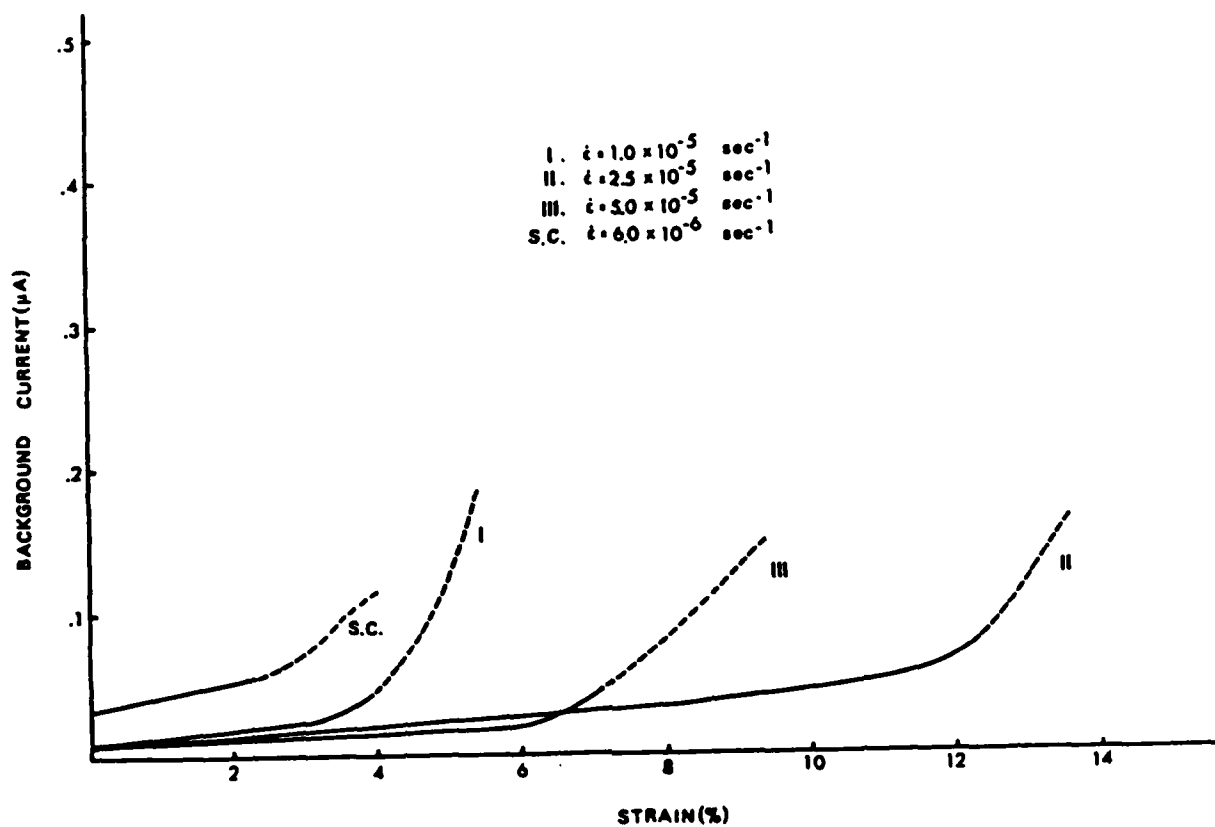
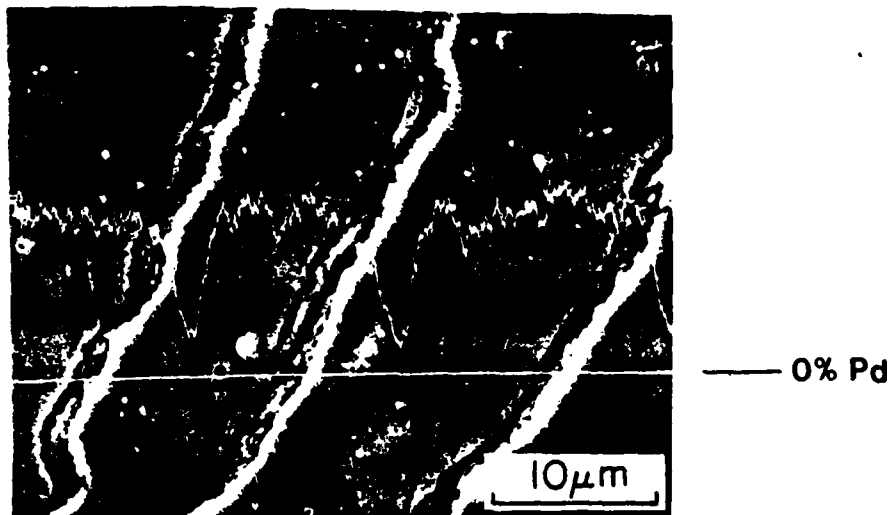


Figure 5-11: The anodic surface effect due to dynamical straining of single crystal and polycrystalline iron at various strain rates.

shown in Figure 5-12, and this observation provided an upper limit strain to the straining permeation tests.

In the case of the single crystals, the strain at which the abnormal background noise associated with loss of Pd integrity was found to be smaller than that for polycrystals. This difference is attributed to the less homogeneous plastic deformation on the single crystals, especially within the easy glide strain. Once the height of a slip step on the surface is large enough to completely penetrate the coated palladium layer, the noisy flux signal will appear due to the dissolution of the iron exposed on the active slip step.

In the following sections, the straining permeation tests conducted on single crystals and polycrystal specimens will be separately presented. Due to the precisely defined dislocation behavior during plastic deformation for the



**Figure 5-12:** SEM micrograph accompanied with X-ray of Pd signal showing the rupture of Pd layers after straining.

former, the single crystal straining permeation illustrates in a more controlled manner the interaction between dislocations and hydrogen. Importantly they also yield the best possible quantitative measurements of the hydrogen transport rates by different dislocation types, as a function of strain rate, lattice hydrogen concentration and temperature. In contrast, the straining permeation test results obtained from the polycrystal specimens can be better used to illustrate the relative contribution and importance of trapping and transport, since during plastic deformation complex multiple slip systems are activated, and the sessile dislocation density increases rapidly, giving rise to a significant hydrogen trapping effect.

### 5.3. Straining Permeation Tests for Single Crystals

It is believed that the observed transport and trapping phenomena during straining permeation tests result from coupled interactions between hydrogen and dislocations which are in turn sensitive to the non-uniform nature of straining, particularly in single crystals oriented for single slip. To better appreciate the importance of the heterogeneous strain history, results will be

presented in two different ways; first, a more qualitative description and rationalization of how the interaction between hydrogen and dislocations can give rise to different kinds of flux behaviors will be presented; and then a more quantitative assessment will describe the velocity and concentration of hydrogen as it is carried (or perhaps trapped) by different dislocation types. The dependence of this effect on such parameters as strain rate, hydrogen concentration and temperature will also be presented.

### 5.3.1. Qualitative Description of Straining Permeation and Flux Phenomena

Single crystals of three different surface orientations, as shown in Figure 5-4, were used to investigate the interdependence of possible hydrogen transport steps to the dynamics of dislocation motion within the easy glide regime. Since the crystal orientation effectively influences the dislocation behavior during plastic deformation, it is conceivable to have different hydrogen flux phenomena during a straining permeation test for differently oriented crystals. For screw dislocations, as described previously, a single crystal with a (110) surface was cut to obtain a specimen with a [553] tensile orientation. For this orientation only the single slip system  $(\bar{1}12)-[\bar{1}\bar{1}1]$  is initially operating, and a long easy glide strain of about 20% exists, where largely unimpeded dislocation motion occurs. The specimen surface at which hydrogen was detected during permeation was intersected primarily by screw dislocation segments, particularly for small strains.

The detailed test sequence was as follows: After a stable background current was reached, a charging current density of  $0.37 \text{ mA/cm}^2$  was applied, small enough to avoid any complication due to undesirable effects such as Joule heating (see Section 2-1 for a detailed description) and possible irreversible microstructure effects, until a static steady state flux was reached. Straining was then imposed at a constant rate and corresponding changes of steady state flux were recorded continuously by a strip chart recorder and also monitored electronically by a fast response microprocessor.

In the case of screw dislocations, the steady state flux before and after straining is shown in Figure 5-13, together with the corresponding stress-strain curve. Initially a decrease in steady state flux, less pronounced than in polycrystals (as will be seen in the next section), occurred after plastic

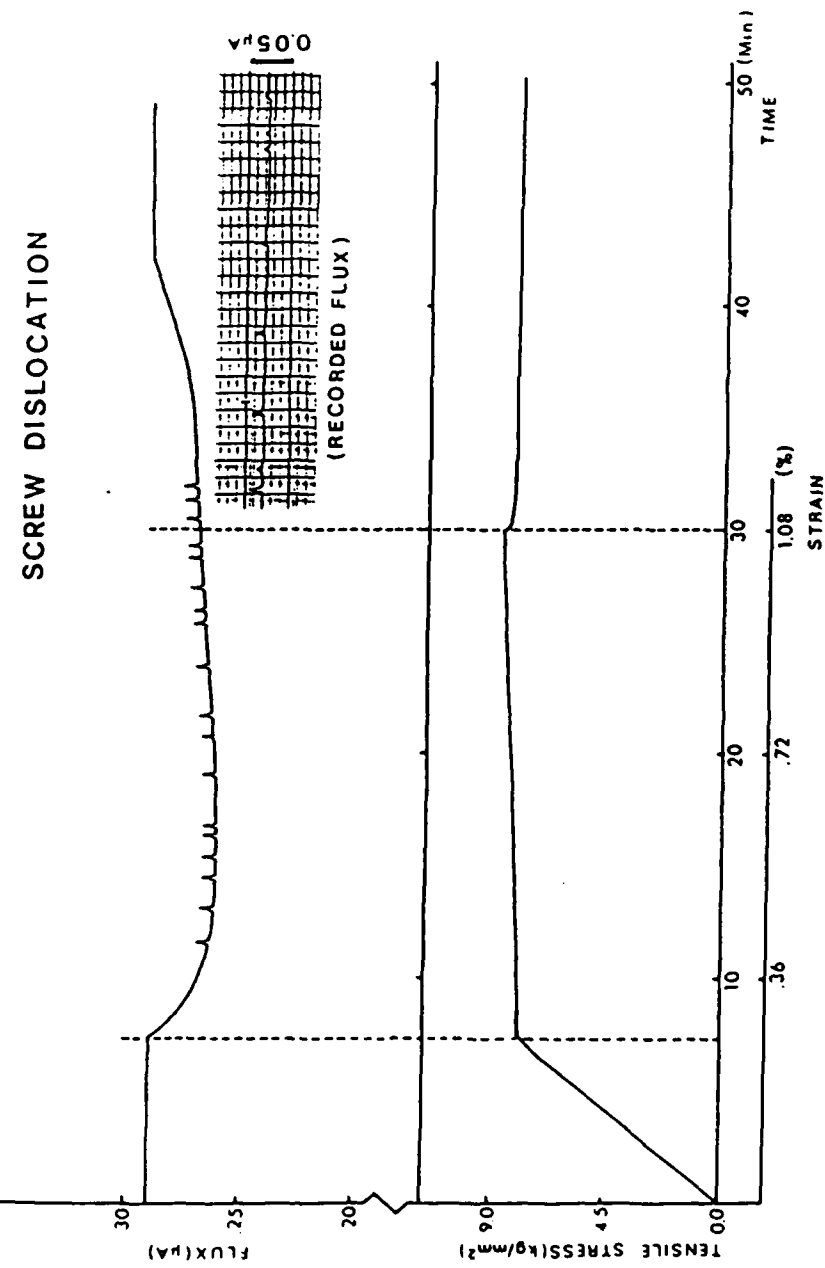


Figure 5-13: Typical changes of steady state hydrogen flux due to concurrent plastic deformation for screw orientation single crystal.

yielding, consistent with previous test data(186) and believed due to a trapping effect from the rapid multiplication of dislocation density attendant to the onset of plastic strain(187). The steady state flux then continuously decreased until a pronounced peak, with a height higher than the steady flux, of about  $0.005 \mu\text{A}$  was observed. This is shown in Figure 5-13, together with the direct recorded data from the strip chart recorder. During the remainder of the test, similar peaks were occasionally found. The overall flux also began to steadily increase. After the cessation of straining, the peak phenomenon persisted for the first two to three minutes, a result consistent with continued dislocation egress associated with stress relaxation(188). The flux then gradually and smoothly increased to a steady state level usually somewhat higher than the original steady state level. This increase in steady state flux is believed associated with a slight increase of apparent hydrogen solubility resulting from the increase in dislocation density during straining, and thus an increased permeability. The slow process of this increasing flux toward a new steady state value is believed to be a result of a gradual diminution of trapping due to fewer newly generated sessile dislocations, while in turn, previously mobile dislocations now also stop and became traps for lattice hydrogen. This explanation is consistent with the literature(189) that mobile dislocations generally have a smaller associated hydrogen concentration than do sessile dislocations. Thus these rather complicated flux contributions from the increasing total dislocation density, and a diminishing of the trapping effect from sessile dislocations, and the transport effect by mobile dislocations, as well as the presence of the trapping effect from "once-mobile" dislocations, result in the observed increased steady state flux.

As previously discussed, it is important to have confidence that the observations are associated only with dislocation transport. Although the observed peak heights are of the same magnitude as the total uncertainty associated with the type of experimental set-up, as discussed in Section 4.4, this strong peaking behavior was only found during plastic straining and only for this particular screw oriented crystal. Further the fact that the above phenomenon was consistently found for a number of similarly oriented single crystal specimens as well as in consecutive straining permeation tests on the same specimen, is convincing evidence that the peaks are not simply experimental artifacts associated with test technique or the specimen

preparation process, but are much more likely related to emission from the surface of the hydrogen transported by slip bands consisting primarily of screw dislocations. Further, there was no evidence for any abnormal background noise during the first few percents of strain where the straining permeation tests were conducted, and thus it is concluded that unexpected or unaccounted surface effects did not interfere with the recorded flux behavior.

A semiquantitative analysis of the peaking behavior was carried out using the assumption that the time interval between plastic yielding and the observation of the first peak, represents the travel time of dislocations through the entire specimen thickness. This allowed an estimate of the average dislocation velocity to be made, as well as the average mobile dislocation density. Table 5-3 summarizes the results of such an analysis, for three consecutive straining permeation tests on the same screw oriented crystal. The average dislocation velocities obtained were about  $10^{-4}$  cm/sec, in general agreement with reported literature data(190-191) of  $10^{-4}$  cm/sec to  $10^{-1}$  cm/sec for a range of applied stresses. A more accurate comparison with the present dislocation velocities appears to be not useful, due to the dependency of dislocation velocity on such parameters as crystal orientation, impurity content and strain rate. The corresponding mobile dislocation density, on the order of  $10^6$  cm/cm<sup>3</sup>, is also reasonable for such a well-annealed single crystal, at small strains.

Table 5-3: An estimation of average dislocation velocities and mobile dislocation densities for three consecutive straining permeation tests

| TEST | AVG. DISLOCATION VELOCITY<br>(CM/SEC) | MOBILE DISLOCATION DENSITY<br>(CM/CM <sup>3</sup> ) |
|------|---------------------------------------|---|
| 1    | $1.5 \times 10^{-4}$                  | $1.9 \times 10^6$                                   |
| 2    | $5.8 \times 10^{-6}$                  | $5.1 \times 10^6$                                   |
| 3    | $1.1 \times 10^{-4}$                  | $2.8 \times 10^6$                                   |

The peaking behavior can be regarded as due to the extra hydrogen transported by dislocations; concurrent hydrogen emission by lattice diffusion gives rise to the base line of the peak, which in this case is a stable value of about  $0.3 \mu\text{A}$ . The peak height can thus be used to estimate the total amount of hydrogen being transported out of the surface during the passage of slip bands. If the hydrogen concentration associated with dislocations can be estimated, then the number of dislocations needed to cause each peak can also be obtained, which would provide a check of the contention that the peaking phenomenon is directly related to the dislocation transport of hydrogen. Due to the lack of significant hydrostatic stresses around screw dislocations, any associated Cottrell atmosphere will be insignificant. However, as shown in Figure 2-3, there is significant interaction between hydrogen and a screw dislocation core as the binding energy is about 20 to 30 kJ/mole. This should result in a nearly saturated core atmosphere of hydrogen(189) for those screws near the hydrogen charged (hydrogen input) surface, where a sufficient quantity of hydrogen can be picked up by dislocations. Taking the atomic ratio of hydrogen to iron within the dislocation core as unity(189), and the lattice parameter of iron as  $2.87 \times 10^{-8} \text{ cm}$ , it is straightforward to show that a 1 cm long dislocation along the  $\langle 111 \rangle$  direction (screw) will consist of about  $4 \times 10^7$  iron atoms and the hydrogen concentration associated with this is then about  $4 \times 10^7$  atom H/cm. The experimental peak height found is about  $0.005 \mu\text{A}$ ; a simple dimensional conversion using Faraday's law shows that this is equivalent to  $3 \times 10^{10}$  atom H/sec. Dividing this number by the value of the estimated hydrogen concentration associated with screw dislocation shown above, it is estimated that each peak would require that about  $10^3 \text{ cm}/\text{cm}^2$  (surface density) of total dislocations move out of specimen surface within a short period of time. This value is consistent with an expected mobile density of  $10^6 \text{ cm}/\text{cm}^3$  (volume density), supporting our hypothesis that the observed peak is largely a result of the egress of hydrogen transported by screw dislocations originating at the input surface.

It should be noted that this simple calculation intrinsically implied that the mobile dislocations generated far from the hydrogen charging (hydrogen input) surface will not contribute to the peaking phenomenon. In fact, the possibility exists that mobile dislocations generated from the output surface (where hydrogen flux is monitored) may re-trap those hydrogen atoms being

transported to that area either by lattice diffusion or dislocation transport, and cause an "inverse" peaking phenomenon. Although this is considered rather unlikely, it was occasionally found that inverted peaking did occur during the straining permeation tests, and the above may be the explanation.

This more detailed calculation is also consistent with the earlier one, where the first peak was attributed to the hydrogen transported by dislocations passing through the entire specimen thickness, and the average dislocation velocity and the mobile dislocation density were evaluated. Both admittedly first order calculations support our contention that the observed discontinuous change in flux is associated with the emission of screw dislocations from the anodic (hydrogen output) surface.

In contrast, the results for those single crystals oriented such that edge or mixed dislocations exited the anodic detection surface, and performed under the same straining permeation condition as those for screw orientations, showed different behavior as shown in Figure 5-14 and Figure 5-15. In both cases, it can be seen that the flux fluctuated irregularly and no distinct peaks were found. This behavior is believed to be an obvious consequence of the nature of room temperature plastic deformation behavior in iron. In the edge orientation, the plastic flow within the single crystal is still dominated by the motion of screw dislocations, and therefore the hydrogen flux monitored in this orientation (as well as in the mixed orientation) is believed associated only with those edge (or mixed) kinks travelling along the screw dislocations, and which then intersect the monitoring crystal surface. Since the egression frequency of such kinks is faster and relatively more uniform than that of the long lengths of screw dislocations, it is reasonable to expect that the resultant hydrogen flux behavior will be less discontinuous and likely less dramatic, as was observed.

The irregularity of the flux behavior is believed to represent the hydrogen transport by dislocations (kinks), in addition to the lattice diffusion hydrogen flux, which in all cases should be smooth and steady. In the next section, these particular flux behaviors will be further analyzed in the best possible quantitative manner, to assess the hydrogen transport rates by different dislocation types under various given experimental conditions.

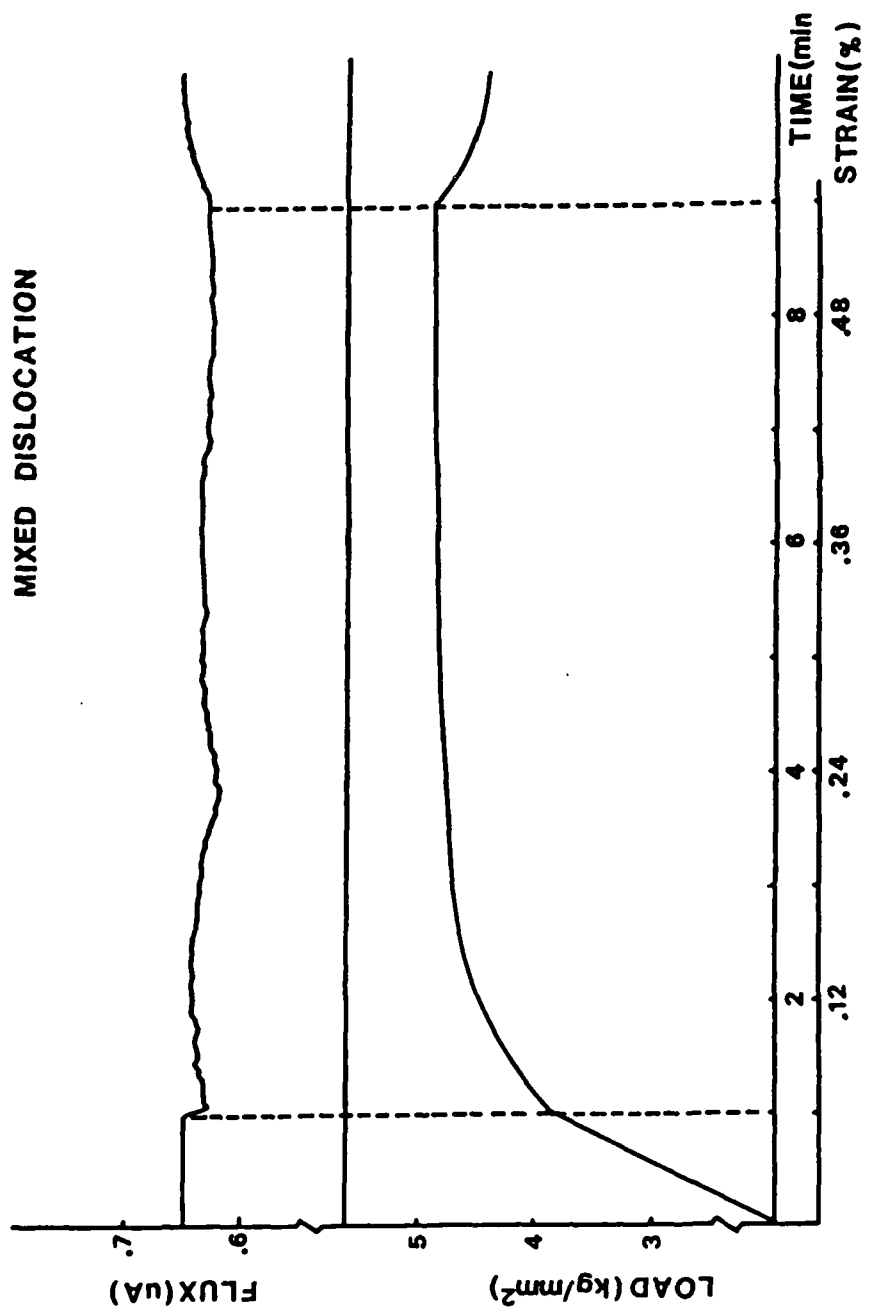


**Figure 5-14:** Typical changes of steady state hydrogen flux due to concurrent plastic deformation for mixed orientation single crystal.

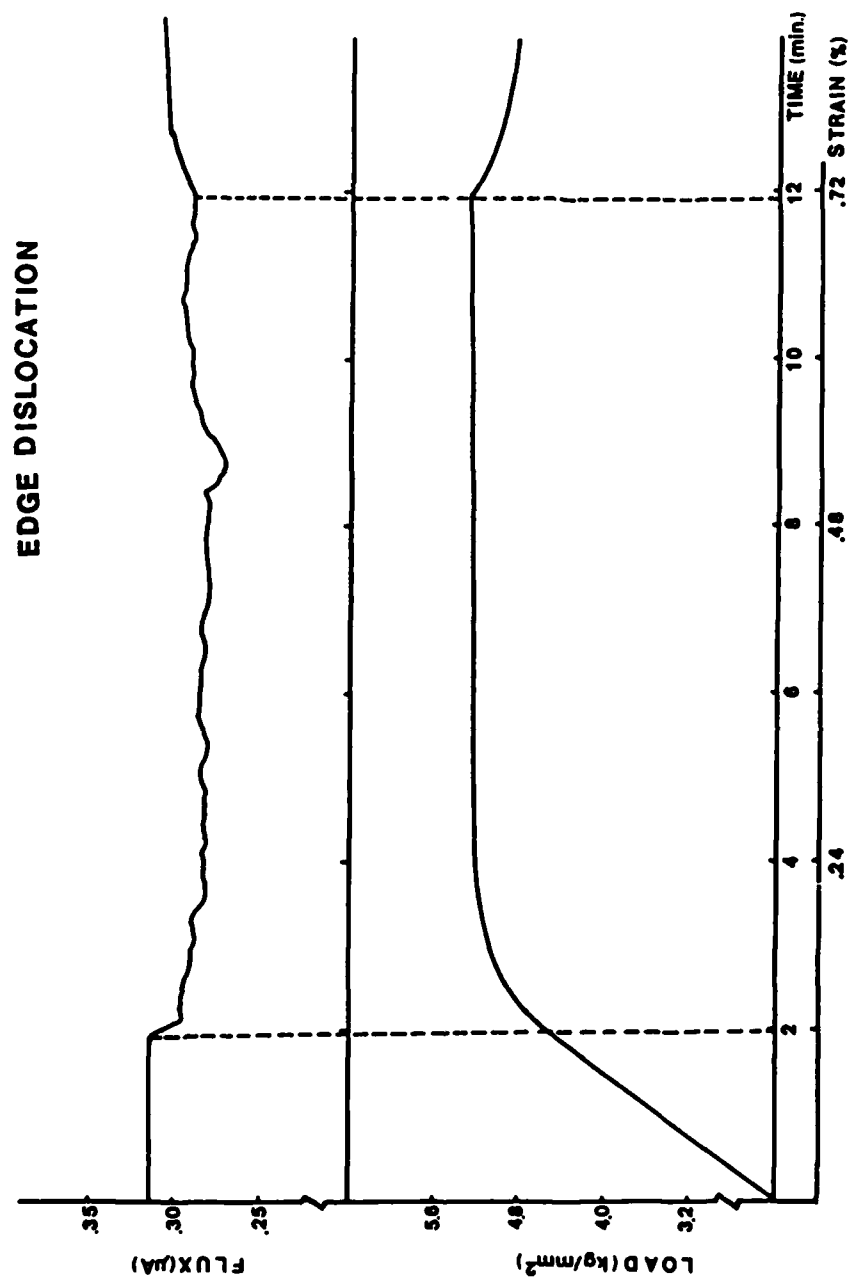


Figure 5-15: Typical changes of steady state hydrogen flux due to concurrent plastic deformation for edge orientation single crystal.

### 5.3.2. Quantitative Analyses

To understand in a more quantitative manner the overall picture of how hydrogen can be transported by mobile dislocations, it is necessary to undertake a much more systematic study of this phenomenon than described in the previous section. Towards this goal, parameters crucial to the transport mechanism, such as hydrogen concentration, strain rate, temperature have been employed as variables during the experiments as follows:

**Table 5-4:** Summary of straining permeation tests, giving the relation between test condition and designated code.

| CHARGING CURRENT<br>(mA/cm <sup>2</sup> ) | STRAIN RATE<br>(10 <sup>-8</sup> sec <sup>-1</sup> ) | SCREW   | EDGE    | MIXED   |
|---|--|---------|---------|---------|
| 0.5                                       | 800  | SSPT055 | ESPT055 | MSPT055 |
|   | 80   | SSPT056 | ESPT056 | MSPT056 |
|   | 8  | SSPT057 | ESPT057 | MSPT057 |
|   | 1.6  | SSPT058 | ESPT058 | MSPT058 |
| 1.0                                       | 800  | SSPT105 | ESPT105 | MSPT105 |
|   | 80   | SSPT106 | ESPT106 | MSPT106 |
|   | 8  | SSPT107 | ESPT107 | MSPT107 |
|   | 1.6  | SSPT108 | ESPT108 | MSPT108 |
| 2.5                                       | 800  | SSPT255 | ESPT255 | MSPT255 |
|   | 80   | SSPT256 | ESPT256 | MSPT256 |
|   | 8  | SSPT257 | ESPT257 | MSPT257 |
|   | 1.6  | SSPT258 | ESPT258 | MSPT258 |

Four initial strain rates and three different charging currents (i.e. different hydrogen concentrations) were used. Table 5-4 summarizes the tests conducted in this portion of study; each test was designated by a special code to illustrate the different test condition. The first letter in the code represents the dislocation type: S is for screw, E is for edge and M is for mixed

dislocations. The following letter, SPT, simply stands for straining permeation test. Following this four-letter code, the first two digit number represents the charging current density used: 05, 10, 25, represents respectively  $0.5 \text{ mA/cm}^2$ ,  $1.0 \text{ mA/cm}^2$  and  $2.5 \text{ mA/cm}^2$ . The last digit in the code represents the strain rate: 5, 6, 7, 8, represents, again respectively,  $8 \times 10^{-6} \text{ sec}^{-1}$ ,  $8 \times 10^{-7} \text{ sec}^{-1}$ ,  $8 \times 10^{-8} \text{ sec}^{-1}$  and  $1.6 \times 10^{-8} \text{ sec}^{-1}$ . (the actual initial strain rate measured directly from a sensitive LVDT device are reported in Table 5-5).

**Table 5-5:** Nominal strain rates measured from LVDT for all the tests conducted in this part of study.

| TEST | SSPT                  | MSPT                  | ESPT                  |
|------|-----------------------|-----------------------|-----------------------|
| 055  | $8.13 \times 10^{-6}$ | $5.70 \times 10^{-6}$ | $8.01 \times 10^{-6}$ |
| 105  | $8.12 \times 10^{-6}$ | $6.90 \times 10^{-6}$ | $9.24 \times 10^{-6}$ |
| 255  | $7.97 \times 10^{-6}$ | $6.95 \times 10^{-6}$ | $8.07 \times 10^{-6}$ |
| 056  | $8.03 \times 10^{-7}$ | $7.18 \times 10^{-7}$ | $9.49 \times 10^{-7}$ |
| 106  | $8.46 \times 10^{-7}$ | $7.55 \times 10^{-7}$ | $8.20 \times 10^{-7}$ |
| 256  | $8.29 \times 10^{-7}$ | $7.12 \times 10^{-7}$ | $8.92 \times 10^{-7}$ |
| 057  | $8.18 \times 10^{-8}$ | $6.90 \times 10^{-8}$ | $10.0 \times 10^{-8}$ |
| 107  | $8.06 \times 10^{-8}$ | $7.04 \times 10^{-8}$ | $8.39 \times 10^{-8}$ |
| 257  | $7.97 \times 10^{-8}$ | $7.14 \times 10^{-8}$ | $8.46 \times 10^{-8}$ |
| 058  | $1.69 \times 10^{-8}$ | $1.68 \times 10^{-8}$ | $1.55 \times 10^{-8}$ |
| 108  | $1.79 \times 10^{-8}$ | $1.63 \times 10^{-8}$ | $1.97 \times 10^{-8}$ |
| 258  | $1.64 \times 10^{-8}$ | $1.80 \times 10^{-8}$ | $2.04 \times 10^{-8}$ |

Examining the effects of temperature variations was more difficult experimentally since the flux was found to be very sensitive to temperature fluctuation of even one degree of centigrade, about the best control possible in these tests. While this control problem was less severe at or below room temperature, it becomes more serious as the temperature rises. Nevertheless tests were performed at  $12^\circ\text{C}$ ,  $24^\circ\text{C}$ ,  $45^\circ\text{C}$ , and  $78^\circ\text{C}$  for screw and edge dislocations respectively; tests under the same conditions were repeated

several times and the average values obtained, taken in an attempt to improve reliability. In the following section, the data analysis techniques will be discussed first and the effect of each parameter described above will be presented and the inter-relationship between them will be discussed.

### 5.3.2.1. Data Analyses Techniques

For each type of specimen (type of dislocation under study), the tests shown in Table 5-4 were done sequentially from lower to higher hydrogen input concentration and from higher strain rate to lower strain rate. The intention of this sequencing was to minimize the extent of differences in microstructure caused by imposing these variables, when comparing the results from one sequence to the other. Specifically, it should be noted that the only serious microstructural variation among each group of tests is the total strain, since the tests were performed on the same specimen; other microstructure variations such as impurity concentration were kept constant. It is believed that for crystals undergoing single slip, small variations in total strain should not have a major effect on results and likely any changes associated are smaller than and will be masked by the invariable degree of error present.

While the overall flux of hydrogen during the test is quite irregular, corresponding to the non-uniform dislocation motion, the variation is always around a fixed steady state value. This is because the main contribution of the flux during this type of test is still the lattice diffusion flux, as discussed in Section 4.5.1, which was kept as constant as possible to facilitate the detection of other transport mechanisms, such as in our case, dislocation transport. We have already speculated that the total flux consists of three major components, steady state lattice diffusion, trapping effects by newly generated sessile dislocations and the flux associated with hydrogen transported by mobile dislocations. To separate and differentiate these three components, we have assumed and we believe reasonably, that any interactions between these three components can be neglected and further that during straining, the steady state lattice flux will stay constant and the effect of trapping can only decrease the flux. The first assumption can be justified based on the kinetic nature of the dislocation transport process, where the equilibrium between lattice hydrogen and the hydrogen associated with dislocations may not be established during the transient time period of the

test, implying that the interaction between them is insignificant. In fact, once hydrogen is trapped inside the dislocation core, it likely would stay there even if the surrounding matrix is almost free of hydrogen, as indicated by Hirth(189,192) and others(95). The assumption that the steady state lattice flux stays the same during straining is clearly theoretically reasonable, although during the experiments, there were always fluctuations on the recorded flux, (discussed in Section 4.4.3) attributed to the background fluctuations and this represents either the resolution limit of this technique, or perhaps small changes in the steady state flux. The final assumption, that the effect of trapping can only decrease the flux, is easily rationalized by the fact that the trap density (in this case, sessile dislocation density) increases with straining which would definitely always reduce the total hydrogen flux. While it is difficult to justify *a priori* if these assumptions have established an upper or lower bound for the transport rate analysis, because of other various experimental errors, such as the stability of electrochemical cells, the temperature variations, we are convinced that the carefully devised experimental set-up used in this study (see Chapter 4 for details) has minimized experimental errors. Subsequently the validity of the results is only dependent on the physical reality of the modelling.

In this vein, this assumption of superposition of different concurrent hydrogen flux contributions allows us to construct a curve by connecting the lower points of the experimental curve, to obtain a curve comprising only steady state lattice flux and the effect of trapping. By then subtracting this from the original experimental curve, the remainder of the flux component is attributable to the quantity of hydrogen transported by dislocations. Figure 5-16 shows schematically how this approach was carried out: During the construction of this artificial curve, two adjacent data points were compared and the lower one used to construct the curve; for example, for data point C, the value of C was compared to that of B, since C is higher than B, C was replaced by C' which is equal to B. At point E, the value of E is lower than that of C', so point E was used. A similar approach was used to construct the entire curve using an iterative computer generated procedure. While there are many other ways to construct such an artificial curve, it is believed the approach adopted here most realistically mirrors reality allowing us to quantitatively evaluate the hydrogen transport rate by dislocations. In fact this

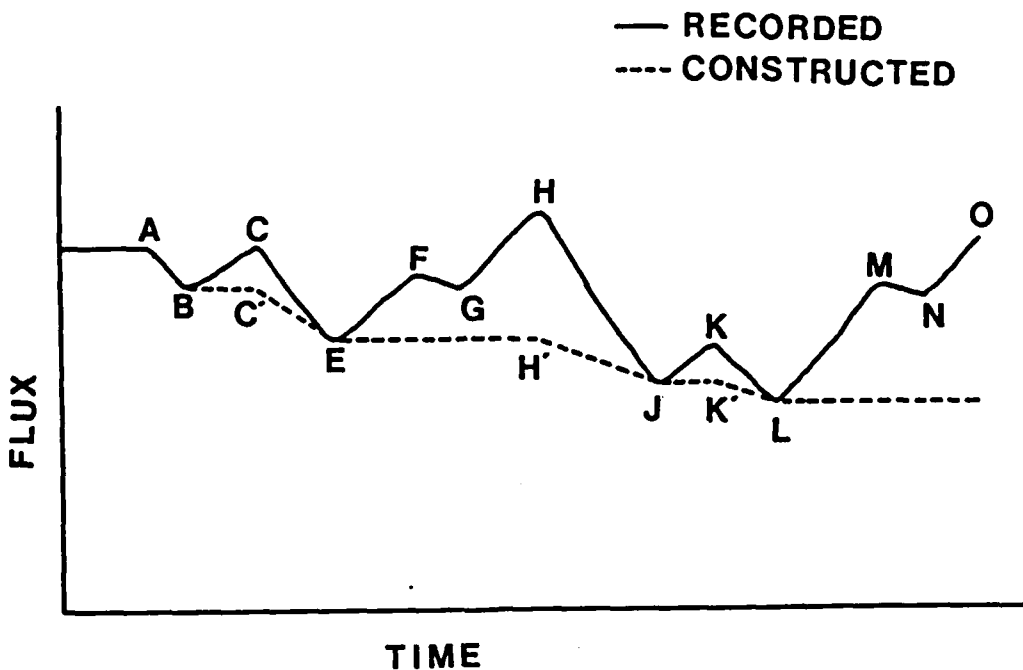


**Figure 5-16:** Curve stripping method used in separating hydrogen flux transported by dislocations from the total flux.

curve stripping method likely underestimates the hydrogen transport rate by dislocations since it only accounts for the relatively discontinuous portion of the dislocation-transport hydrogen flux; any contribution of transport to the continuous portion of this flux is indistinguishable from and is combined with concomitant trapping effects.

This curve stripping approach has been carried out for each of the different tests; the resultant curves for lattice diffusion and trapping are shown in Figure 5-17, and the dislocation transport component is shown in Figure 5-18 which itself reflects local averaging between the two closest data points to represent the amount of hydrogen being transported during a given time period. In the case of lattice diffusion and trapping, since similar curves were observed for different tests, only the range changes instead of each individual curve was plotted in Figure 5-17. In contrast, the transport

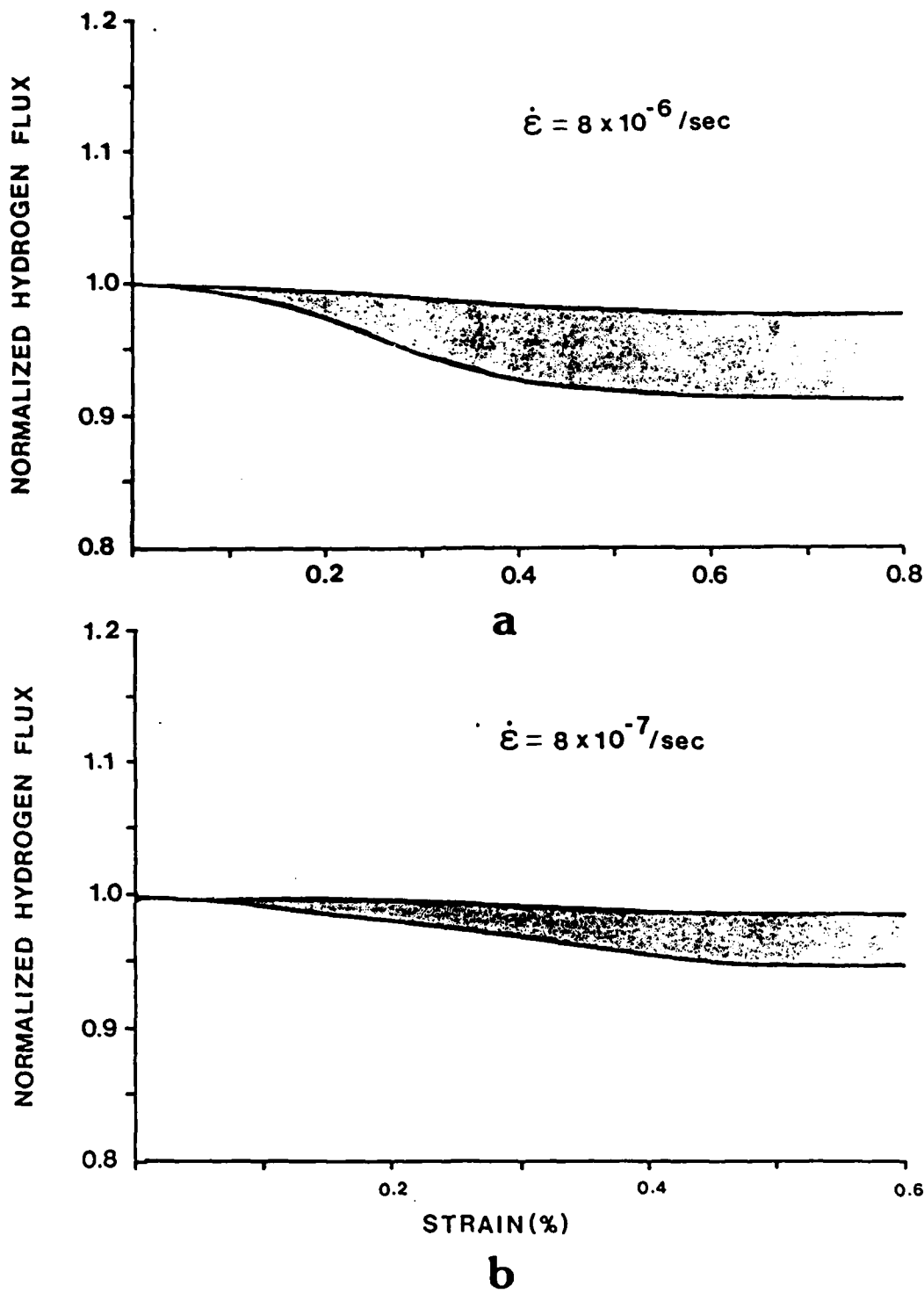


Figure 5-17: The hydrogen flux behavior showing the range of trapping effect during straining permeation tests at different strain rates. (a)  $\dot{\epsilon} = 8 \times 10^{-6} \text{ sec}^{-1}$ , (b)  $\dot{\epsilon} = 8 \times 10^{-7} \text{ sec}^{-1}$ , (c)  $\dot{\epsilon} = 8 \times 10^{-8} \text{ sec}^{-1}$ , (d)  $\dot{\epsilon} = 1.6 \times 10^{-8} \text{ sec}^{-1}$ .

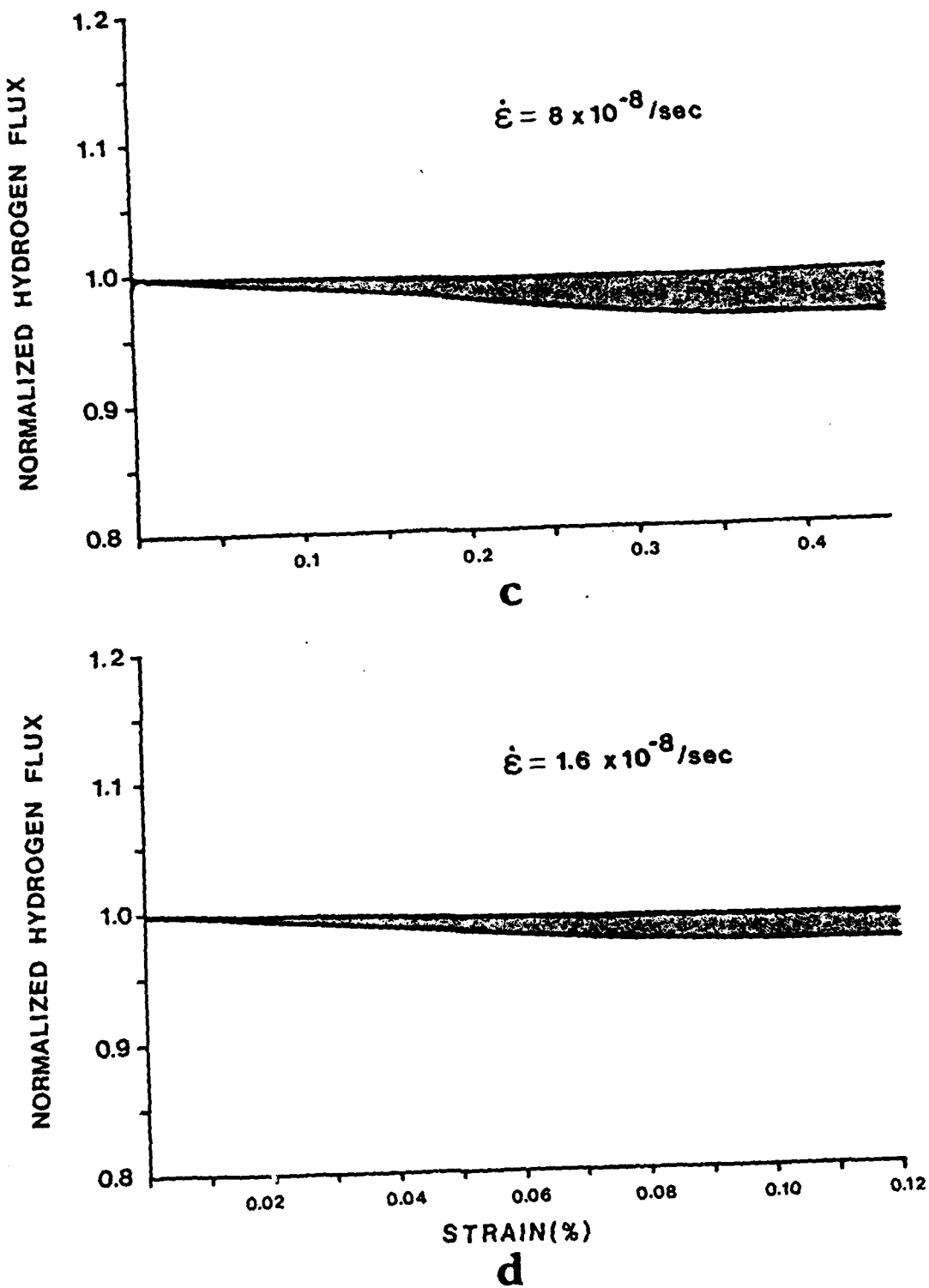


Figure 5-17: The hydrogen flux behavior showing the range of trapping effect during straining permeation tests at different strain rates. (a)  $\dot{\epsilon} = 8 \times 10^{-6} \text{ sec}^{-1}$ , (b)  $\dot{\epsilon} = 8 \times 10^{-7} \text{ sec}^{-1}$ , (c)  $\dot{\epsilon} = 8 \times 10^{-8} \text{ sec}^{-1}$ , (d)  $\dot{\epsilon} = 1.6 \times 10^{-8} \text{ sec}^{-1}$ .

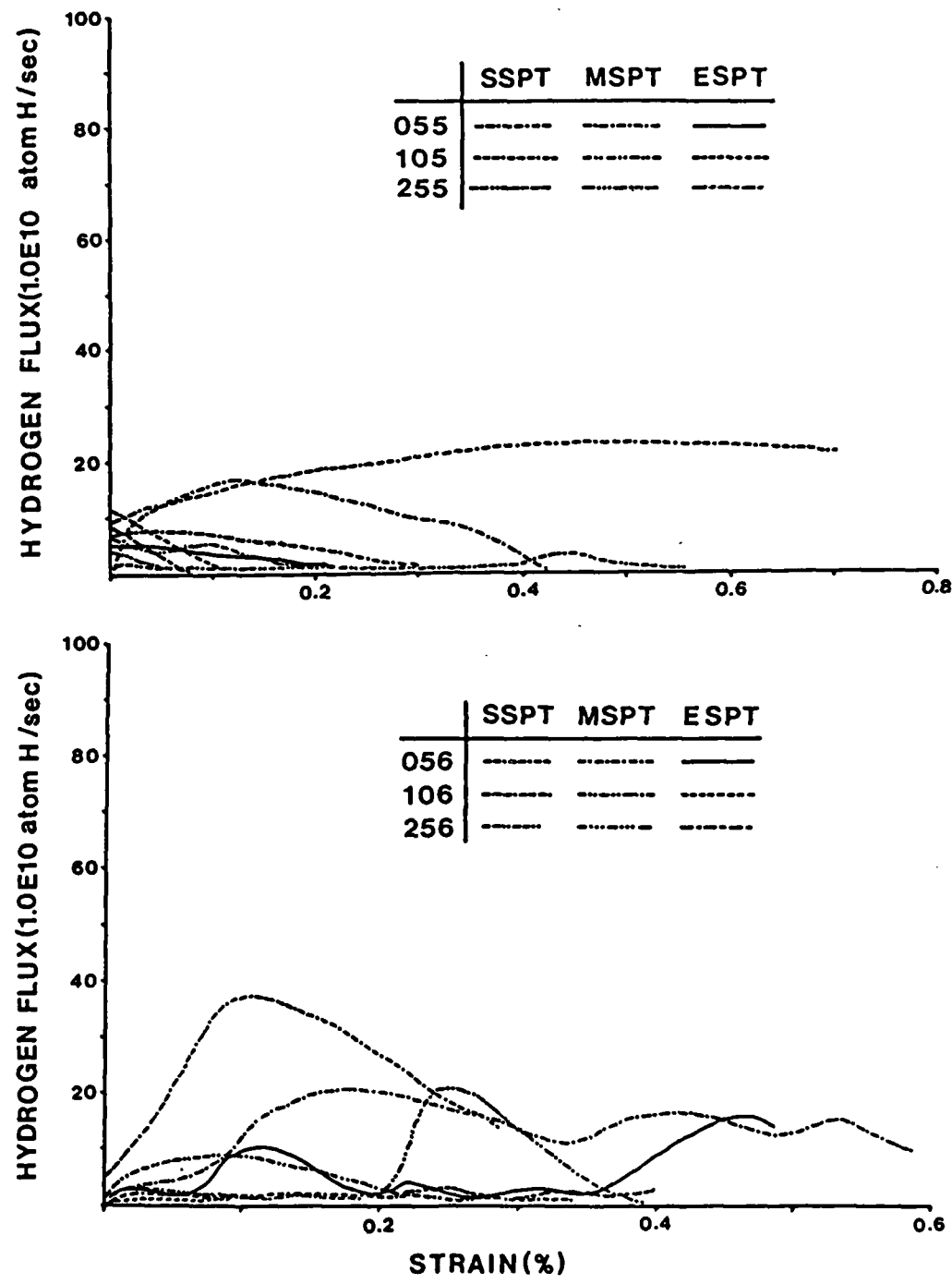
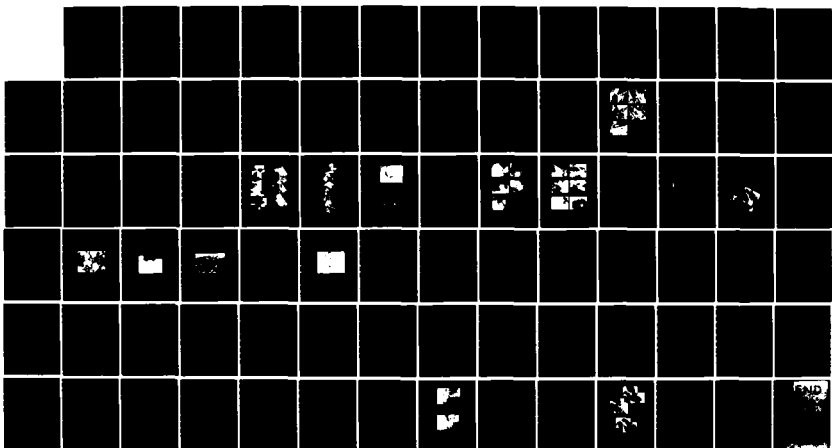
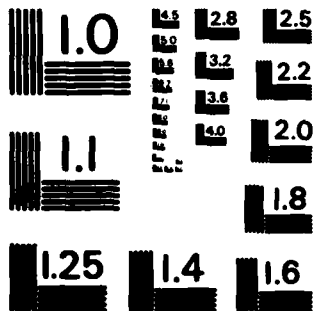


Figure 5-18: Hydrogen flux behavior showing the dislocation transport effect during straining permeation tests at different conditions indicated by the associated codes. Note:  $1.0\text{E}10 \text{ atom H/sec} = 1.0 \times 10^{10} \text{ atom H/sec}$ .

AD-A148 143 THE FUNDAMENTALS OF DISLOCATION TRANSPORT OF HYDROGEN 2/2  
IN BCC IRON(U) CARNEGIE MELLON UNIV PITTSBURGH PA DEPT  
OF METALLURGICAL ENGI.. C HWANG ET AL. OCT 84 TR-18  
UNCLASSIFIED N00014-75-C-0265 F/G 11/6 NL





MICROCOPY RESOLUTION TEST CHART  
NATIONAL BUREAU OF STANDARDS - 1963 - A

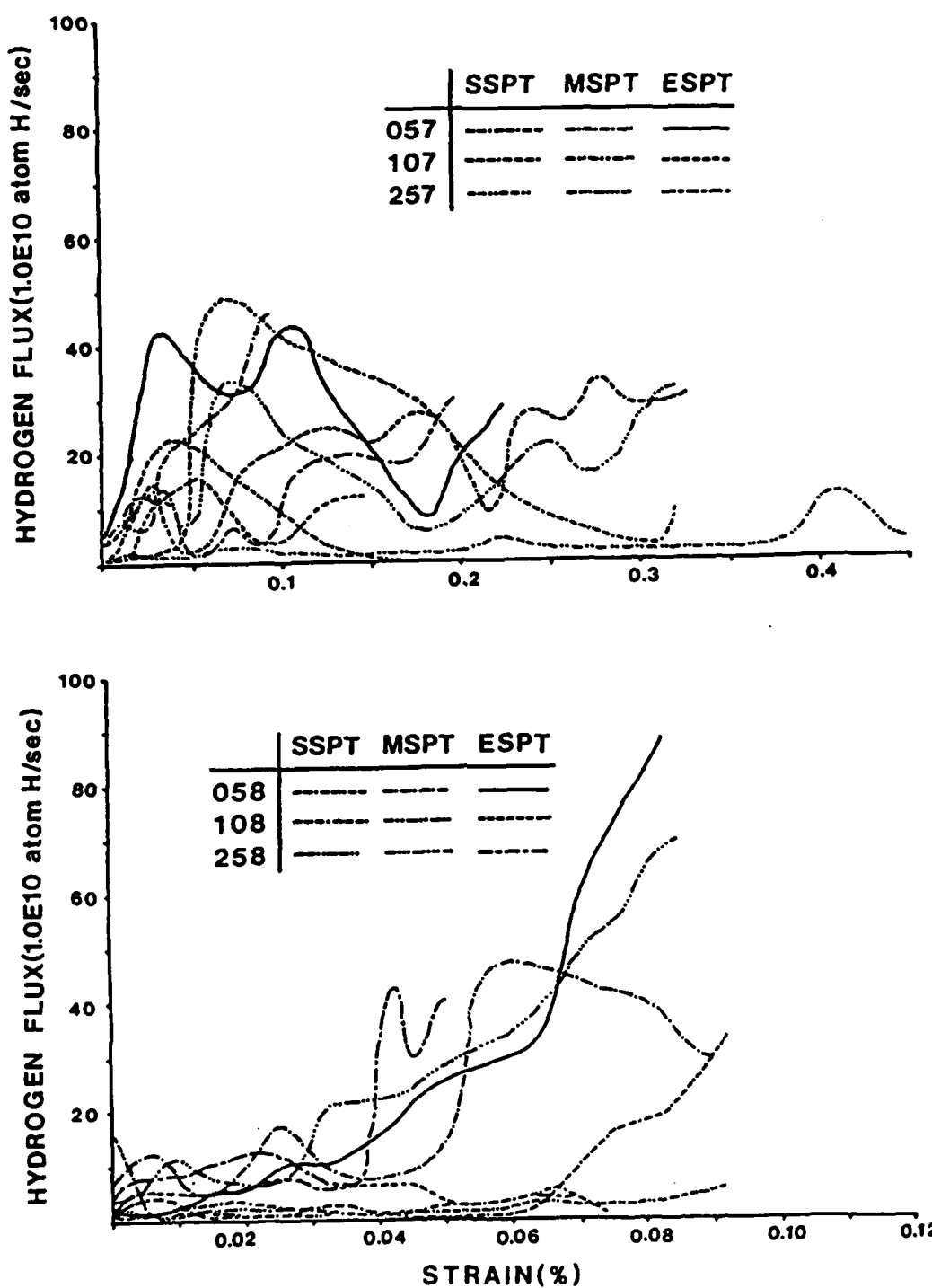


Figure 5-18: Hydrogen flux behavior showing the dislocation transport effect during straining permeation tests at different conditions indicated by the associated codes. Note:  $1.0E10$  atom H/sec =  $1.0 \times 10^{10}$  atom H/sec.

components were very different and rather complex for different test conditions, as can be seen in Figure 5-18. In addition to Figure 5-18, the transport data were further averaged by integrating the entire testing period, as shown in Figure 5-19. The significance of each of these approaches will be discussed in detail in the following sections.

Having established the data analysis technique where the hydrogen transport and trapping results have been separated, it is now possible to further investigate the dependence of the dislocation transport rate as a function of imposed experimental parameters. In the following sections, the effect of strain rate on hydrogen transport by different dislocations will be discussed first; the hydrogen concentration effect on these transport rates will then be presented; then, temperature effects will be discussed. Finally, a summary of all the effects mentioned will be presented, as will a more complete discussion of trapping effects which have been intentionally ignored till now.

#### 5.3.2.2. Effect of Strain Rate.

To compare the transport data at different strain rates, it should be recognized that if the mobile dislocation density can be assumed relatively constant throughout the entire strain rate range employed, the number of dislocation lines intersecting the crystal surface per unit time period will be directly proportional to the imposed strain rate, with the number of dislocation lines intersecting the anodic crystal surface increasing with the strain rate. In contrast to this, if the transport rate is averaged per unit strain, the total dislocation lines intersecting the crystal surface will be sensibly constant (because of the same strain), and the hydrogen transport rate can then be compared on the basis of a per unit dislocation line rather than a less significant time basis. However, as can be seen in Figure 5-19 even using the time average approach the transported hydrogen flux is always higher at slower strain rate, suggesting the validity of using the latter approach. If the transport rate is averaged based on per unit strain (in this case 0.01% strain is used), as shown in Figure 5-20, it is obvious that lower strain rates gave rise to a much higher transported hydrogen flux. Generally, the hydrogen transport rate increases an order of magnitude or more when the strain rate is lowered by an order of magnitude. This can be rationalized as follows: When straining

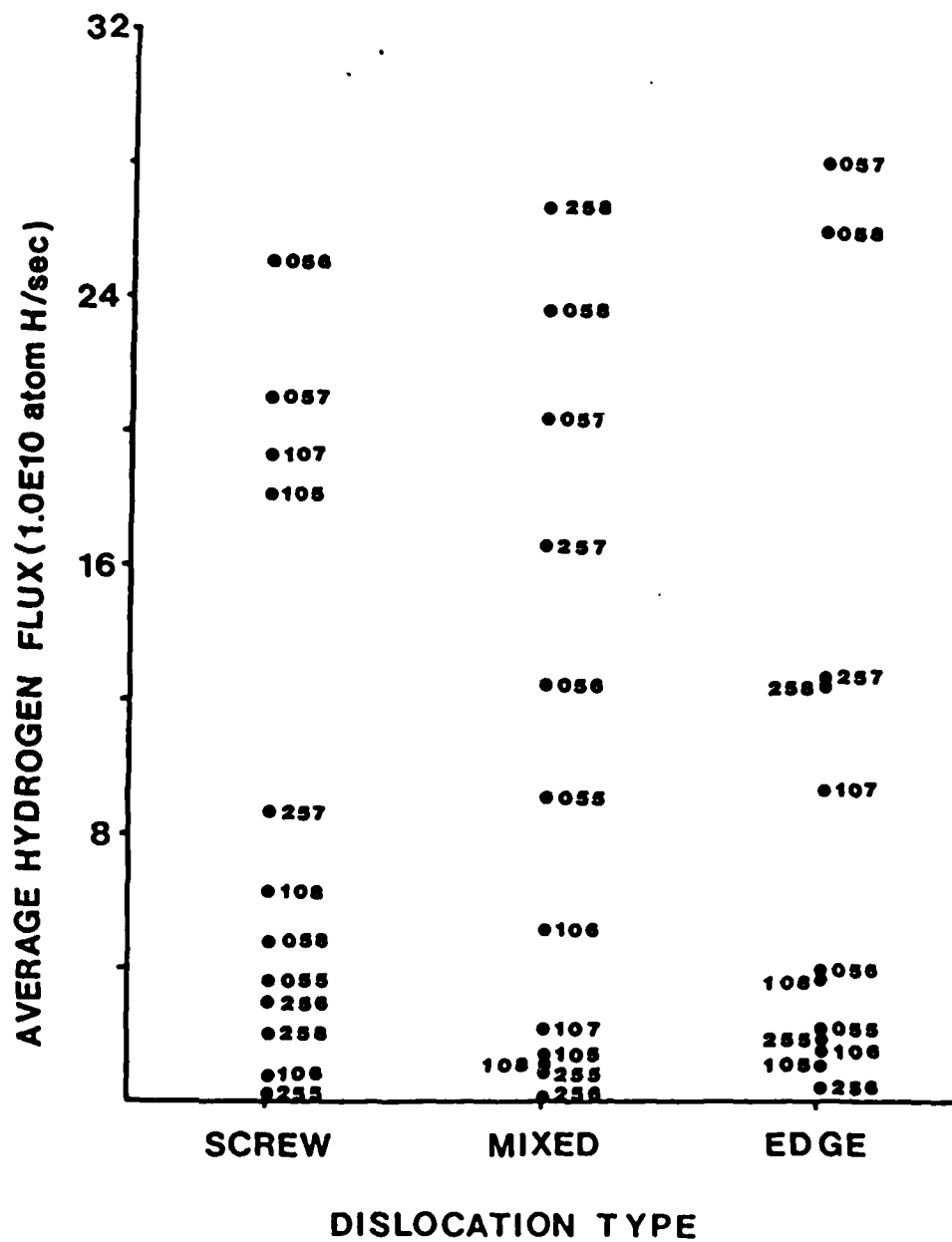


Figure 5-19: Average hydrogen transport rates based on per unit time for various tests indicated by special codes. Note:  $1.0E10$  atom H/sec =  $1.0 \times 10^{10}$  atom H/sec.

at a slower strain rate, for the assumption of a similar mobile dislocation density at different strain rates, it is believed that most dislocations will move more slowly, and hence are capable of carrying more hydrogen to the monitoring surface. Conversely, at higher strain rates, a certain percentage of the dislocations exceed the break-away velocity, for which the hydrogen can no longer keep up with the moving dislocations. This results in a smaller transport flux even though the number of dislocations intersecting the surface may be larger in a given time.

To compare the hydrogen transport rates for different dislocations, note that for the higher strain rate range, screws appear to transport more hydrogen than do edge or mixed dislocations. This is shown in Figure 5-21, by comparing tests: SSPT105, ESPT105 and MSPT105. Conversely, at lower strain rates edges and mixed types carry much more hydrogen than do screws; for example, compare tests SSPT258, ESPT258 and MSPT258. This phenomenon appears due to the combined effects of dislocation mobility and hydrogen concentration. Specifically, recall that for the screw orientation the actual hydrogen carrier is the mobile screw dislocation, whereas for the other two orientations the hydrogen carrier being monitored is the kinks which move at a much faster velocity than the total dislocation line.

To appreciate this difference, a simple comparison can be made by calculating the corresponding single step kink velocity necessary for a given dislocation line velocity. Since the width of the single crystal specimens used is 8 mm, a single step kink has to travel this distance to give rise to roughly one Burgers vector advance (the height of the kink) of its associated dislocation line lying parallel to the crystal surface; therefore the single step kink velocity can be calculated at different given dislocation line velocities as shown in Table 5-6. From it we can tentatively conclude that the kink velocity at the higher strain rate employed in this study may have exceeded the break-away velocity beyond which the hydrogen is no longer associated with dislocation, so that much less hydrogen can now be transported by dislocations. In support of this idea, Hashimoto(95) has calculated the hydrogen concentration remaining on a moving dislocation as a function of dislocation velocity and this is shown in Figure 5-22. Two binding energies used in his calculation resemble the binding energies for screw (0.2 eV) and edge (0.6 eV) dislocations respectively. He also defined that the break-away

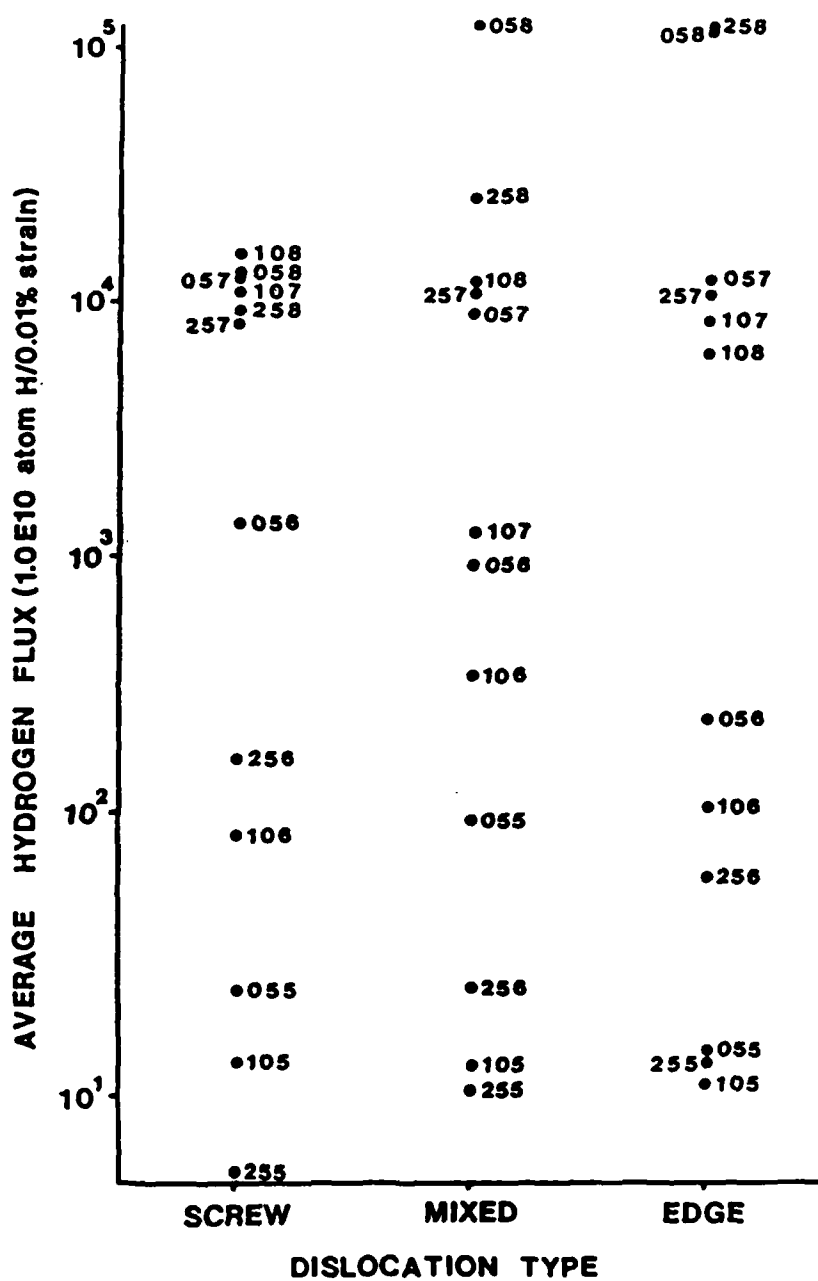


Figure 5-20: Average hydrogen transport rates based on per unit strain for various tests indicated by special codes. Note:  $1.0E10$  atom H/sec =  $1.0 \times 10^{10}$  atom H/sec.

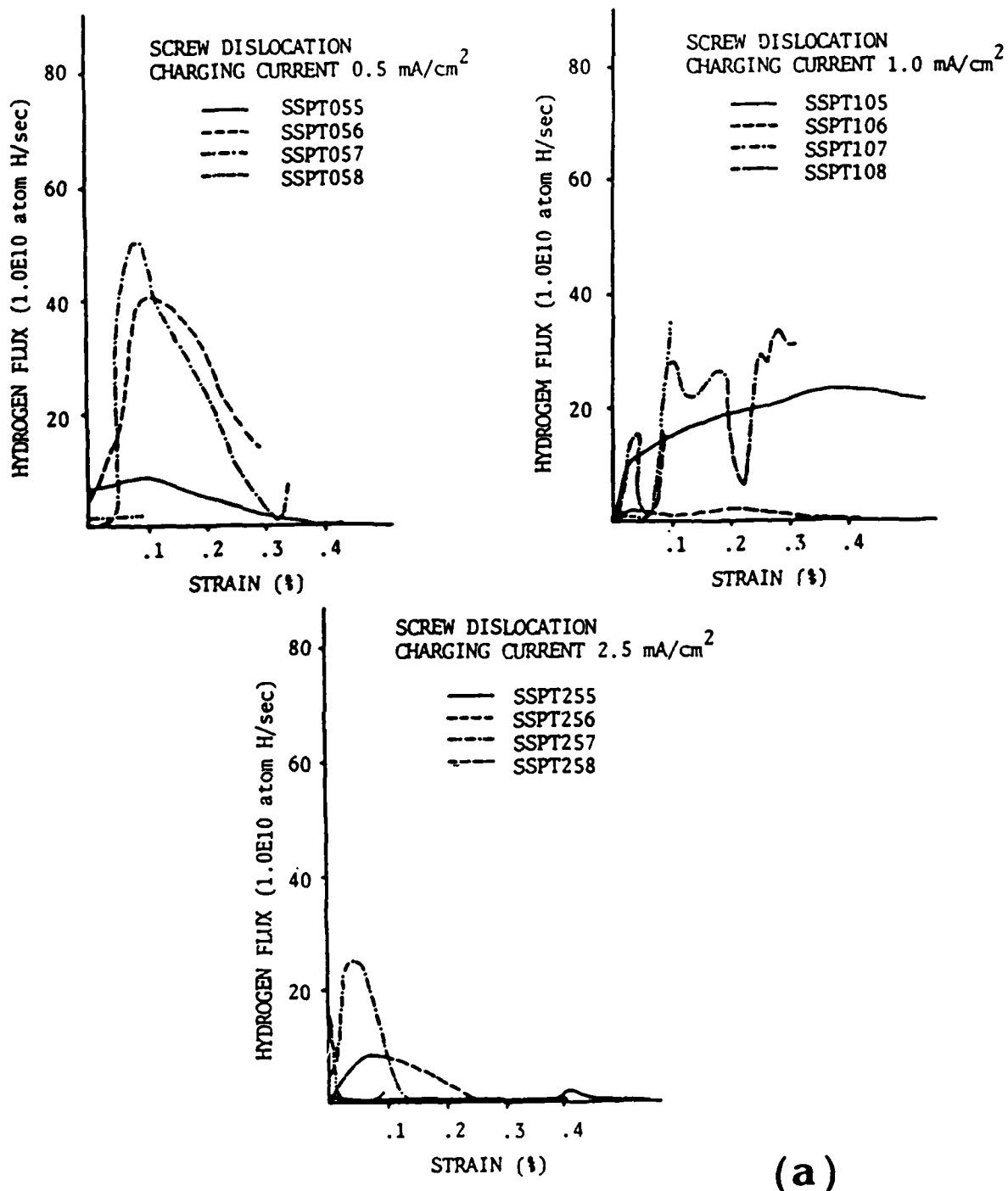


Figure 5-21: Strain rate effect on hydrogen transport rates by different dislocation types for different testing conditions. (a) screw dislocation, (b) mixed dislocation, (c) edge dislocation. Note:  $1.0E10$  atom H/sec =  $1.0 \times 10^{10}$  atom H/sec.

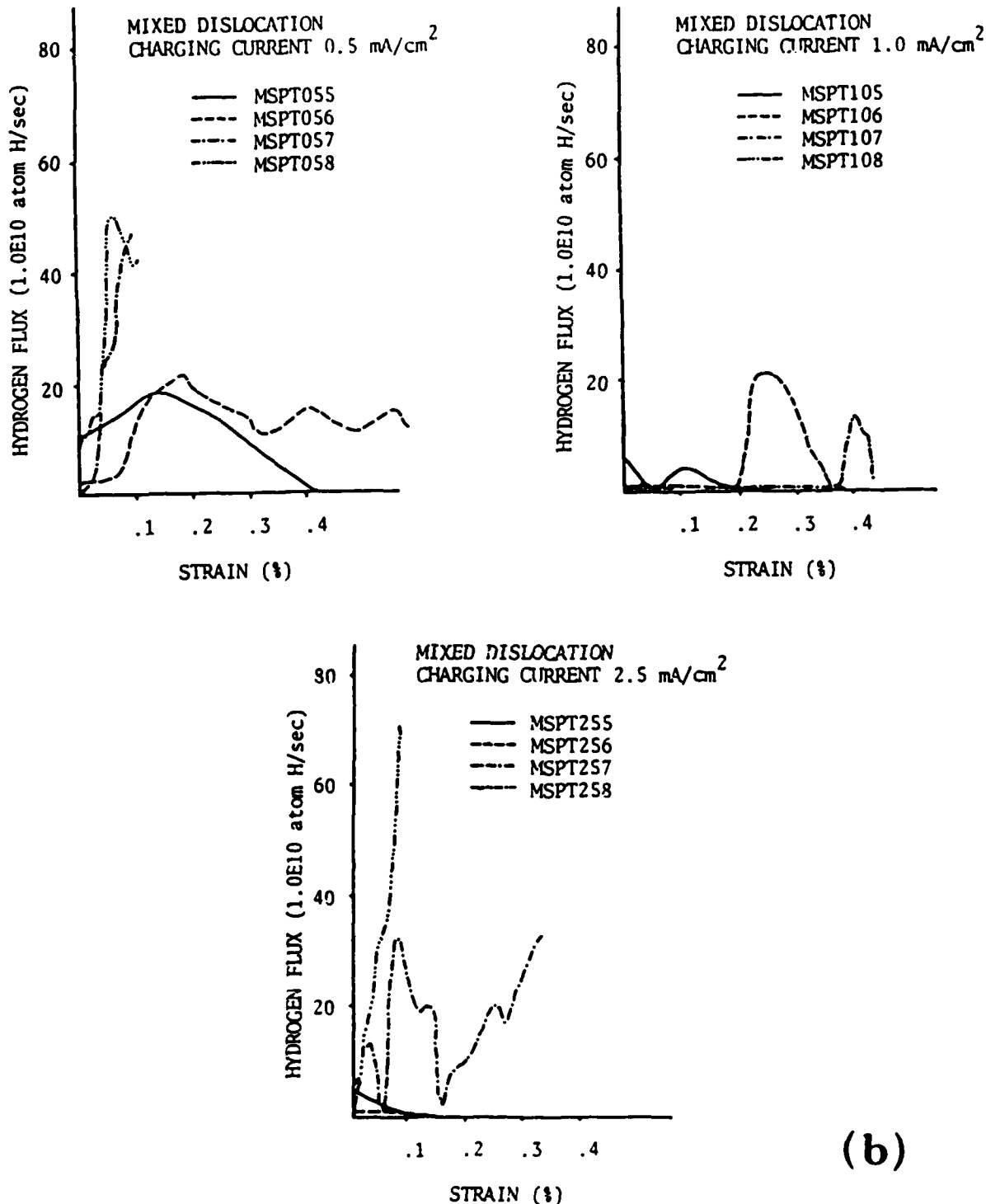


Figure 5-21: Strain rate effect on hydrogen transport rates by different dislocation types for different testing conditions. (a) screw dislocation, (b) mixed dislocation, (c) edge dislocation. Note:  $1.0E10$  atom H/sec =  $1.0 \times 10^{10}$  atom H/sec.

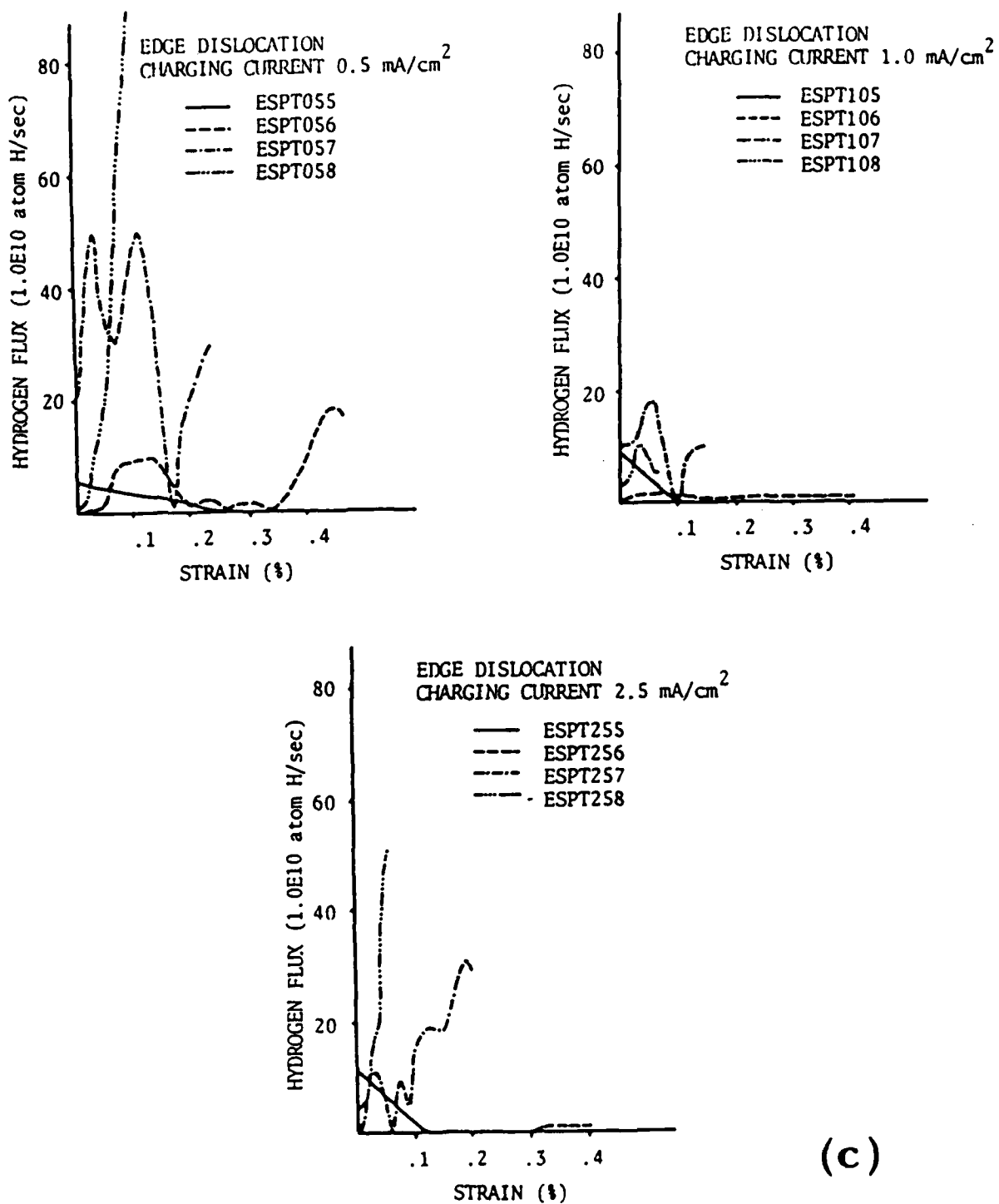


Figure 5-21: Strain rate effect on hydrogen transport rates by different dislocation types for different testing conditions. (a) screw dislocation, (b) mixed dislocation, (c) edge dislocation. Note:  $1.0E10$  atom H/sec =  $1.0 \times 10^{10}$  atom H/sec.

velocity is the velocity at which the core concentration is one tenth of that at stationary dislocation core, thus concluded that the break-away velocity is about 3.6 cm/sec for edge dislocations and 3600 cm/sec for screw dislocations. Tien et al(81) also reported a estimated dislocation break-away velocity for iron alloys, which is about 10 cm/sec. These dislocation velocities are orders of magnitude higher than those expected in our slow strain rate tests (Table 5-6). Thus only the kinks travelling along screw dislocation lines may reach a velocity of the same order of magnitude as the break-away velocity for edge dislocation; otherwise dislocations are capable of dragging the associated hydrogen atmosphere successfully through a hydrogen depleted matrix, compared to the concentration at defects.

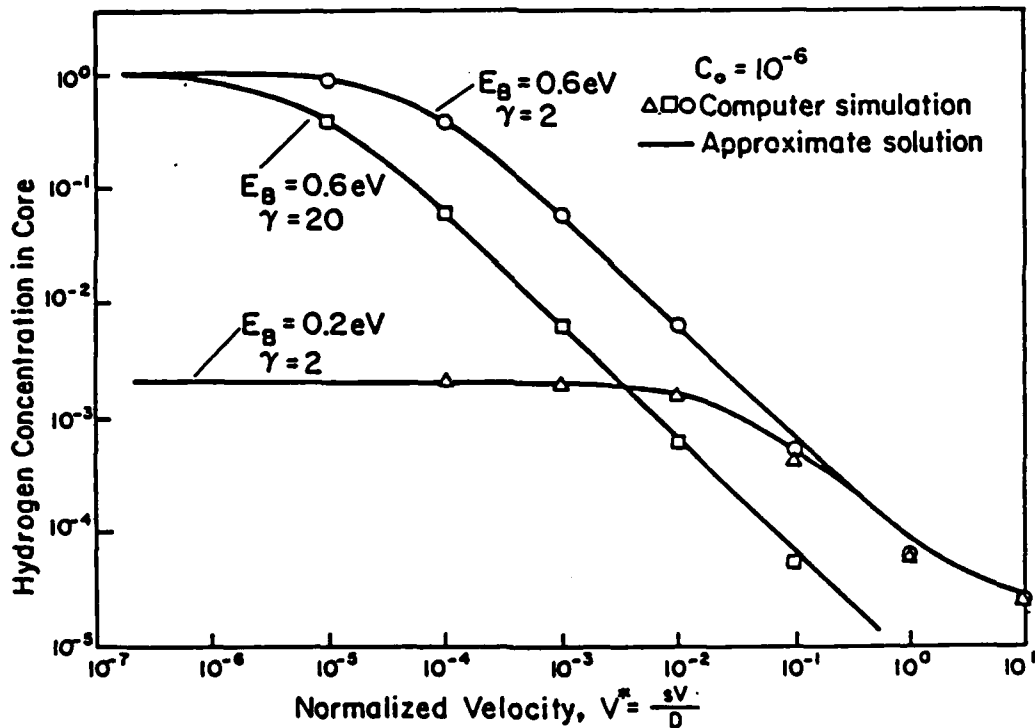


Figure 5-22: Hydrogen concentration in the dislocation core at steady state as a function of velocity.(95)

In the edge and mixed orientation specimens we have tested, the actual hydrogen-carriers monitored are edge (mixed) kinks travelling along the screw dislocation line present in the specimens. These kinks move much faster than

Table 5-6: A comparison of dislocation velocity and kink velocity at different strain rates assuming a constant mobile dislocation density of  $10^6 \text{ cm/cm}^3$ .

| STRAIN RATE<br>(sec <sup>-1</sup> ) | DISLOCATION VELOCITY<br>(cm/sec) | KINK VELOCITY<br>(cm/sec) |
|-------------------------------------|----------------------------------|---------------------------|
| $10^{-5}$                           | $10^{-3}$                        | $10^3$                    |
| $10^{-6}$                           | $10^{-4}$                        | $10^2$                    |
| $10^{-7}$                           | $10^{-5}$                        | $10^1$                    |
| $10^{-8}$                           | $10^{-6}$                        | $10^0$                    |

the actual screw dislocation velocity, as shown in Table 5-6. In some cases, the kink velocities may reach the break-away velocity for the higher strain rates employed, hence the hydrogen transport rates are very small as shown in Figure 5-21. When the kink velocity substantially slows down at the slower imposed strain rates, the hydrogen transported by them can then become quite high. In the screw oriented case, this strain rate effect on hydrogen transport rate is less significant, which can be attributed to the fact that the hydrogen-carrier in this case is the screw dislocation itself which presumably moves at a much slower speed. Hence for the majority of dislocations, the break-away velocity can not be reached even at the highest strain rate used in this study.

In addition, at the lowest strain rates ( $1.6 \times 10^{-8} \text{ sec}^{-1}$ ), we find almost no hydrogen being carried by screw dislocations. If we examine the dislocation dynamics more carefully we find that at the lowest strain rate the dislocation velocity is extremely slow (see Table 5-6), and thus an excessive time would be needed to observe a significant hydrogen flux. In fact, the time at which the first significant hydrogen flux was detected in each test can be summarized in Table 5-7. These times clearly scale with the strain rate, consistent with our speculation that for screws, an insufficient test time prevented enough dislocations from travelling through the entire specimen thickness. In contrast, for the edge and mixed orientation specimens, the hydrogen carriers are kinks which move considerably faster than the average dislocation velocity. Thus for the same test time kinks can move through the entire specimen thickness and contribute to the detected total hydrogen transport flux. Additionally, for a kink velocity slow enough to retain its hydrogen atmosphere, the transport rate can be very high as in the case of

**Table 5-7: Approximate break-through time for significant dislocation transport of hydrogen flux.**

| TEST | SSPT<br>(sec) | MSPT<br>(sec) | ESPT<br>(sec) |
|------|---------------|---------------|---------------|
| 055  | >700          | >700          | >700          |
| 056  | ~400          | ~1000         | ~3000         |
| 057  | ~5000         | ~1000         | ~2000         |
| 058  | ~40000        | ~25000        | ~20000        |
| 105  | <50           | >700          | >700          |
| 106  | >500          | ~3000         | >4000         |
| 107  | ~2000         | ~50000        | ~1000         |
| 108  | ~40000        | >30000        | >40000        |
| 255  | >500          | >400          | >700          |
| 256  | <1000         | >6000         | >4000         |
| 257  | ~2000         | ~15000        | ~8000         |
| 258  | >50000        | ~25000        | ~20000        |

slower strain rate tests for edge and mixed dislocations, which possess a higher binding energy for hydrogen, as shown in Table 2-2. Although for our test conditions we did not observe a steady state dislocation transport rate, we speculate that if the single slip system persisted through the test one should exist, which could then be used to more accurately evaluate the carrying capacity for different dislocation types.

The results obtained indicate that edge dislocations have the highest hydrogen transport rate at the slowest strain rate, implying that a higher hydrogen concentration is associated with edge dislocations, consistent with the fact that edges have a higher binding energy with hydrogen. Thus the fact that at the slowest strain rate there is almost no hydrogen being carried by screw dislocations and this situation is exactly reversed for the edge and mixed orientations has thus been rationalized by the combined effects of the dislocation mobility and associated hydrogen concentration for different types.

### 5.3.2.3. Effect of Hydrogen Concentration

**Table 5-8:** Steady state lattice hydrogen diffusion fluxes and strains before each straining permeation test.

| TEST | SSPT                                  |               | MSPT                                  |               | ESPT                                  |               |
|------|---------------------------------------|---------------|---------------------------------------|---------------|---------------------------------------|---------------|
|      | FLUX<br>( $\mu\text{A}/\text{cm}^2$ ) | STRAIN<br>(%) | FLUX<br>( $\mu\text{A}/\text{cm}^2$ ) | STRAIN<br>(%) | FLUX<br>( $\mu\text{A}/\text{cm}^2$ ) | STRAIN<br>(%) |
| 055  | 4.58                                  | 0.0           | 6.69                                  | 0.0           | 5.75                                  | 0.0           |
| 056  | 4.89                                  | 0.585         | 8.24                                  | 0.515         | 5.84                                  | 0.581         |
| 057  | 5.27                                  | 0.903         | 9.16                                  | 1.118         | 5.65                                  | 1.065         |
| 058* | 5.97                                  | 3.913         | 6.19                                  | 4.027         | 8.34                                  | 3.769         |
| 105  | 8.40                                  | 1.227         | 9.63                                  | 1.292         | 6.60                                  | 1.293         |
| 106  | 8.52                                  | 1.958         | 9.63                                  | 1.794         | 6.28                                  | 1.958         |
| 107  | 8.68                                  | 2.415         | 9.57                                  | 2.292         | 6.16                                  | 2.401         |
| 108* | 16.29                                 | 3.991         | 11.84                                 | 4.117         | 13.13                                 | 3.835         |
| 255  | 12.28                                 | 2.715         | 11.08                                 | 2.732         | 16.80                                 | 2.557         |
| 256  | 12.98                                 | 3.289         | 10.64                                 | 3.191         | 12.53                                 | 3.138         |
| 257  | 12.88                                 | 3.717         | 11.11                                 | 3.618         | 12.13                                 | 3.566         |
| 258* | 18.79                                 | 4.086         | 13.07                                 | 4.220         | 21.88                                 | 3.916         |

\* The slowest straining permeation tests are conducted at a higher total strain, as noted in the strain column.

Table 5-8 summarizes the steady state lattice diffusion hydrogen flux obtained for each test condition. It is clear that at a higher charging current density and hence higher lattice hydrogen concentrations a somewhat higher steady state flux was obtained. However, the transport rate data show an insignificant dependence of charging current density compared for example to the strain rate dependence, as shown in Figure 5-23, suggesting that the lattice concentration may not have a significant effect on the hydrogen concentration associated with dislocations. This will be the case if the dislocation core for the total mobile density is saturated with hydrogen even at the lowest charging current density ( $0.5 \text{ mA/cm}^2$ ) employed.

In some cases, such as tests ESPT058 and ESPT258; at lower input concentration the hydrogen transport rate by dislocations is actually higher, implying firstly, that the lattice hydrogen has no obvious effect on the hydrogen concentration associated with dislocations, and secondly, and likely more importantly, the microstructure (total strain) where these two tests were conducted has a stronger effect on the transport rate. The ESPT258 test was performed at a higher total strain than was ESPT058 (see Table 5-8), hence the former has a higher sessile dislocation density, likely giving rise to the observed difference in transport rate due to the stronger trapping effect.

This weak dependence of the amount of hydrogen associated with dislocations on lattice hydrogen concentration may also indicate that the local equilibrium between hydrogen concentration on dislocations and in the lattice is not fulfilled, supporting the kinetic nature of dislocation transport. That is, once hydrogen is trapped in the dislocation core it will be dragged along with the dislocations until the dislocations encounter an even stronger trap, annihilate with other dislocations, or intersect the crystal surface, and hydrogen can then be released. However it will not significantly interact reversibly with the lattice.

#### 5.3.2.4. Effect of Temperature

A series of experiments has been conducted in order to study the effect of temperature on the transport mechanism. As discussed, inherent limitations of this type of tests are the temperature stability of solution and instruments, especially the standard calomel electrode which can be used only within 0 °C to 80 °C. Our constant temperature bath can keep the temperature variation virtually undetectable by a conventional mercury thermometer, but since even a few tenths of degree fluctuation in temperature is enough to give rise to a background noise in size comparable to the hydrogen flux transported by dislocations, interpretation problems are potentially serious. This problem was found to be most severe only at the higher temperature, possibly related to a greater though unidentified instability in the solution chemistry or associated electronic devices.

To obtain more reliable results, we have chosen to run several identical tests at a rather fast strain rate ( $1 \times 10^{-5}$  sec $^{-1}$ ) to keep the test time period short and to then average the data obtained. Table 5-9 shows such results for

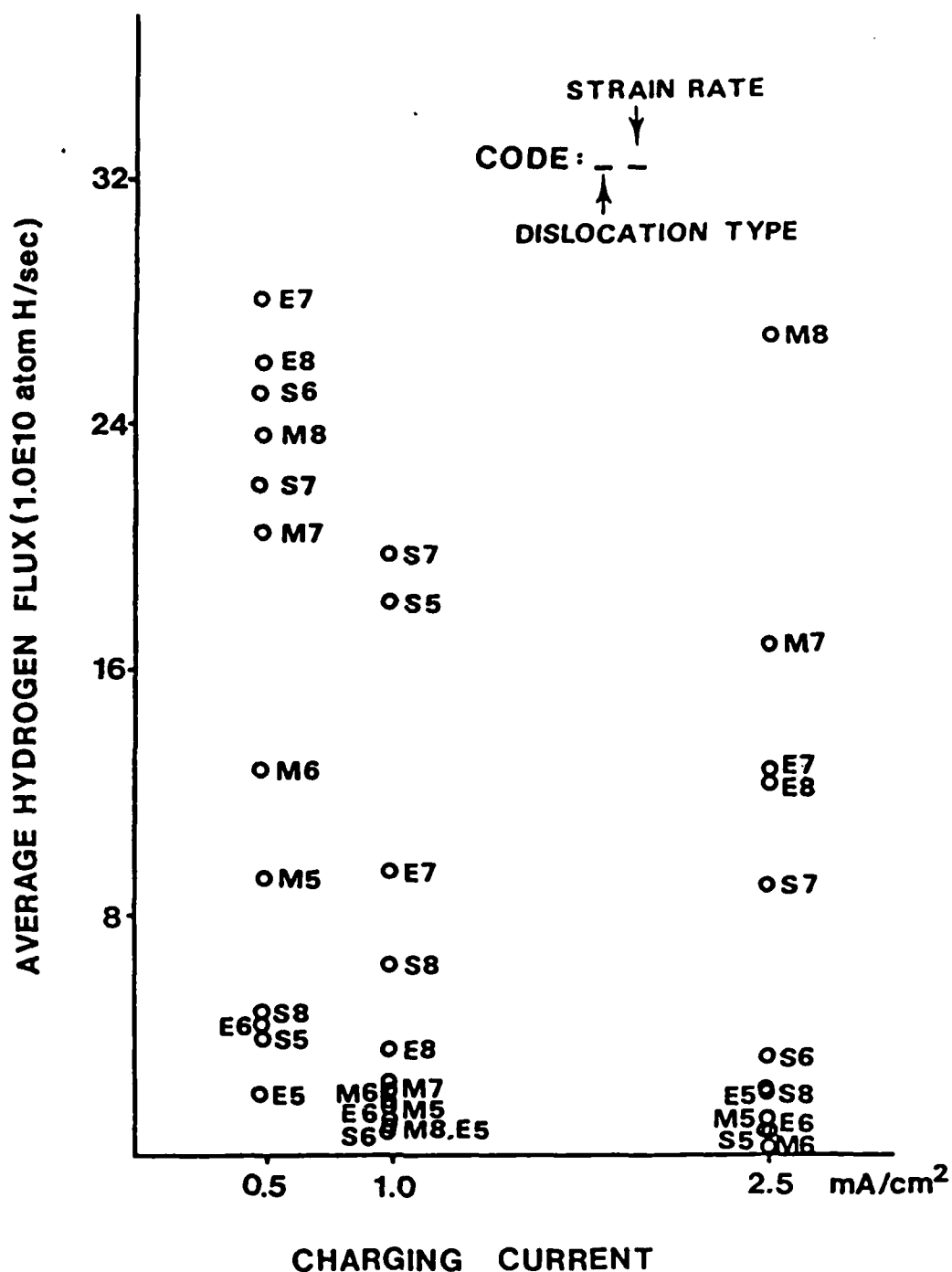


Figure 5-23: The lattice hydrogen concentration effect on hydrogen transport rates by different dislocations. Note: 1.0E10 atom H/sec =  $1.0 \times 10^{10}$  atom H/sec.

**Table 5-9:** Temperature dependence of hydrogen transport rate by screw and edge dislocations. The strain rate used is  $1 \times 10^{-5} \text{ sec}^{-1}$  and the charging current density is  $0.5 \text{ mA/cm}^2$ .

| <u>TEMPERATURE(<math>^{\circ}\text{C}</math>)</u> | <u>SCREW(<math>10^{10} \text{ ATOM H/SEC}</math>)</u> | <u>EDGE(<math>10^{10} \text{ ATOM H/SEC}</math>)</u> |
|---|---|--|
| 12  | $5.35 \pm 0.71$                                       | $8.03 \pm 0.25$                                      |
| 24  | $5.85 \pm 0.25$                                       | $4.45 \pm 0.1$                                       |
| 45  | $6.37 \pm 0.78$                                       | $7.78 \pm 2.41$                                      |
| 78  | $5.75 \pm 0.78$                                       | $16.79 \pm 1.86$                                     |

screw and edge orientations at four different temperatures. It is not surprising to see that the transport rates are almost the same for these four temperatures since the extra thermal energy provided by raising the temperature is about  $k\Delta T$ , where  $k$  is Boltzmann's constant and  $\Delta T$  is the temperature difference between two test temperatures, which is a maximum of about 0.03 eV. Since this is only a small fraction of the binding energy (0.2-0.6 eV) between hydrogen and dislocations, it is therefore impractical to expect a significant variation in the hydrogen transport rate. However, it is noteworthy that the steady state hydrogen flux is increased substantially with increasing temperature due to the increased permeability of hydrogen through the specimen at higher temperature. Again, these results indicate that there is no obvious thermodynamic equilibrium between the hydrogen trapped at dislocations and in the lattice during the straining permeation test, again consistent with the kinetic nature of this transport phenomenon.

#### 5.3.2.5. Summary

This detailed study has separately determined the hydrogen transport rates by different dislocation types. It has been clearly shown that hydrogen transport rate by dislocations is strongly dependent on the dislocation types and strain rates. Edge kinks seem to have the greatest capability to transport hydrogen provided that their velocity is slow enough to allow them to retain their associated hydrogen atmosphere. This is understandable since edge dislocations have the highest binding energy with hydrogen, and are thus capable of trapping a larger amount of hydrogen (Table 2-2). Due to experimental limitations, it was not possible to measure the hydrogen transport

rate by long lengths of edge dislocation lines, but rather the "edge kinks" travelling along the screw dislocations were monitored. The same general conclusion can also be applied to the mixed type dislocation as well. Further, the hydrogen transport rate increases with decreasing strain rate for every type of dislocation if a constant mobile dislocation density at different strain rate is assumed(188). To obtain the exact transport rate, the exact mobile dislocation density at each given experimental condition would be needed, but this is yet to be obtained. In any event such a calculation is at present unwarranted considering the other various assumptions used in this analysis.

The weak lattice hydrogen concentration effect on the hydrogen transport rate by dislocations was attributed to the kinetic nature of this transport mechanism, where the thermodynamic equilibrium between the hydrogen at mobile dislocations and in the lattice is not readily obtainable. Further, the insignificant temperature effect on dislocation transport of hydrogen is also consistent with the above, since the lattice hydrogen concentration increases substantially with temperature; however a minimal effect on hydrogen transport with increasing temperature was observed.

#### 5.3.2.6. Trapping Effect

Another issue which has been ignored in the previous discussion is the details of the associated trapping. As shown in Figure 5-17, the trapping effect due to newly generated sessile dislocations during straining was relatively small for all the tests conducted in this portion of study. This is due to the fact that the plastic deformation for the single crystals under study was restricted to one primary slip system, so that the dislocation multiplication rate was minimized. In general, this condition is not readily obtainable in polycrystal specimens and consequently the trapping effect then would be much more dominant(95), which in turn could mask the extent of enhanced transport. To further elucidate this point, an identical straining permeation test was conducted on a single crystal oriented for double slip. The orientation of this crystal is shown in Figure 5-24, where two slip systems are found to have the identical Schmid's factors. The trapping effect for this particular orientation is presented in Figure 5-25 and compared with that for the three single slip systems also examined. It is obvious that the trapping effect for the latter cases were all about the same, whereas the double slip system

exhibited a much greater trapping effect, resembling that for polycrystal iron specimen(95). This is clearly due to the interaction between two equally activated slip system which results in a much higher dislocation multiplication rate and in turn enhanced trapping.

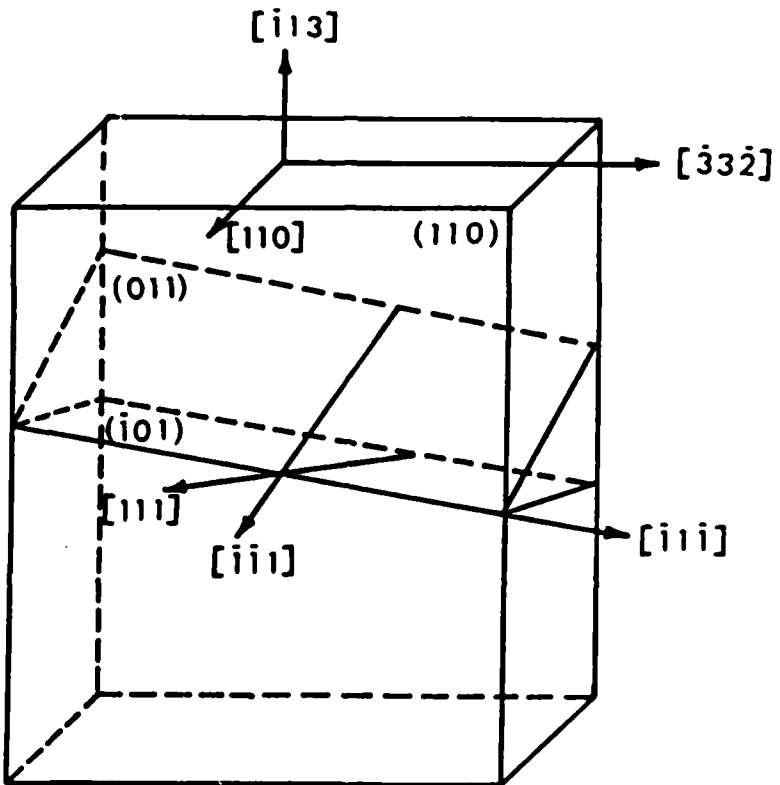


**Figure 5-24:** A double slip crystal orientation used to study the trapping effect.

It is clear that while the trapping effect should not be overlooked in general, in this study, its importance has been intentionally minimized so as to more clearly monitor the hydrogen transport nature of dislocations. The relative importance of trapping and transport during plastic deformation were studied as described in the following section, by using polycrystal iron specimens.

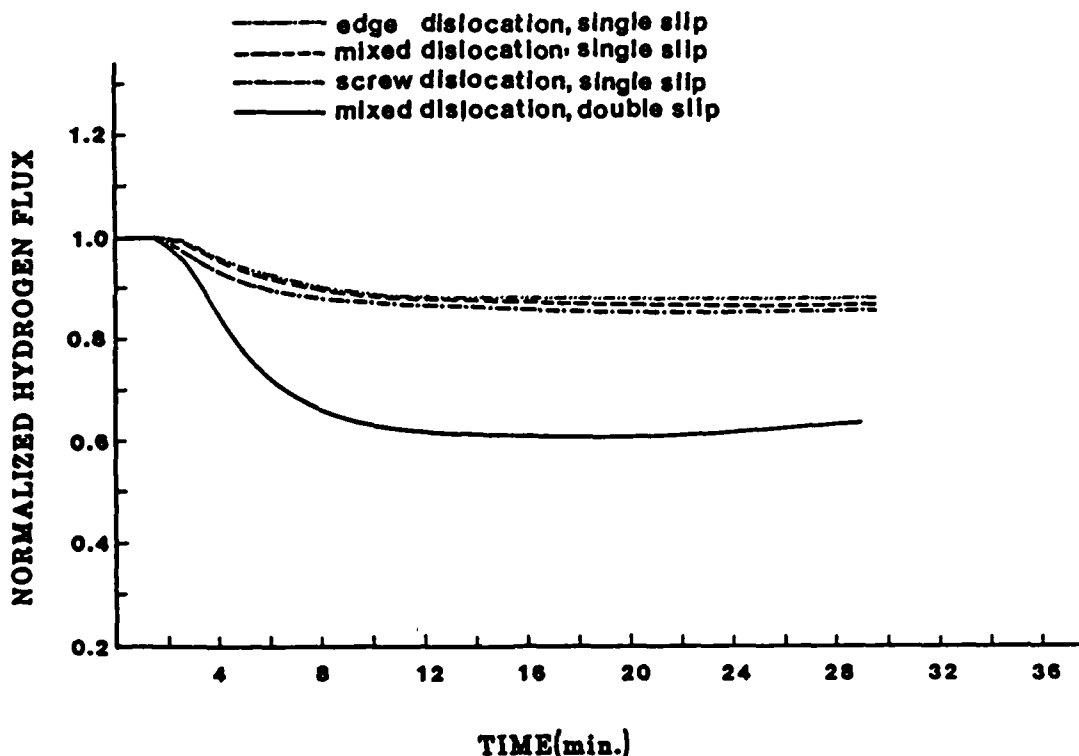


Figure 5-25: The trapping effect due to strain induced sessile dislocations for single crystals oriented for single and multiple slips.

#### 5.4. Straining Permeation Tests for Polycrystalline Specimens

##### 5.4.1. Hydrogen Flux Behavior during Straining

Straining permeation tests similar to those done on single crystals were also conducted on polycrystal pure iron, but at higher strain rates ranging from  $6.9 \times 10^{-5} \text{ sec}^{-1}$  to  $1.5 \times 10^{-5} \text{ sec}^{-1}$ . A characteristic permeation transient is shown in Figure 5-26 together with its associated stress - strain curve. In the small strain range, the flux behavior is similar to that of single crystals. However, the decrease in flux upon yielding is more pronounced due to the faster dislocation multiplication rates and the higher strain rates employed. Continued straining does in time produce an increasing flux whose magnitude

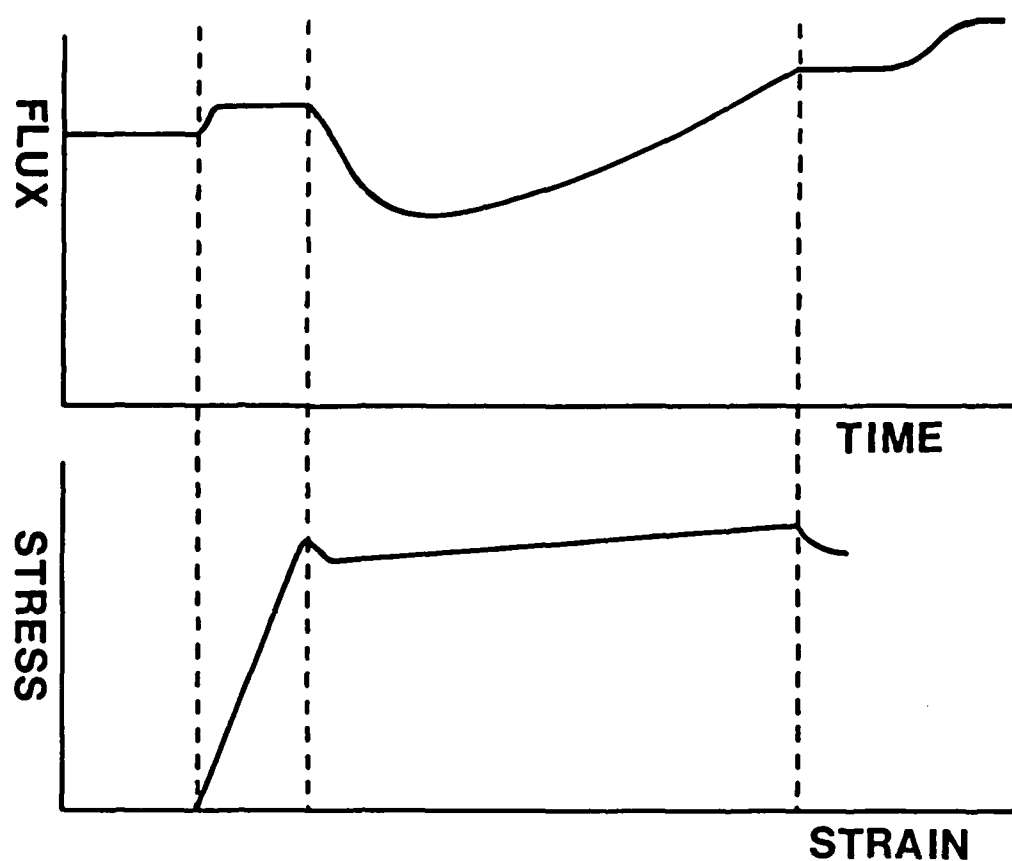
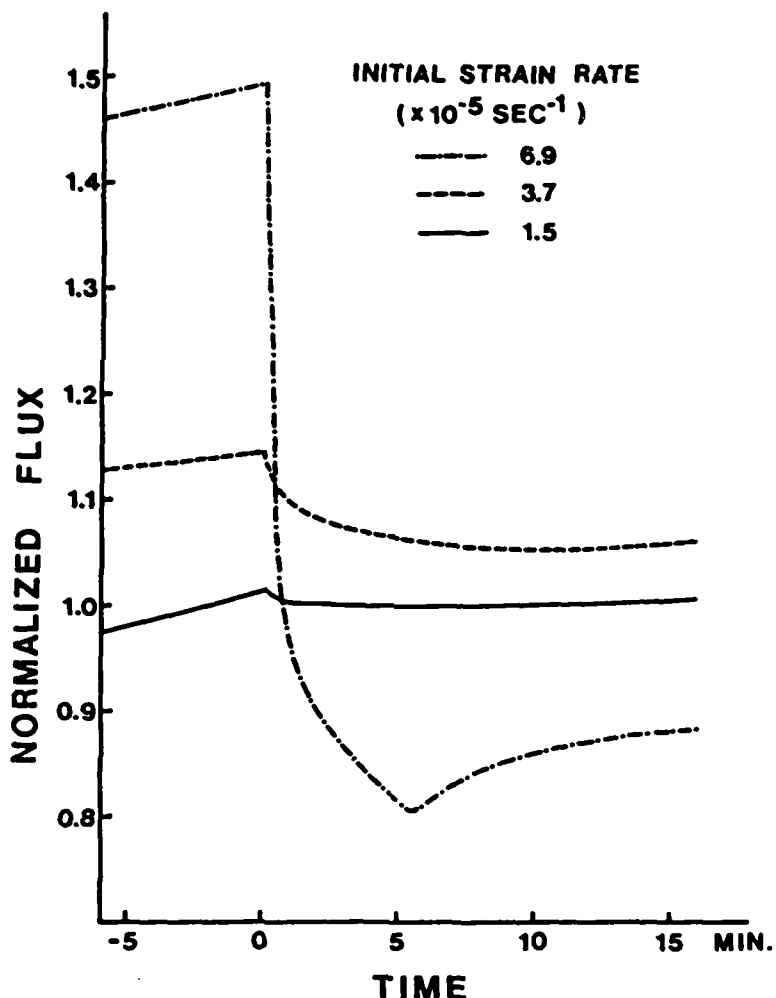


Figure 5-26: Changes in the steady state permeation flux of hydrogen from the unstrained state due to concurrent plastic deformation.

can in fact exceed the value of the original strain-free steady state flux. If the strain rate is now reduced to zero with the input current density retained, the flux either remains relatively constant for the lowest strain rate ( $1.5 \times 10^{-5}$  sec $^{-1}$ ) or decreases sharply at the higher strain rates, as illustrated in Figure 5-27. At longer times, the flux again rises, and the final steady state flux is always somewhat higher than the original steady state value.

Due to the higher strain rates involved in these tests, the final total strain on the specimens was much greater than for the single crystals. However, the extent was carefully monitored and controlled to avoid any



**Figure 5-27:** Strain rate dependence of normalized flux with respect to the steady state flux prior to straining. The time shown is the period after the cessation of straining.

complications due to abnormal surface effects. It is believed that at these higher strains the consequent increase of flux after the first decay results from the saturation of the dislocation density and hence the number of trapping sites. Support for this argument can be found in the work of Keh and Weissman(181) on dislocation structures in polycrystalline iron deformed at room temperature. At small strains the dislocation density was shown to increase linearly with strain, tending to saturate above about 10%. They also found that a dislocation cell structure begins to develop after about 3.5% strain and is well formed after about 8% strain. Increasing strain sharpens the

cell walls, likely due to local annihilation and rearrangement, but the cell diameter remains quite constant at about  $1.5 \mu\text{m}$ . This microstructure response due to straining has also been studied in the current work, as presented in the next section, and it is consistent with the above findings. The reason trapping is dominant in the early strain region is that as the dislocation density rises rapidly dislocation intersections and "knitting" reactions(193) reduce the local slip length and produce strong trapping centers. In the single crystal case with only one slip system operating, this is less likely, and hence a weaker trapping effect was found, as previously described. As more hydrogen is introduced at larger total strains, both the weak (e.g. single dislocation lines) and strong (e.g. dislocation cell wall) traps become effectively filled, particularly since the rate of dislocation production is now decreasing(181). Enhanced transport of hydrogen by mobile dislocations which are moving through the cells should now begin to dominate. For this process to produce the observed measurable increases in flux requires that hydrogen be easily released at cell wall and grain boundaries, move across these barriers, and then be available to be "picked up" by other dislocations generated to ensure slip continuity. The likelihood that such a sequence can occur has been demonstrated by Tien et al(81), and was discussed in Section 2.1. The different behavior observed as a function of strain rate, particularly when the rate is reduced to zero is also consistent with the above discussion. The higher strain rates require that a greater population of mobile dislocations carry hydrogen since there is a ready hydrogen supply available at the input surface. The permeation rate would then initially drop more sharply at higher strain rates when this rate is decreased to zero, since the primary vehicle for enhanced transport has been eliminated, as clearly shown in Figure 5-27. The final gradual increase in flux has been rationalized in Section 5.3.1, for the single crystal case; it should be equally applicable to the polycrystalline specimens.

Unlike the case of screw dislocations, no "peaking phenomenon" has been found in polycrystalline specimens, this is likely due to the more uniform intersection of dislocations on specimen surface, since the strain is distributed through many grains with many different operating slip systems, rather than along a single slip system.

To further study the significance of the relative contribution of trapping

and dislocation transport to the overall hydrogen diffusion rate during plastic deformation of polycrystalline specimens, additional tests measuring the apparent diffusivities with and without straining were conducted. It is expected that since during straining the microstructure changes from a well annealed structure to a dense dislocation tangled structure and finally to a well defined cell structure (Figure 5-28), the hydrogen diffusion rate through these different structures should be significantly different, as pointed out by Kumnick et al(177). In the following, the microstructural effect on the apparent diffusivities will be presented. A special experimental procedure described in Section 4.5.2 was adopted to study the effectiveness of hydrogen transport by dislocations during plastic deformation and these results will also be presented and discussed.

#### **5.4.2. Microstructural Effects on the Apparent Diffusivity of Hydrogen in Iron**

As shown in Figure 5-28, the microstructure of polycrystalline iron changes with total strain from a fully annealed structure to a well defined cell structure. The measured apparent diffusivities of hydrogen through these different microstructures in the absence of straining (dislocation transport) have been summarized in Figure 5-29. As can be seen the diffusivity decreases rapidly at low strains corresponding to the rapid increase in dislocation density; above about 8% strain, the apparent diffusivity seems to reach an asymptotic value corresponding to the development of a well defined cell structure. This results implies that major traps for hydrogen during plastic deformation are sessile dislocation arrays and this trapping effect must be taken into account in any study of hydrogen transport during plastic deformation.

#### **5.4.3. Effectiveness of Hydrogen Transport during Plastic Deformation**

Since it is obvious that dislocations can have dual roles in hydrogen transport behavior during plastic deformation, it is of importance to minimize differences in microstructure, such as sessile dislocation densities, when comparing the measured apparent diffusivities with and without dislocation transport.

The detailed experimental procedure adopted for this study is described

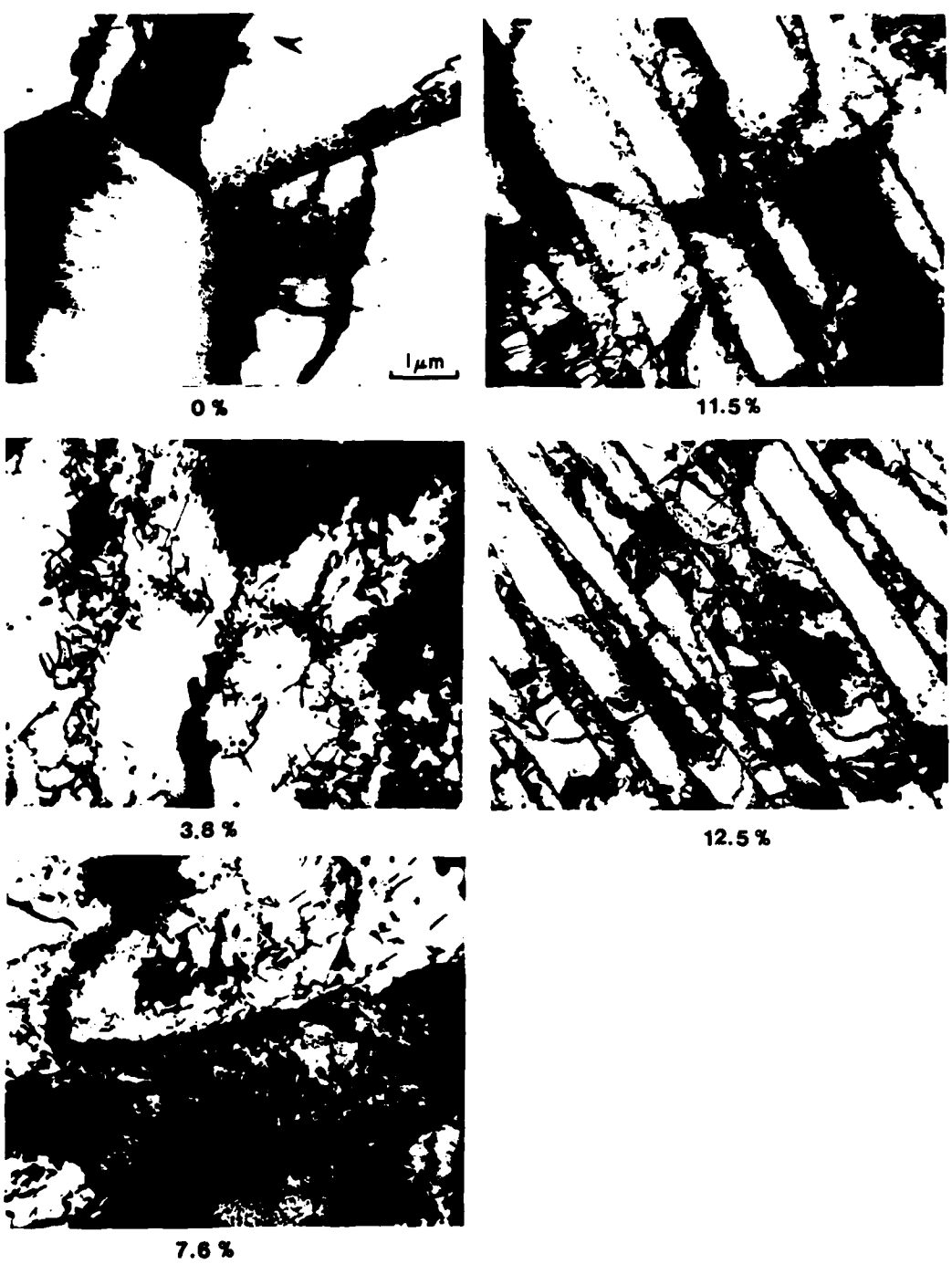


Figure 5-28: The microstructural change sequence as a function of tensile strain.

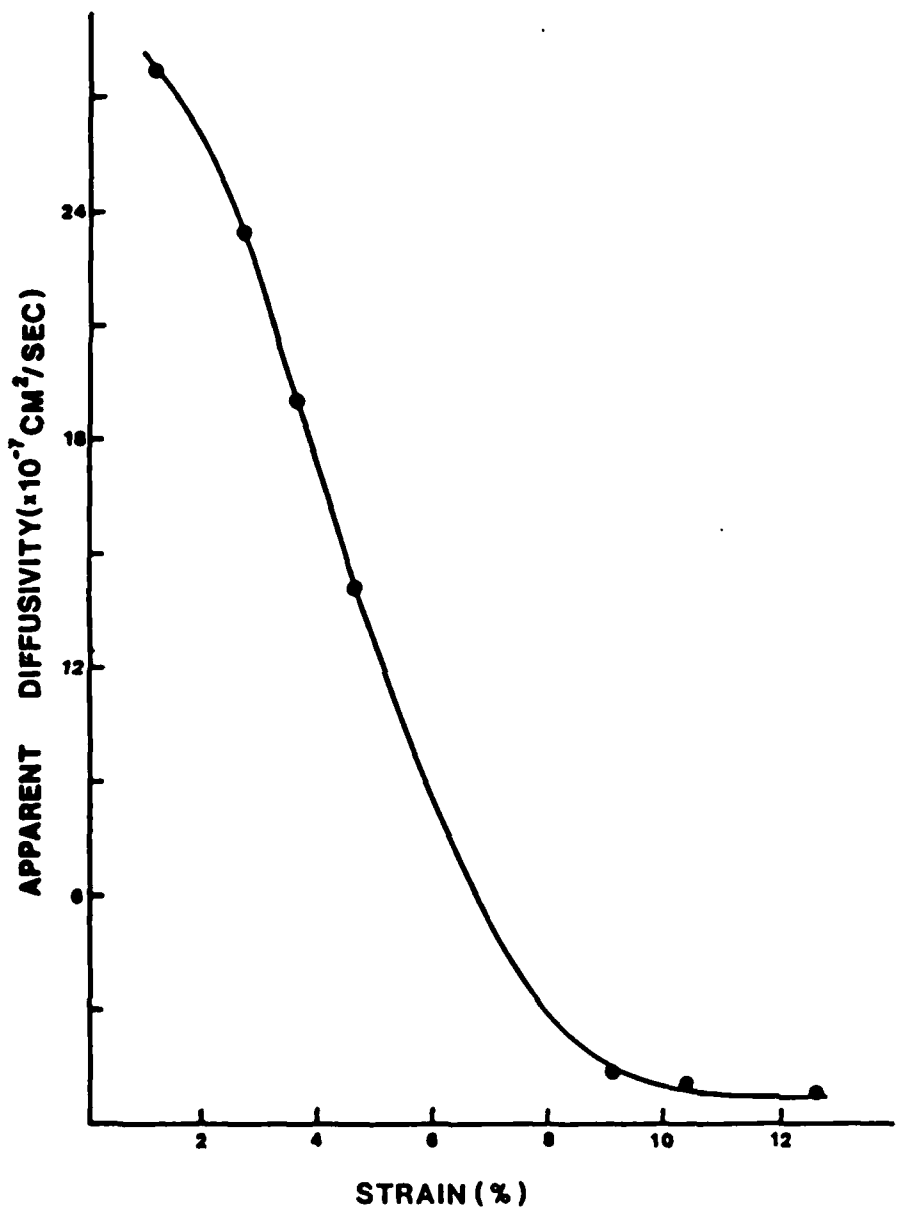


Figure 5-29: The apparent diffusivity in the absence of straining, as a function of tensile strain.

in Section 4.5.2. In contrast to the single crystal test where the steady state lattice hydrogen flux was always established before conducting any straining test, in this part of the study plastic deformation was initiated prior to introducing any hydrogen. After establishing a steady state background during straining, the hydrogen charging current was applied and the apparent diffusivity evaluated from the breakthrough time. As discussed in Chapter 4, this method monitors the fastest diffusion path, likely dislocation transport, and can be used to compare between the dislocation transport rate and the lattice diffusion rate of hydrogen in the presence and absence of dislocation substructure. Figure 5-30 shows the effect of strain rate on the apparent diffusivity during straining normalized by the apparent diffusivity in the absence of straining. A 30-fold increase in the apparent diffusivity was found for the highest strain rate employed, but unlike the single crystal test there seems to be no break-away dislocation velocity detected, although very high strain rates could not be used due to surface effect instabilities.

At lower strain rates, the apparent diffusivity in the presence of straining approaches that without straining, in contrast to the single crystal results where the hydrogen transport rate by mobile dislocations was always greater. The most likely explanation is that the higher dislocation multiplication rate and the shorter dislocation mean free path allows trapping to almost always dominate over transport in polycrystals at slower strain rates. However, this finding does not exclude the possibility that the redistribution rate of hydrogen within the specimen can be much faster during straining, even when no obvious increase in the apparent diffusivity could be detected experimentally. A faster redistribution rate of hydrogen may be quite important during crack initiation where it is widely believed that a critical hydrogen concentration is needed; enhanced local transport can be of importance in achieving this local critical hydrogen concentration. This implication as well as other direct effects of dislocation transport on local deformation and fracture events will be discussed in more detail in the subsequent section on supersaturation effects.

### 5.5. A Descriptive Model for Dislocation Transport of Hydrogen during Plastic Deformation

There have been many modelling attempts to describe the interaction between hydrogen and dislocations in the literature(71-72,174). However most of these have concentrated on the trapping effects due to stationary dislocations. Recently, Hashimoto(95) has provided an interesting model based on a modified McNabb-Foster's formulation(71), which simultaneously considered the transport and trapping effects of hydrogen during plastic deformation. In this thesis work, a similar though more simplified attempt has been made. Here instead of using a McNabb-Foster type trapping analysis, we started with Fick's second law and assumed the existence of only one kind of trap, dislocations, with a known interaction energy and density. This is quite reasonable for single crystals or relatively large grain polystalline pure iron specimens. We have also assumed that the mobile dislocation density is only a small portion of the total dislocation density and remains constant during straining, while the total (sessile) dislocation density increases(181). This assumption has been previously widely used and accepted in studies of dislocation mobility using strain cycling(188) or by stress relaxation methods(194).

Another required assumption is the direction of dislocation motion. In real systems, the dislocations can move in both directions depending on the applied stress and dislocation nature (e.g. right handed screw or left handed screw or the position of the extra half plane with respect to the stress). However, in the straining permeation test, where the hydrogen concentrations on both specimen surfaces are very different, with one at a null concentration (output surface) and the other at a non-zero constant concentration (input surface), it may thus be reasonable to assume that those dislocations which move from input surface to output surface carry much more hydrogen than those in the other direction. We have thus reasonably assumed that the hydrogen-carrying mobile dislocations move only in one direction, from the input to the output surface. This assumption might have artificially enlarged the forward dislocation transport hydrogen flux by neglecting the backward hydrogen flux transport by dislocations moving in the opposite direction. To compensate in part for this rather unusual assumption, we also assumed that the hydrogen concentration with dislocations obeys a Boltzmann's distribution

and maintains a local equilibrium value with lattice hydrogen. As the dislocation moves from the input surface to the output surface, the hydrogen concentration associated with it will thus decrease according to the instantaneous lattice hydrogen concentration. While this is counter to the kinetic nature of the hydrogen transport process as previously discussed, a dislocation should be able to drag almost all its hydrogen with it even if the surrounding lattice hydrogen concentration is very low(95). However we believe that this assumption taken together with the one of uni-directional dislocation motion would counter each other to minimize the difference between model and reality. It must be reemphasized that the assumptions used here are quite crude and the present modelling attempt should be regarded as only a descriptive approach to separate out the various contributions to the total flux. The directions for necessary refinements have been discussed by Hashimoto(95).

Based on these assumptions, equations involved in this modelling attempt can be formulated. The detailed development of these equation is presented in Appendix A. The resultant final equation is listed as follows.

$$\frac{\partial C_L}{\partial t} + \frac{\partial \rho_s C_L}{\partial t} b^2 \exp(-E_B/kT) + \frac{\partial C_L}{\partial t} \rho_m b^2 \exp(-E_B/kT) = D \frac{\partial^2 C_L}{\partial x^2} - \frac{\partial C_L}{\partial x} \rho_m b^2 v \exp(-E_B/kT). \quad (5.1)$$

$C_L$ : lattice concentration

$t$ : time

$\rho_s$ : sessile dislocation density, which is a function of time. ( $\rho_s = 10^7 + 10^6 t \text{ cm}/\text{cm}^3$  (181))

$\rho_m$ : mobile dislocation density, with boundary conditions  $\rho_m = 0$  at  $t = 0$ ,  $\rho_m = 10^6 \text{ cm}/\text{cm}^3$  at  $t > 0$

$E_B$ : binding energy between hydrogen and dislocation ( $E_B = 30 \text{ kJ}/\text{mole}$ )

$k$ : Boltzmann's constant, ( $k = 1.38 \times 10^{-16} \text{ erg}/\text{K}$ )

$T$ : temperature in K, ( $T = 295 \text{ K}$ )

$b$ : Burgers vector, ( $b = 2.58 \times 10^{-8} \text{ cm}$ )

D: lattice diffusivity, ( $D = 10^{-6} \text{ cm}^2/\text{sec}$ )

v: average dislocation velocity, ( $v = 4 \times 10^{-3} \text{ cm/sec}$  at strain rate  $1 \times 10^{-5} \text{ sec}^{-1}$ )

As it can be seen, there are separate terms describing the trapping and transport effects, so that these two effects can be separately evaluated. Three different cases, trapping only, transport only, and combined trapping and transport, have been solved numerically by finite difference methods; a detailed calculation is presented in Appendix A, and the results are shown in Figure 5-31. It is clear that in this model, as the dislocation density increases linearly with time, which applies for small strains, the trapping effect by newly generated dislocations is dominant as manifested in the total flux. This is true even in the combined effect case, where there is definitely an enhanced hydrogen flux due to dislocation transport, as indicated in Figure 5-31. This result is consistent with the experimental observation of the early strain flux behavior. It is speculated that if the model could be adjusted such that the dislocation density would saturate at higher strains, the increase in flux observed experimentally in the larger total strain should appear in the model as well.

Although this modelling effort could be clearly improved to more realistically mirror experimental conditions, because of the excessive computation costs and the many inevitable over-simplified assumptions, we have decided not to pursue this modelling work further, particularly since it is beyond the intended scope of the thesis.

In summarizing this modelling attempt, we have been able to demonstrate that hydrogen can be transported by dislocations. At early strains when the dislocation density increases rapidly, the trapping effect by dislocations is overwhelming and the total flux decreases. However, without this interference of the trapping effect, dislocations can efficiently transport hydrogen. Thus, even with this simplified model we can account for redistribution of hydrogen during plastic deformation. Even though the total hydrogen passing through per unit area is lowered, the amount of hydrogen remained and redistributed within per unit volume is greater, which may lead to events where the local critical hydrogen concentration is exceeded around potential crack initiation sites and this can be entirely due to this dislocation transport mode.

### Modified Hydrogen Flux Profile

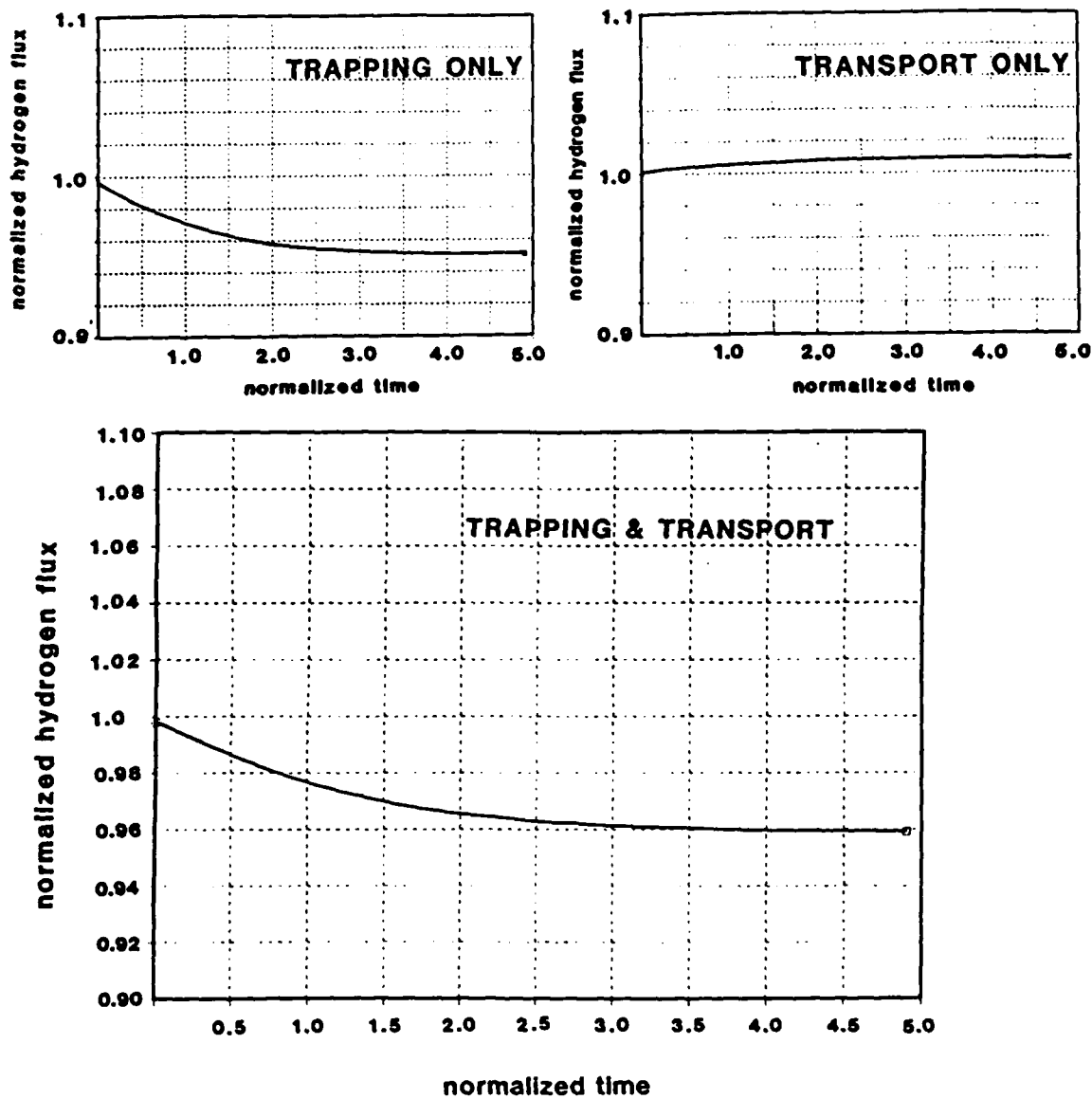


Figure 5-31: The modified hydrogen flux profile for three different modelling conditions as indicated.

## 5.6. Hydrogen Supersaturation Associated with Dislocation Transport

### 5.6.1. Evidence by Transmission Electron Microscopy

Although the occurrence of dislocation transport by hydrogen seems to be well established, the possibility that such an occurrence can lead to a significant increase in hydrogen embrittlement is still unclear. To examine this possibility, specimens taken from straining permeation tests were examined by transmission electron microscopy; two areas, with and without exposure to hydrogen charging, were both carefully studied in order to identify any modifying effect of hydrogen on microstructural development during plastic deformation.

Figure 5-32 and Figure 5-33 shows the characteristic microstructure of hydrogen charged and hydrogen free, strained single crystal iron. Although the crystal is quite pure, there are still some spherical particles with sizes of a few micrometers in diameter. These spherical particles have been examined by scanning electron microscopy and energy dispersive X-ray analysis and found to be silicon-rich, as illustrated in Figure 5-34; they are speculated to be silica (or iron silicide) particles formed during melting and retained in the material after casting. In addition, the low concentration (see Section 4.2.1) of mobile "locking" lattice interstitials, such as C and N allowed many of the dislocations to move out of the foil during observation, activated by the thermal energy of the electron beam. This dislocation movement left surface steps as illustrated in Figure 5-32 and Figure 5-33. Trace analysis performed on these areas with two different zone axes has clearly shown that those steps are parallel to the  $\langle 111 \rangle$  directions, as are the majority of dislocations remaining in the matrix. These observations are consistent with these being screw dislocations, in agreement with the literature that in iron crystals deformed at room temperature, the screw dislocations are dominant in the deformation process(98, 120). As we have discussed this is attributable to the intrinsically higher Peierls force (lattice friction) for screw dislocation motion, resulting in a much faster mobility for edge dislocations whose population is then exhausted at low strains.

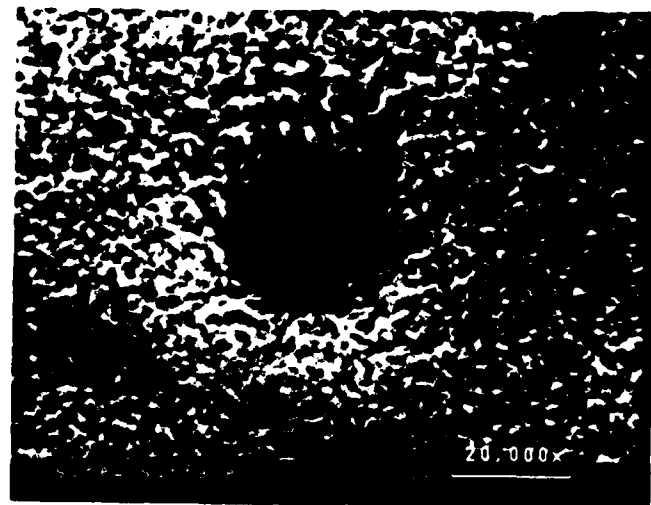
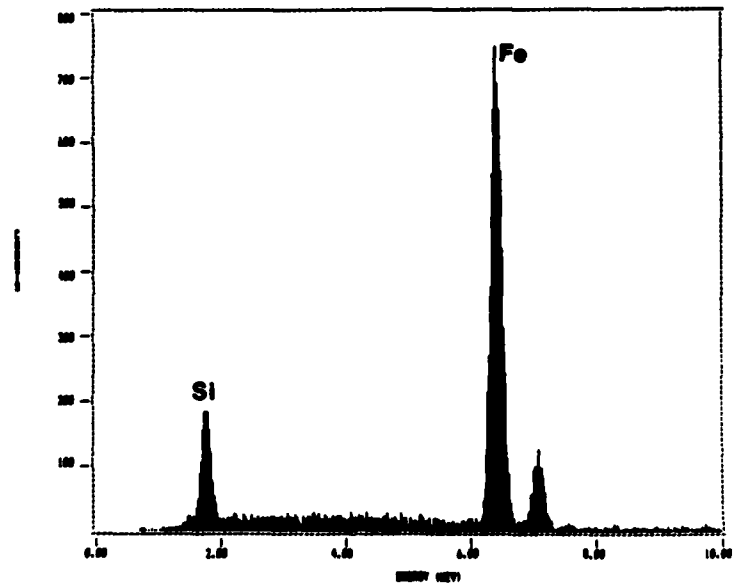
Both hydrogen charged and hydrogen free regions showed the same general type of dislocation configuration at strains of about 5%. However there



**Figure 5-32:** Dislocation structure in the hydrogen charged region of a "screw dislocation" single crystal at about 5% strain.



**Figure 5-33:** Dislocation structure in the hydrogen free region of the same single crystal in Figure 5-32.

**A****B**

**Figure 5-34:** (a) SEM micrograph of silicon rich spherical particle. (b) Energy dispersive spectrum (EDS) of the particle in (a).

are some striking differences; for example in the uncharged region, more secondary slip dislocations are observed than in the hydrogen charged region. This is clearly seen in Figure 5-32 and Figure 5-33. The same conclusion has been reached by Kimura et al(98), who studied the work hardening behavior of single crystal iron under hydrogen charging condition and found that hydrogen increased the easy glide strain range when only one slip system is operating. They interpreted this increase in easy glide strain as due to an increase in primary screw dislocation mobility due to hydrogen; this overrides the onset of a secondary slip system, so that the primary slip system will operate until a larger strain.

An important difference observed in this study, as shown in Figure 5-35, is that a relatively uniform dislocation tangled structure was found around the large silicon rich particles in the hydrogen free portion of the SPT specimen, while in contrast, within the hydrogen charged region, a very different type of dislocation structure existed. Figure 5-36 shows the dislocation structure associated with particles in the hydrogen charged specimen. Particles presumably have trapped a large amount of hydrogen during the straining permeation test by dislocation transport. In such a case, the strain around the particles is highly localized and concentrated along a particular direction. Unlike the adjoining matrix where only one slip system dominates, this localized strain region was found to be composed of several different slip systems. A detailed electron diffraction analysis, presented in Appendix B, has been carried out to determine the operating slip systems participating in this localization process. It was found that in addition to the expected primary system,  $(\bar{1}12)[1\bar{1}1]$ , there are at least two other slip systems operating,  $(1\bar{1}2)[\bar{1}11]$ ,  $(\bar{2}11)[111]$ , as illustrated in Figure 5-36. The sequence and interaction appears to be as follows: Only two slip systems,  $(\bar{1}12)[1\bar{1}1]$ ,  $(\bar{2}11)[111]$ , are usually found at the tip of the tangled structure suggesting that the third slip system was somehow generated by the presence of or through the interaction between the first two, leading to the final dense dislocation tangled structure. To further elucidate this point, a sketch tracing the dislocation images around the localized strain is shown in Figure 5-37, demonstrating that the third slip system is largely confined to and is responsible for stabilizing the tangling structure. Possible reasons for this will be considered subsequently. Because of their size and small number, the large

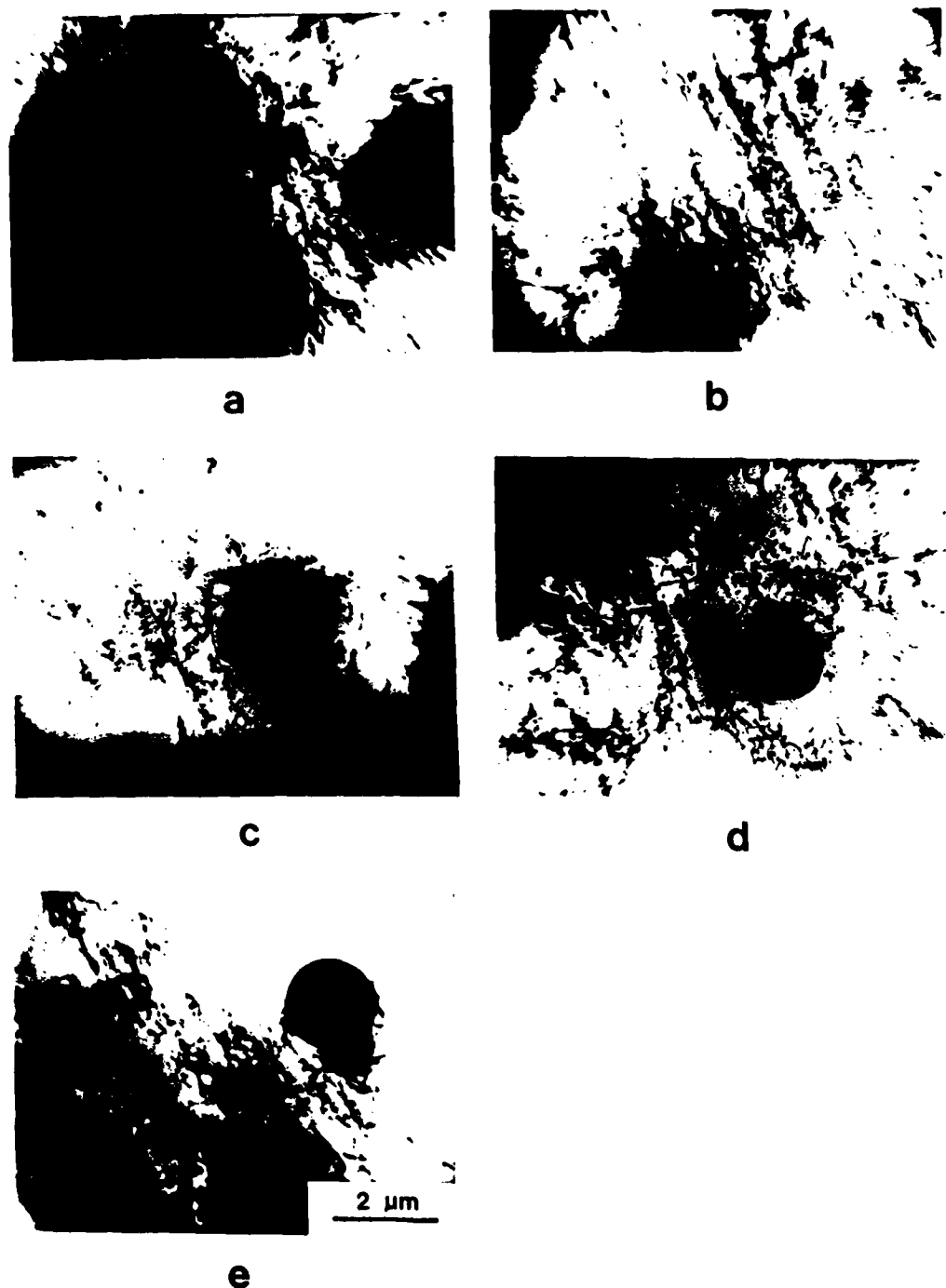


**Figure 5-35:** A collection of the dislocation structures around spherical particles found in the hydrogen free region of a "screw orientation" single crystal at about 5% total strain.

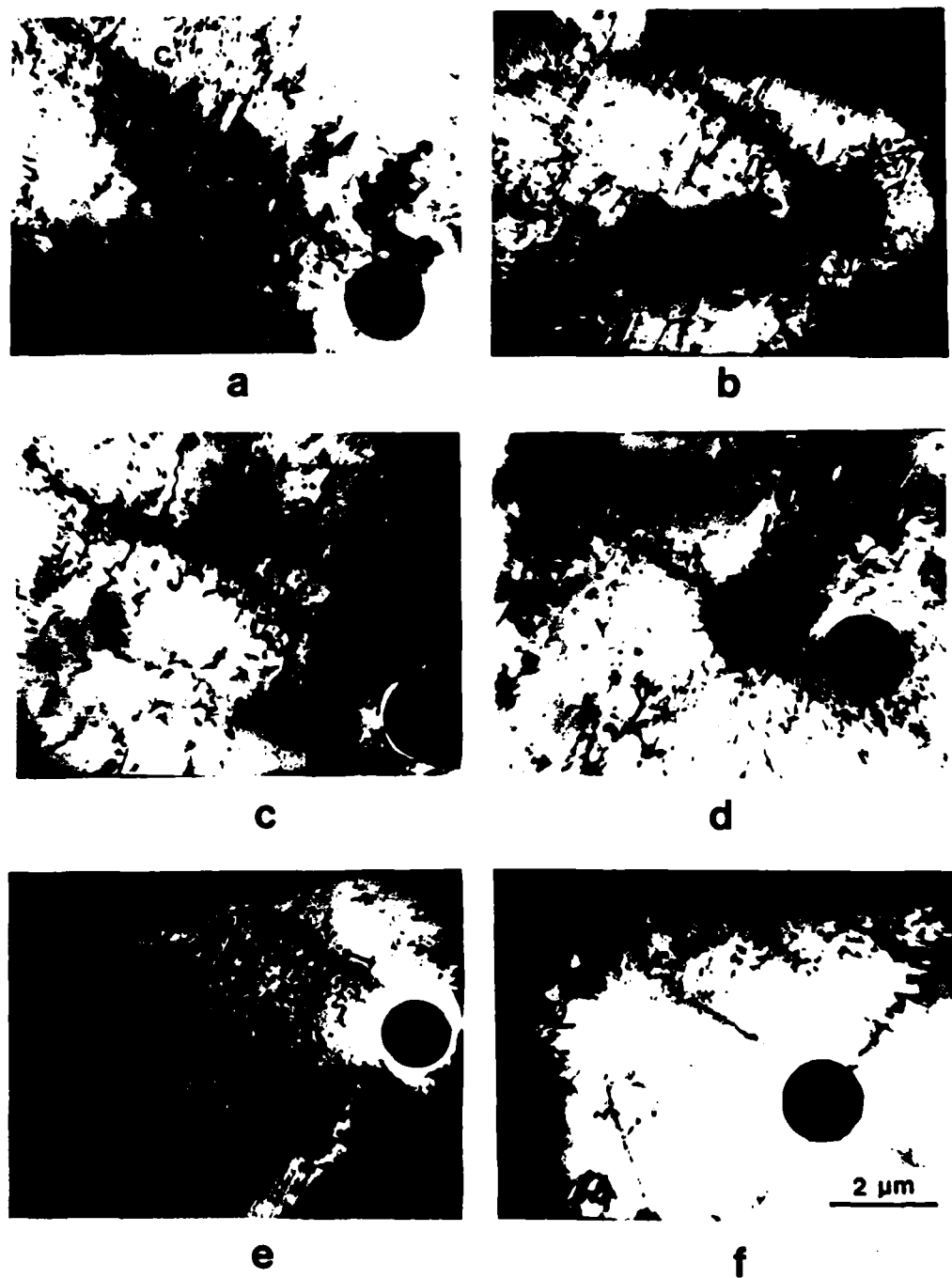
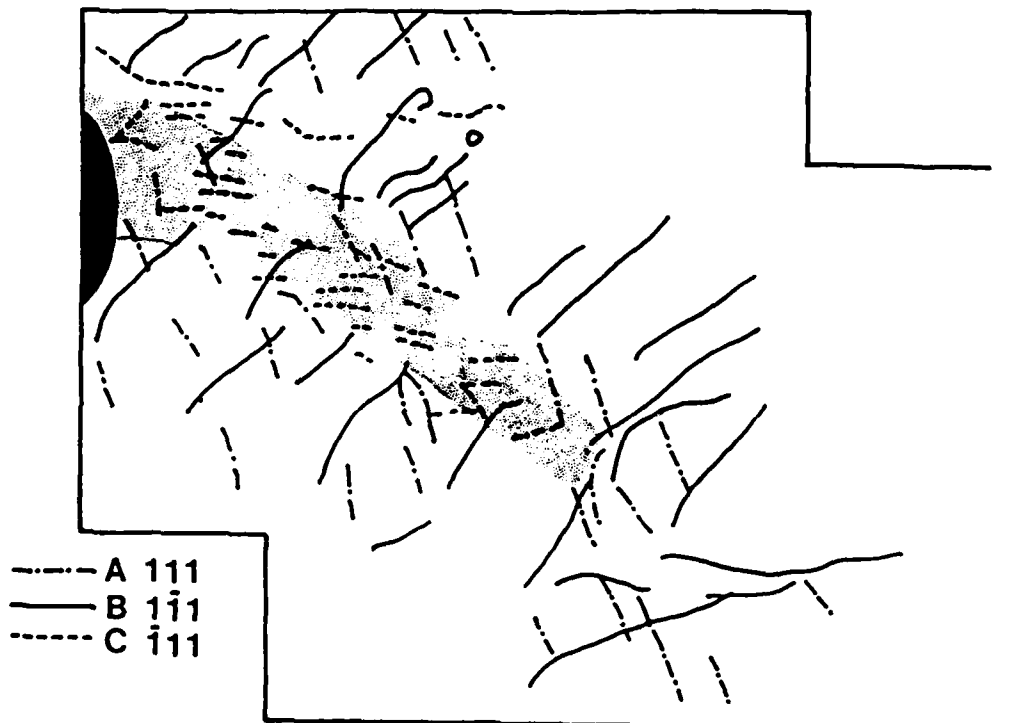


Figure 5-36: A collection of the dislocation structures around spherical particles found in the hydrogen charged region of the same single crystal in Figure 5-35.

spherical particles were rarely found in the thin foils, most in fact being lost during thinning. However a number were examined in both hydrogen charged and uncharged sections respectively, as illustrated in Figure 5-35 and Figure 5-36. This clear evidence for straining localization only in the hydrogen case precludes this effect being due to any thin foil handling effects or other artifacts.

Further, more detailed analyses were not possible with a 100 KeV TEM but this promises to be an area of continuing and fruitful study. Notwithstanding the limitations of the present TEM there were additional observations that could be made, as detailed below. Another interesting and likely important observation is that this tangled structure seems to occur discontinuously, as indicated in Figure 5-36(a); it appears to be composed of three slightly shifted units marked A, B and C in the figure; the dislocations between them are much less concentrated. It is speculated that these units occurred sequentially, and remained to be linked by subsequently generated dislocations. A similar condition can also be seen in Figure 5-39(b), where the second and perhaps the third tangled unit are about to form. It is intriguing that this periodic dislocation structure resembles crack propagation in a hydrogen environment where discontinuous crack growth is often found(195).

In all cases examined, the same crystallographic direction for the main axis of the strain localization band was found; it is approximately along the [112] orientation and perpendicular to the primary slip plane traces on the (110) plane. This particular direction is about 30 degrees away from the tensile axis, as shown in Figure 5-38, which does not match with either the maximum shear orientation (45 degrees from the tensile axis), or the pure shear orientation (55 degrees from the tensile axis) angles predicted for an isotropic, elastic matrix (152-153). While the direction may result from the nonisotropic or nonelastic behavior of iron, this has not been established, nor can it be simply predicted what slip planes will have the greatest resolved shear stress for the unknown stress field generated by the tensile stress, the particle and the trapped (perhaps recombined) hydrogen. It is quite possible, though considered unlikely that the observed orientation may be fortuitous; more likely it points to a unique role of hydrogen in modifying how dislocations react and interact in iron. It is planned that future work will employ an elasto-plastic analysis using suitable material constants to



**Figure 5-37:** A sketch of dislocations on different slip systems participating in the strain localization structure. See Appendix B for detailed analyses.

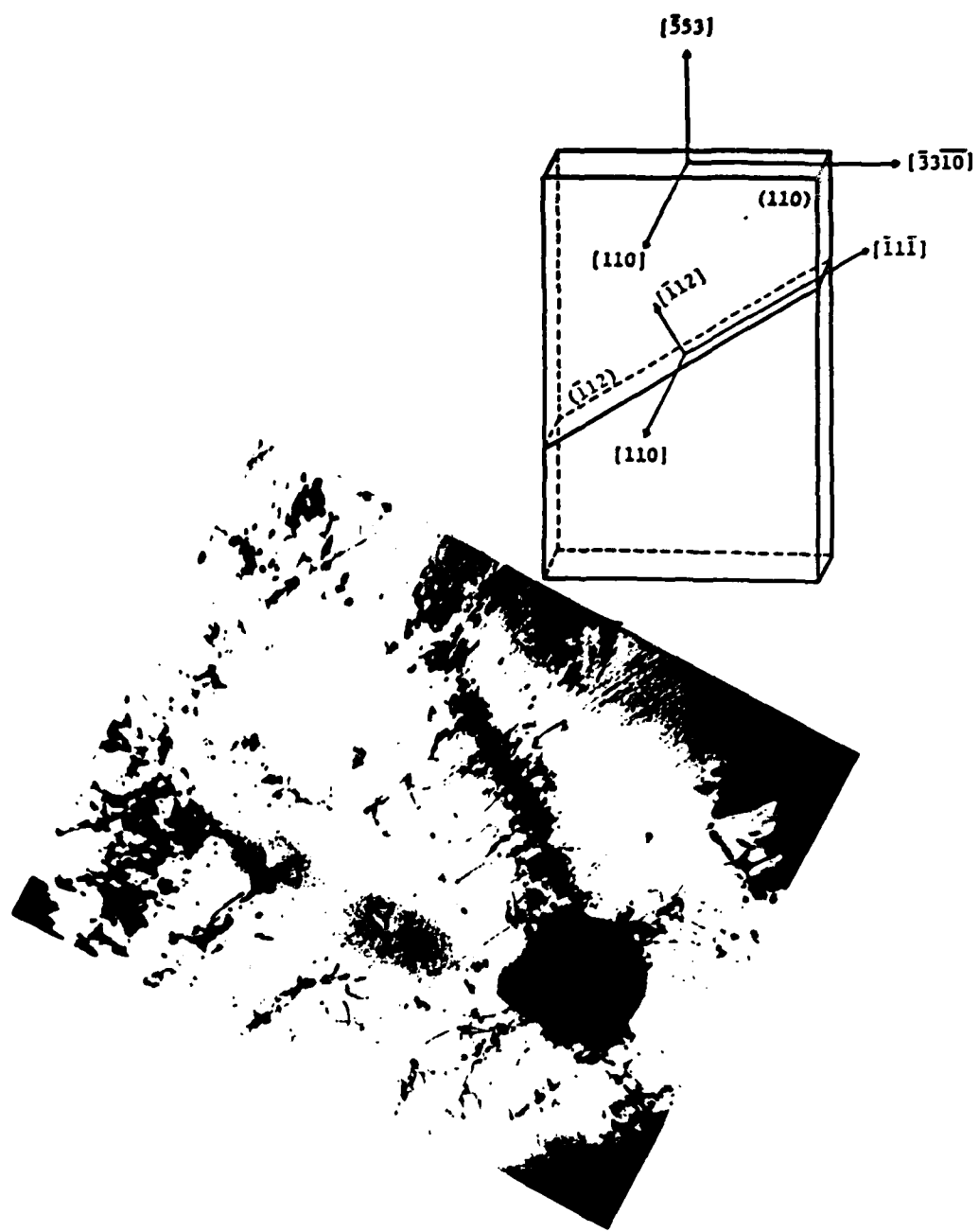


Figure 5-38: The orientation relationships between the strain localization direction on the (110) plane and the tensile axis.

calculate the stress and strain distribution around the particle for our given boundary condition.

Even though the strain localization around the particles is clearly caused by hydrogen, it is found that the hydrogen charging condition during straining permeation tests was not sufficient to cause any obvious surface blisters, indicating that no large scale irreversible damage was introduced during the tests. However it is clear that tangling was induced by excess localization of hydrogen transported by dislocations to the particles which can lead to local supersaturation, for reasons discussed by Bernstein and Thompson(100). Similar observations of hydrogen-induced micro-plasticity have also been reported(44,46,63). If this local excess concentration promotes irreversible plastic deformation which then occurs along a particular orientation in the form of a tangled dislocation structure, as in fact has been observed here and by in-situ TEM studies(62), this could be the precursor for hydrogen induced cracking. As already implied, the local hydrogen supersaturation can lead to either pressurization resulting from hydrogen gas enrichment, or an enhanced transient lattice concentration build-up, both occurring at or near traps. The first possibility requires the presence of microvoids as sites for hydrogen recombination, and while none were observed in the vicinity of the tangling, we are not able to yet discount this possibility. However we believe it more likely that a transient hydrogen concentration build-up occurs which, in combination with local stresses, leads to an enhanced localized straining.

In possible support of this latter possibility we have previously found that hydrogen tends to promote the formation of particle associated microtwins in iron cathodically charged at room temperature(63); these have also been found in hydrogen containing iron deformed at low temperature(196). This twinning formation could serve as another example of the operation of a strain relief process catalyzed by hydrogen supersaturation. In the present study, two out of three slip systems identified in the dislocation tangled structure are in the twinning directions, while the primary slip system is in the anti-twinning direction. One intriguing possibility is that hydrogen enhances local dislocation generation in the twinning direction and the movement of such dislocations could, in some cases, initiate microtwin formation. This is in the spirit of the proposal by Mahajan(197), that the dislocation core can split into a three layer microtwin which can then interact with other

microtwins and grow in response to further straining. If, however there are, in addition, competitive slip systems to accomodate the further straining, such as in our case where the primary slip system is in the anti-twinning orientation, too high a stress may be required to generate twins and the response to enhanced local deformation may instead be highly localized slip.

While we still do not fully understand this phenomenon of hydrogen induced strain localization, several possibilities can serve as the basis for future work.

- Hydrogen reduces the Peierls stress thus enhancing dislocation mobility(198).
- Hydrogen reduces the stacking fault energy of bcc iron, favoring the generation of twinning dislocations.
- Due to the mutual enhancement of the interaction between hydrogen and dislocations, the resultant dislocation structure is thus highly localized.

We can speculate that these three processes should occur concurrently to give rise to the observed phenomenon. The need for additional, much more detailed analytical studies is clear.

#### 5.6.2. The Morphology of Cracks Induced by Hydrogen Supersaturation

Two types of hydrogen charging procedures were conducted on the screw orientation single crystals (see Figure 5-4), as mentioned in Section 4.6. The first was to cathodically charge with hydrogen to intentionally produce surface blisters and internal cracks, in the absence of external straining. The second was to concurrently strain during hydrogen charging (straining electrode test, SET) to intentionally produce particle associated strain localization, followed by charging with hydrogen under more severe conditions, to study where cracks initiate in this type of dislocation structure. These two test techniques were then examined and compared to reveal the effect of dislocation transport on the crack morphologies.

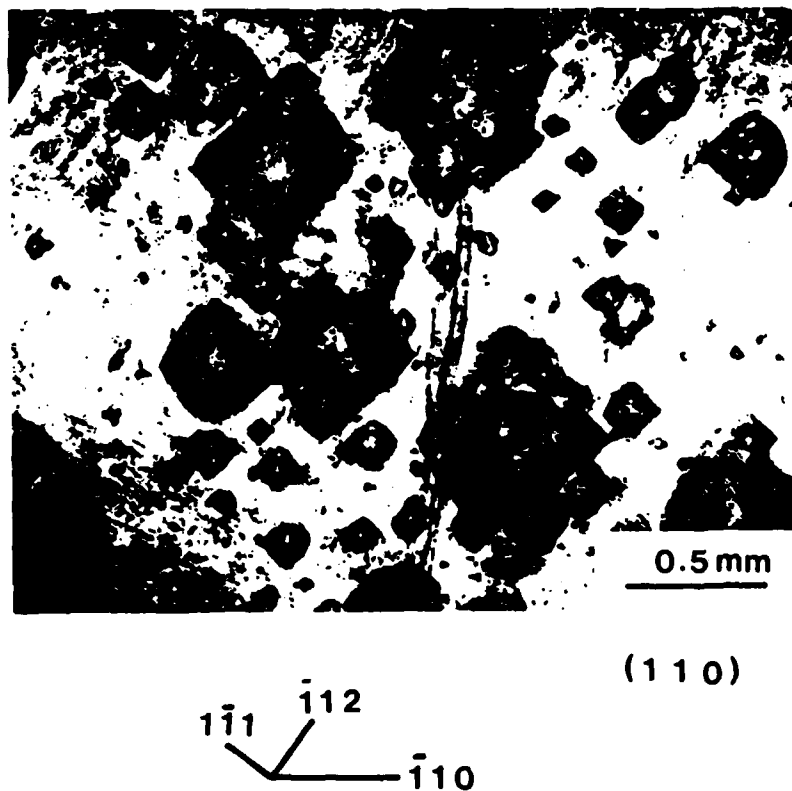
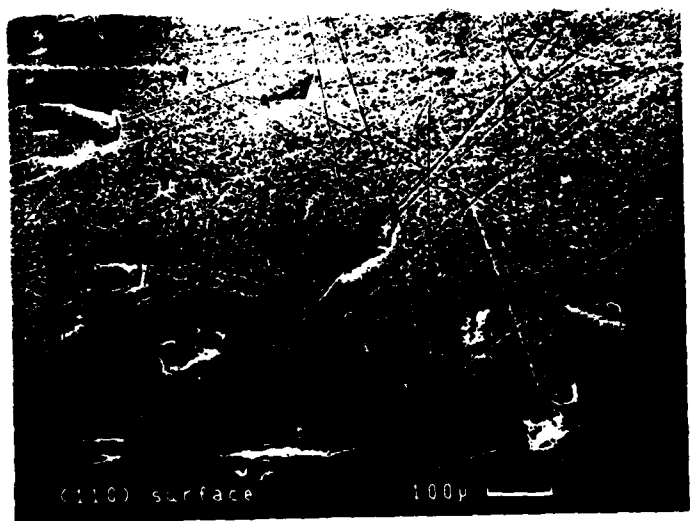


Figure 5-39: Light micrograph of surface blisters on a (110) plane, resulting from hydrogen charging.



001  
— i10

**Figure 5-40:** Internal cracks underneath the surface blisters shown in Figure 5-39.

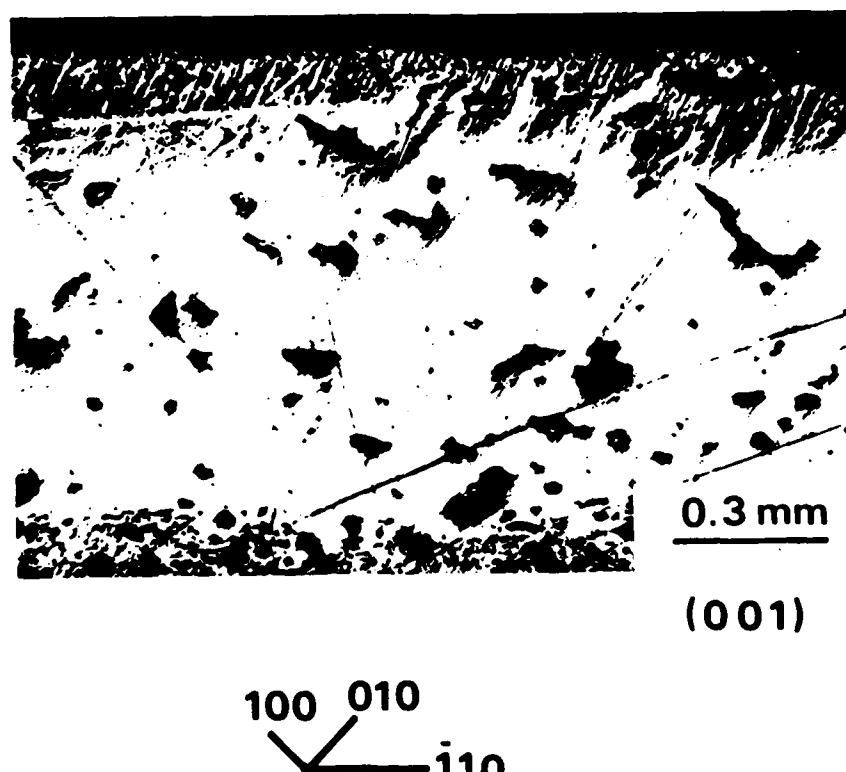
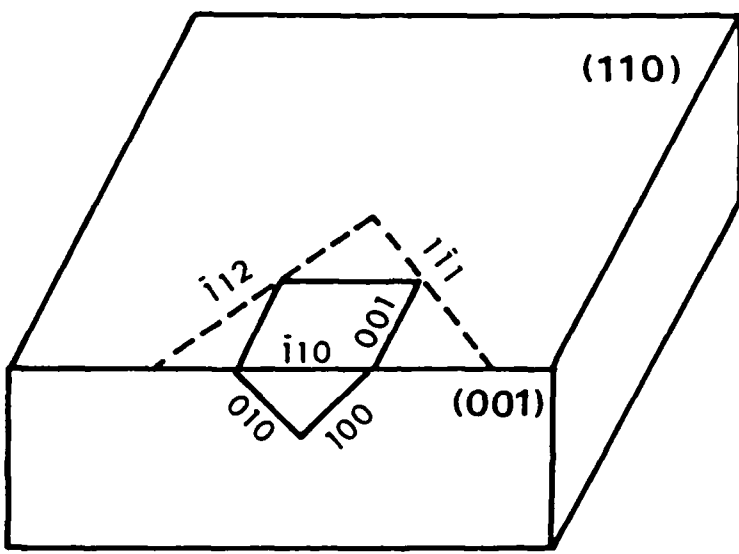
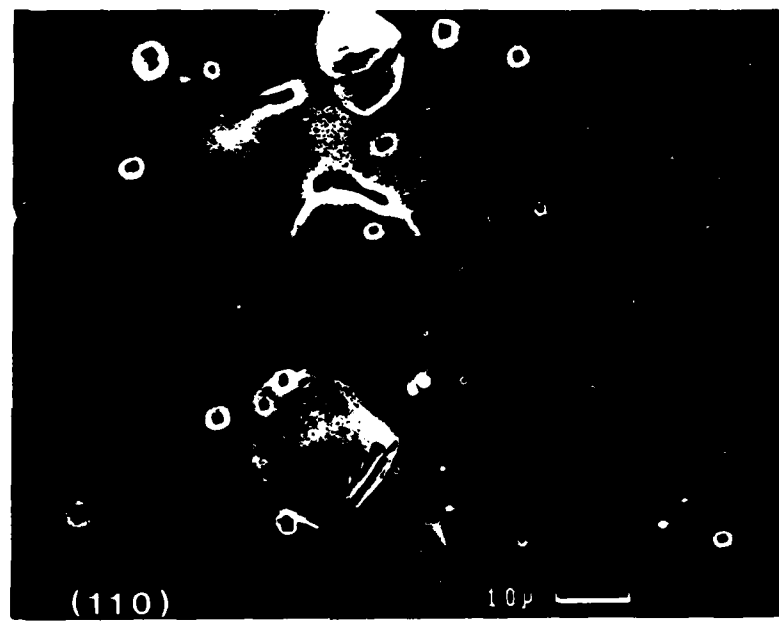


Figure 5-41: Internal cracks on a (001) plane of the same crystal in Figure 5-40 resulting from hydrogen charging.



— INTERNAL CRACK  
---- SURFACE BLISTER

Figure 5-42: A sketch of hydrogen-charging induced surface blisters and internal cracks, with the proper indexed orientation relationship.



553  
111      112

Figure 5-43: The early stage of the (110) surface blister formation of a SET single crystal specimen.

actively involved in the blister formation process, not surprisingly due to the ease of activating this system. More importantly, even at the very early stage of this blister formation process, a crack has been found along a [112] direction on a (110) plane, which matches very well with the strain localization direction, presented in the previous section. This observation is in agreement with our expectation that the presence of strain localization associated with the particles can serve as prime potential crack initiation sites and initial crack propagation path.

While further work is needed to systematically study the process of crack initiation and growth under the influence of hydrogen supersaturation induced by dislocation transport, there are obvious differences between the two charging conditions examined. Currently we are not able to resolve the reasons for this. Nevertheless, the observation of how strain localization developed due to hydrogen and the direct correspondence between it and the formation of hydrogen-induced microcracks is a major finding which when further elucidated should provide a much clearer picture of how hydrogen changes the mechanical response of iron and presumably other alloys.

## Chapter 6 Conclusion

The primary goal of this thesis was to develop a greater understanding of the phenomenology and mechanism of dislocation transport of hydrogen during plastic deformation of bcc iron. An accurate and reliable experimental approach has been devised through the use of properly oriented pure iron single crystals, the construction of a slow strain rate tensile testing machine equipped with a well-aligned grip system, and a pair of sophisticated electrochemical cells. It is believed that the experimental uncertainties have been reduced to the minimum in this study, so that the often small hydrogen flux changes due to dislocation transport can be accurately monitored and measured.

In the crystals used in this investigation, the slip systems predicted by Schmid's law have been characterized and confirmed in that for a tensile axis oriented along the  $\langle 110 \rangle$ - $\langle 111 \rangle$  boundary of a crystallographic unit triangle, the primary slip system is of the {112} type slip plane and along a  $\langle 111 \rangle$  type slip direction.

By using single crystals with proper combinations of surface orientation and tensile axis, the hydrogen transport rate by edge, screw and mixed dislocations could be separately studied. It was found that for all three types of dislocation behavior within the crystal during plastic deformation, the measured hydrogen flux behavior can detect the egress of dislocation on the monitored crystal surface. In the case of screw dislocations, since the entire dislocation line intersects the crystal surface with a rapid release of most of its associated hydrogen, the flux due to dislocation transport is relatively discontinuous, manifested by distinct peaks in the flux. In contrast to this, in the cases of both edge and mixed dislocations, the dislocation segments intersecting the monitoring crystal surface are the kinks travelling along the screw dislocation lines, because the movement of screw dislocations continues

to be the predominant source of strain for iron crystals deformed at room temperature. The hydrogen flux in these cases is more continuous in appearance, reflecting the high emission frequency of kinks on the monitoring surface.

The dependence of hydrogen transport rate on functional parameters such as strain rate, lattice hydrogen concentration and temperature for the different dislocation types was also studied. It was found that the hydrogen transport rate generally increased as the strain rate decreased, due to the fact that at higher strain rates the hydrogen-carrying dislocation velocity could approach or exceed the break-away velocity beyond which the associated hydrogen atmosphere can no longer keep up with the dislocations. This is especially true for edge and mixed dislocations where the kink velocity is much faster than the nominal (average) dislocation velocity. At slower strain rates, the edge kinks seem to have the greatest capacity to transport hydrogen, consistent with their higher binding energy to hydrogen.

The absence of a strong lattice hydrogen concentration effect on the hydrogen transport rate by dislocation have been observed and attributed to the kinetic nature of this transport process. It is believed that thermodynamic equilibrium between the hydrogen associated with mobile dislocations and the lattice hydrogen is not readily obtainable, so that reversible equilibrium between the lattice and dislocation hydrogen concentration is unlikely to exert a great effect on the enhanced transport rate.

Only limited information on the temperature effect was developed. It was found that due to the restrictions of the electrochemical technique employed in this study, only a rather narrow temperature range, from 12°C to 78°C, was possible and in this range only an insignificant temperature dependence of the dislocation transport rate was observed, consistent with the expectation that the extra thermal energy provided by the increased temperature was too small to alter the interaction between hydrogen and mobile dislocations. On the other hand, this is also consistent with the effect of lattice hydrogen concentration on the hydrogen transport rate, since the lattice hydrogen concentration increased substantially with increasing temperature; however a minimal effect on hydrogen transport was observed.

In the single crystal tests mentioned above, significant trapping effects due to strain generated sessile dislocations were suppressed by limiting our study to the easy glide strain region, where the dislocation multiplication rate during plastic deformation was greatly reduced. To study the competition between hydrogen transport rate by mobile dislocations and the trapping effect mentioned above, polycrystalline iron specimens instead were used. The results showed that the apparent hydrogen diffusivity decreases with total strain, in response to the dislocation structures formed during plastic deformation. However by evaluating the ratios between the apparent diffusivities with and without the presence of dislocation transport, a 30-fold increase in apparent diffusivity due to hydrogen transport was found in the highest strain rate,  $6.9 \times 10^{-5} \text{ sec}^{-1}$ , employed.

A simple model was developed to characterize this combined effect of trapping and transport of hydrogen by dislocations during plastic deformation, based on Fick's first and second laws. By using available parametric data from the literature, the model accurately predicted that the transport effect can co-exist with the trapping effect even at very early strains where the dislocation multiplication rate is most significant. However, the combined flux results show that the trapping effect at early strain is the dominant factor for the condition where sessile dislocation traps can form.

In addition to the study of the hydrogen transport rate by mobile dislocations, the consequences of this transport mechanism on the possible development of hydrogen supersaturation around strong hydrogen traps were also examined. It was found that around the hydrogen-containing spherical inclusions, the dislocation structure could be highly localized, with this region consisting of several (at least three) different slip systems, in contrast to the matrix or the region around the same particles in hydrogen free specimens, where only primary slip predominated. Comparing the hydrogen charged and hydrogen free region from the same specimen, it was concluded that while hydrogen apparently enhances the mobility of primary screw dislocations in the matrix, it also can affect the local stress field associated with inclusion particles, to promote dislocation generation on slip systems compatible with twin formation. It is therefore speculated that two cases can occur: In one, if there is no competing slip system, these twinning-sense dislocations catalyzed by hydrogen can lead to the formation of crystallographic identifiable

twins(63). In the other, if a strong anti-twinning primary slip is in operation, as in this present study, this twinning process is suppressed, but the associated dislocations interact locally with the primary system to promote a tangled dislocation structure.

Finally, to correlate hydrogen-induced crack formation and possible embrittlement to the dislocation transport of hydrogen, the effect of hydrogen supersaturation on crack initiation or growth was studied for either high fugacity hydrogen charging in the absence of an applied stress or hydrogen charging following a SET test. It was found that for the former case, the resultant internal cracks were bounded by {100} and {110} types of planes, and the associated surface blisters appeared to be square in shape lying on a (110) plane, and bounded by [112] and [111] directions. In the latter, the orientation of the initiated crack was the same as the strain localization band observed in the straining permeation specimen; viz a [112] direction on a (110) plane. It is therefore concluded that it is possible to induce hydrogen supersaturations both from a thermodynamic sense (i.e. heavily charging with high fugacity hydrogen) and in a kinetic approach (i.e. dislocation transport with a much lower hydrogen fugacity), although consequent crack initiation and more likely growth can be different. This difference may be due to the different dislocation substructure induced by the interaction between the co-existing hydrogen and mobile dislocations in the latter case. In any event, a direct correspondence between the presence of hydrogen induced strain localization bands on the initiation of hydrogen-induced cracks has been demonstrated.

## Chapter 7

### Recommendations for Future Work

This thesis work has examined several different aspects of the mechanism by which dislocations can transport hydrogen in bcc iron. Further studies related to these findings are clearly warranted, as follows:

#### 1. Strain Localization

It was found that the hydrogen-dislocation interaction during plastic deformation promotes strain localization associated with inclusion particles. This phenomenon deserves further attention to fully understand the mechanistic process(es) through which the strain localization occurred. To achieve this goal, several different approaches can be suggested:

- High Voltage and High Resolution Transmission Electron Microscopy: It was recognized in this study that a thicker TEM thin foil is required to preserve the dislocation structure associated with the inclusion particles; especially information on the three dimensional dislocation structure information is desirable. A high voltage electron microscope will be needed to allow full characterization of the dislocation tangled structure.
- Crack Formation due to Dislocation Transport of Hydrogen: Crack morphology under the influence of dislocation transport of hydrogen also deserves further study both to relate the strain localization phenomenon to subsequent crack formation and to understand the mechanistic nature of how the hydrogen-dislocation interaction combines to accelerate the crack initiation process.
- Stress-Strain Analysis: A sophisticated stress-strain analysis around inclusions, taking into account the material plastic behavior and anisotropic effect is highly desirable to explore the effect of hydrogen on the local stress-strain field associated with the inclusions. This analysis would help further characterize and predict the specific direction for the development of strain localization.

#### 2. Hydrogen Supersaturation due to Dislocation transport

To relate dislocation transport to hydrogen embrittlement, studies of the development of hydrogen supersaturation resulting from dislocation transport are critical. One possibility suggested was local pressurization. A carefully designed material with pre-existing microvoids can be used to study this hypothesis, which if successful can then be related to understanding hydrogen's effect on ductile fracture processes, where microvoid formation and coalescence have been found to be greatly influenced by the presence of hydrogen.

### 3. Mathematic Modelling of Hydrogen Transport Rates by Different Dislocations

Experimental measurements of hydrogen transport rates by edge, screw and mixed dislocations have been carried out in this study. Speculations of how different dislocations can carry hydrogen during plastic deformation were suggested. A much more detailed mathematical model, accounting for crystal surface orientation and the detailed dislocation characteristics, such as mobile dislocation density, dislocation velocity etc., as well as the stress dependence of hydrogen permeability is necessary to further elucidate the hydrogen-carrying capability of different dislocations.

### 4. Hydrogen Transport Rates by Different Dislocation Types

The hydrogen transport rates by different dislocation types have been studied in this thesis as functions of strain rate, lattice hydrogen concentration and temperature. Further investigations of this subject can be suggested as follows:

- Temperature Effect: The temperature range used in this study has been limited by the electrochemical techniques to operate within a rather narrow temperature range. However, it is important to study the hydrogen transport rate in a much wider temperature range within which the thermal energy can be effectively varied to study the hydrogen-dislocation interaction. It also be important, with respect to the effect of dislocation dynamics on hydrogen transport rate, since at higher temperature the mobility of edge and screw dislocations can be comparative and the measurement of hydrogen transport rate by edge dislocation lines instead of edge kinks on screw dislocations will be possible. A wider temperature range can be made possible by using alcohol-based electrolytes at lower temperatures and conversely, by using various salts for electrolytes at higher temperatures. Another possible alternative is to use a gas phase hydrogen charging and detecting experimental set-up.

- Lattice Hydrogen Concentration Effect: In this study an insignificant lattice hydrogen concentration on hydrogen transport by dislocations was found and a saturated hydrogen concentration in the dislocation core at the smallest hydrogen charging current density,  $0.5 \text{ mA/cm}^2$ , used was speculated. It is possible to use an even lower cathodic charging current density, or use low fugacity gas phase charging to effectively alter the dislocation core hydrogen atmosphere, so that the effect of lattice hydrogen on modifying the hydrogen transport rate by dislocation can be studied.
- Alloying Effects: Instead of using pure iron crystals, other single crystals such as Fe-Si or Fe-Al can also be used to alter the dislocation behavior during plastic deformation (more planar) by reducing the stacking fault energy of the iron lattice. The corresponding hydrogen transport rate by dislocations and resultant microstructure will be valuable informations toward the fundamental understanding of mutual influences of hydrogen transport and dislocation dynamics.

## Chapter 8 References

1. Y.H Kim and J.W. Morris Jr.: Met. Trans., 14A, 1983, 1883
2. R. Garber, I.M. Bernstein and A.W. Thompson: Met. Trans., 12A, 1981, 225
3. I.M. Bernstein: Mater. Sci. Eng., 6, 1970, 1
4. A.S Tetelman and W.A Robertson: Acta Met., 11, 1963, 415
5. A.S Tetelman and W.A Robertson: Trans. TMS-AIME, 224, 1962, 775
6. C. Zapffe and C. Sims: Trans. Met. Soc., AIME, 145, 1941, 225
7. N.J. Petch and P. Stables: Nature, 169, 1952, 842
8. N.J. Petch: Phil. Mag. Ser.A, 1, 1956, 331
9. R.A. Oriani and P.H. Josephic: Acta Met., 25, 1977, 979
10. A.R. Troiano: J. Iron Steel Inst., 189, 1958, 37
11. A.R. Troiano: Trans. ASM, 52, 1960, 54
12. R.A. Oriani and P.H. Josephic: Acta Met., 22, 1974, 1065
13. B.A. Wilcox and R.A. Huggins: J. Less-Comm Met., 2, 1960, 292
14. A.M. Adair: Trans. AIME, 236, 1966, 1613
15. I.M. Bernstein: Scripta Met., 8, 1974, 343
16. C.D. Beachem: Met. Trans., 3, 1972, 437
17. S. Asano and R. Otsuka: Scripta Met., 10, 1976, 1015

18. H. Kimura, H. Matsui, S. Takaki, A. Kimura and K. Oguri: Mechanical Properties of BCC Metals, M. Meshii eds., TMS-AIME, Warrendale, PA, 1981, 125
19. A.N. Stroh: Adv. in Phys., 6, 1957, 418
20. S.P. Lynch: Metals Forum, 2, 1979, 189
21. J.J. Gilman: Phil. Mag., 26, 1972, 801
22. J.T. Brown and W.M. Baldwin: Trans. AIME, 200, 1954, 298
23. H.K. Birnbaum: Atomistics of Fracture, Proc. of NATO Conf., R.M. Latanisión and J.R. Pickens eds., Plenum Press, New York, 1981, 733
24. J.P. Hirth: Met. Trans., 11A, 1980, 861
25. M.R. Louthan, G.R. Caskey, J.A. Donovan and D.E. Rawl: Mater. Sci. Eng., 10, 1972, 357
26. R.M. Vennet and G.S. Ansell: Trans. ASM, 60, 1967, 242
27. R.M. Vennet and G.S. Ansell: Trans. ASM, 62, 1969, 1007
28. R.J. Walter, R.P. Jewett and W.T. Chandler: Mater. Sci. Eng., 5, 1969-70, 99
29. D.P. Williams and H.G. Nelson: Met. Trans., 1, 1970, 62
30. R.M. Latanision, M. Kurkela and F. Lee: Hydrogen Effects in Metals, I.M. Bernstein and A.W. Thompson eds., TMS-AIME, Warrendale, PA., 1980, 379
31. A.W. Thompson and B.A. Wilcox: Scripta Met., 6, 1972, 689
32. A.W. Thompson: Met. Trans., 4, 1973, 2819
33. A.W. Thompson: Mater. Sci. Eng., 14, 1974, 253
34. A.W. Thompson: Hydrogen in Metals, I.M. Bernstein and A.W. Thompson eds., ASM, Metals Park, Ohio, 1974, 91
35. A.W. Thompson: Met. Trans., 5, 1974, 1855

36. A.W. Thompson and J.A. Brooks: Met. Trans., 6A, 1975, 1431
37. A.W. Thompson and I.M. Bernstein: Adv. in Corr. Sci. and Tech., M.G. Fontana and R.W. Staehle eds., 7, Plenum Press, New York, 1980, 53
38. M. Taheri, J. Albrecht, I.M. Bernstein and A.W. Thompson: Scripta Met., 13, 1979, 871
39. G.R. Caskey Jr.: Scripta Met., 11, 1977, 1077
40. T.D. Lee, T. Goldenberg and J.P. Hirth: Met Trans, 10A, 1979, 199
41. T.D. Lee, T. Goldenberg and J.P. Hirth: Met Trans, 10A, 1979, 439
42. M.W. Joosten, T.D. Lee, T. Goldenberg and J.P. Hirth: Hydrogen in Metals, I.M. Bernstein and A.W. Thompson eds., TMS-AIME, Warrendale, PA., 1980, 839
43. I.E. French, P.F. Weinrich and C.W. Weaver: Scripta Met., 13, 1979, 285
44. T.J. Kosco and A.W. Thompson: Scripta Met., 16, 1982, 1367
45. G.M. Pressouyre: Ph.D. Thesis, Carnegie Mellon University, 1977
46. I.G. Park and A.W. Thompson: Scripta Met., to be published.
47. J. Albrecht, A.W. Thompson and I.M. Bernstein: Met Trans., 10A, 1979, 1759
48. R. Garber, I.M. Bernstein and A.W. Thompson: Scripta Met., 10, 1976, 341
49. H. Cialone and R.J. Asaro: Hydrogen Effects in Metals, I.M. Bernstein and A.W. Thompson eds., TMS-AIME, Warrendale, PA, 1981, 767
50. A.J. West and M.R. Louthan Jr.: Met. Trans., 10A, 1979, 1675
51. J.D. Frandsen, N.E. Paton and H.L. Marcus: Scripta Met., 7, 1973, 409
52. J.D. Frandsen, N.E. Paton and H.L. Marcus: Met. Trans., 5, 1974, 1655

53. J.D. Frandsen and H.L. Marcus: *Scripta Met.*, 9, 1975, 1089
54. J.K. Tien, R.J. Richards, O. Buck and H.L. Marcus: *Scripta Met.*, 9, 1975, 1097
55. A.K. Zurek and H.L. Marcus: *Hydrogen in Metals*, I.M. Bernstein and A.W. Thompson eds., TMS-AIME, Warrendale, PA., 1980, 57
56. J.W. Swanson and H.L. Marcus: *Met. Trans.*, 9A, 1978, 291
57. J.K. Tien, O. Buck, R.C. Bates and S. Nair: *Scripta Met.*, 14, 1980, 583
58. O.A. Onyewuenyi and J.P. Hirth: *Met. Trans.*, 13A, 1982, 2209
59. J. Eastman, T. Matsumoto, N. Narita, F. Heubaum and H.K. Birnbaum: *Hydrogen Effects in Metals*, I.M. Bernstein and A.W. Thompson eds., TMS-AIME, Warrendale, PA., 1981, 397
60. J.E. Costa and A.W. Thompson: *Met. Trans.*, 13A, 1982, 1315
61. R.A. Oriani and P.H. Josephic: *Acta Met.*, 27, 1979, 997
62. T. Tabata and H.K. Birnbaum: *Scripta Met.*, 18, 1984, 231
63. C. Hwang and I.M. Bernstein: *Scripta Met.*, 16, 1982, 85
64. J. Volkl and G. Alefeld: *Diffusion in Solids - recent development*, A.S. Nowick and J.J. Burton eds., Acad. Press, NY, 1975
65. P. Shewman: *Diffusion in Solids*, McGraw-Hill, 1963
66. G.M. Pressouyre and I.M. Bernstein: *Acta Met.*, 27, 1979, 89
67. W.M. Robertson and A.W. Thompson: *Met. Trans.* 11A, 1980, 553
68. T. Asaoka, G. Lapasset, M. Aucouturier and P. Lacombe: *Corrosion-NACE*, 34, 1978, 39
69. R. Gibala: *Stress Corrosion Cracking and Hydrogen Embrittlement of Iron based Alloys*, R.W. Staehle, J. Hochmann, R.D. McCright and J.E. Slater eds., NACE-5, 1977, 244
70. R.A. Oriani: *Acta Met.*, 18, 1970, 147

71. A. McNabb and P.K. Foster: Trans. TMS-AIME, 227, 1963, 618
72. G.R. Caskey Jr. and W.L. Pillinger: Met. Trans., 6A, 1975, 467
73. R.C. Frank, C.W. Wert and H.K. Birnbaum: Met. Trans., 10A, 1979, 1627
74. A.J. Kurnick and H.H. Johnson: Acta Met., 28, 1980, 33
75. R.W. Lin and H.H. Johnson: Advanced Techniques for Characterizing Hydrogen in Metals, N. Fiore and B.J. Berkowitz eds., TMS-AIME, Warrendale, PA, 1981, 105
76. M. Iino: Acta Met., 30, 1982, 367
77. M. Iino: Acta Met., 30, 1982, 377
78. A.H. Cottrell: Dislocations and Plastic Flow in Crystals, Chapt. 4, Clarendon Press, Oxford, 1953
79. J.P. Hirth and J. Lothe: Theory of Dislocations, Chapt. 17, McGraw-Hill, NY, 1968
80. J.A. Donovan: Met. Trans., 7A, 1976, 1677
81. J.K. Tien, A.W. Thompson, I.M. Bernstein and R.J. Richards: Met. Trans., 7A, 1976, 821
82. L. Christodoulou, M.F. Stevens, J.J. Lewandowski, I.M. Bernstein and A.W. Thompson: Proc. 2nd Int. Conf. on Envir. Degrad. of Eng. Mater., VPI, VA, 1981, 161
83. P. Bastien and P. Azou: C.R. Acad. Sci. Paris, 232, 1951, 1845
84. P. Bastien and P. Azou: Proc. 1st World Met. Congress, ASM, Cleveland, 1951, 311
85. J.A. Donovan: Met. Trans., 7A, 1976, 145
86. M. Kurkela and R.M. Lantanision: Scripta Met., 13, 1979, 927
87. R. Otsuka and M. Isaji: Scripta Met., 15, 1981, 1153
88. M. Kurkela and R.M. Latanision: Scripta Met., 15, 1981, 1157

89. R.W. Lin and H.H. Johnson: *Scripta Met.*, 16, 1982, 1091
90. G.S. Frankel and R.M. Latanision: *ibid*, 1097
91. G.S. Frankel and R.M. Latanision: Proc. 9th Int. Cong. on Metallic Corrosion, Toronto, Canada, 1984, to be published.
92. C. Hwang and I.M. Bernstein: *Scripta Met.*, 17, 1983, 1299
93. M. Hashimoto and R.M. Latanision: Proc. 9th Int. Cong. on Metallic Corrosion, Toronto, Canada, 1984, to be published.
94. J.K. Tien, S.V. Nair and R.R. Jensen: Hydrogen Effect in Metals, I.M. Bernstein and A.W. Thompson eds., TMS-AIME, Warrendale, PA., 1980, 379
95. M. Hashimoto: Ph.D. Thesis, Massachusetts Institute of Technology, 1984
96. H. Yoshinaga and S. Morozumi: *Phil. Mag.*, 23, 1971, 1367
97. T. Tabata and H.K. Birnbaum: *Scripta Met.*, 17, 1983, 947
98. A. Kimura, H. Matsui and H. Kimura: *Mater. Sci. Eng.*, 58, 1983, 211
99. M.R. Louthan Jr.: *Scripta Met.*, 17, 1983, 451
100. I.M. Bernstein and A.W. Thompson: Atomistic of Fracture, Proc. of NATO Conf., R.M. Latanision and J.R. Pickens eds., Plenum Press, New York, 1981, 813
101. J.K. Tien, N.F. Panayotou and R.J. Richards: Proc. 2nd Int. cong. on Hydrogen in Metals, Paris, France, 1977, 2B11
102. J.K. Tien: Effect of Hydrogen on the Behavior of Materials, A.W. Thompson and I.M. Bernstein eds., TMS-AIME, NY, 1976, 309
103. H.H. Johnson and J.P. Hirth: *Met. Trans.*, 7A, 1976, 1543
104. J.P. Hirth and H.H. Johnson: Atomistics of Fracture, Proc. of NATO Conf., R.M. Latanision and J.R. Pickens eds., Plenum Press, New York, 1981, 771
105. S.V. Nair, R.R. Jensen and J.K. Tien: *Met. Trans.*, 14A, 1983, 385

106. C. Hwang and I.M. Bernstein: Proc. 3rd Int. Cong. on Hydrogen and Materials, Paris, France, 1982, 511
107. G.M. Pressouyre, J.P. Fidelle and R. Arnould-Laurent: Hydrogen Effects in Metals, I.M. Bernstein and A.W. Thompson eds., TMS-AIME, Warrendale, PA, 1980, 27
108. E.I. Taylor and C.F. Elam: Proc. Roy. Soc. (London), Ser.A, 112, 1926, 337
109. C.S. Barrett, G. Angel and R.F. Mehl: Trans ASM, 25, 1937, 792
110. N.K. Chen and R. Maddin: Trans AIME, 191, 1951, 927
111. R.P. Steijn and R.M. Brick: Trans ASM, 46, 1406, 1954
112. N.P. Allen, B.E. Hopkins and J.E. McLennan: Proc. Roy. Soc. (London), Ser.A, 234, 1956, 221
113. W.D. Biggs and P.L. Pratt: Acta Met., 6, 1958, 694
114. B. Edmondson: Proc. Roy. Soc. (London), Ser.A, 15, 1961, 176
115. D. Hull: Proc. Roy. Soc. (London), Ser.A, 274, 1963, 5
116. F.W. Noble and D. Hull: Phil. Mag., 12, 1965, 777
117. T. Taoka, S. Takeuchi and E. Furubayashi: J. Phys. Soc. Japan, 19, 1964, 701
118. E. Schmid and W. Boas: Plasticity of Crystals, London, Chapman & Hall, 1968
119. D.F. Stein and J.R. Low: Acta Met., 14, 1966, 1183
120. A.S. Keh: Phil. Mag., 12, 1965, 9
121. W.A. Spitzig: Acta Met., 18, 1970, 1275
122. A. Kelly and G.W. Groves: Crystallography and Crystal Defects, Addison-Wesley, Reading MA, 1970, 188
123. T.E. Mitchell, R.A. Foxall and P.B. Hirsch: Phil. Mag., 9, 1963, 1895

124. T.E. Mitchell and W.A. Spitzig: *Acta Met.*, 13, 1965, 1169
125. F. Guiu and P.L. Pratt: *Phys. Stat. Sol.*, 15, 1966, 539
126. T. Takeuchi: *Japan J. Appl. Phys.*, 8, 1969, 320
127. W.A. Spitzig and A.S. Keh: *Acta Met.*, 18, 1970, 611
128. A.S. Keh and Y. Nakada: *Canad. J. Phys.*, 45, 1967, 1101
129. T. Yamashita and Y. Taneda: *Trans. Iron and Steel Inst. Japan*, 10, 1970, 197
130. S. Ikeda: *J. Phys. Soc. Japan*, 27, 1969, 1564
131. J.E. Dorn and S. Rajnak: *Trans. Met. Soc. AIME*, 230, 1964, 1052
132. H. Saka, M. Doi and T. Imura: *J. Phys. Soc. Japan*, 29, 1970, 803
133. A.S. Keh and Y. Nakada: *Trans. Japan Inst. Metals*, 9 suppl., 1968, 876
134. G. Taylor and J.W. Christian: *Phil. Mag.*, 15, 1967, 873
135. A.S. Keh, W.A. Spitzig and Y. Nakada: *Phil. Mag.*, 23, 184, 1971, 829
136. T. Takeuchi: *Rev. Deform. Behav. Mater.*, 1, 1975, 117
137. Y. Nakada and A.S. Keh: *Acta Met.*, 16, 1968, 903
138. W.A. Spitzig: *Mater. Sci. Eng.*, 50, 1981, 229
139. H. Matsui, H. Kimura and S. Moriya: *Mater. Sci. Eng.*, 40, 1979, 207
140. E. Lunarska and Z. Wokulski: *Acta Met.*, 30, 1982, 2173
141. K. Oguri, S. Takaki and H. Kimura: *Mater. Sci. Eng.*, 53, 1982, 705
142. H. Matsui S. Moriya and H. Kimura: *Proc. 4th Int. Conf. on Strength of Metals and Alloys*, Nancy, France, 1976, 291
143. H. Kimura, H. Matsui and S. Moriya: *Scripta Met.*, 11, 1977, 473
144. H. Kimura and H. Matsui: *Scripta Met.*, 13, 1979, 221

145. D.S. Tomalin and C.J. McMahon Jr.: Proc. 2nd Int. Conf. on Strength of Metals and Alloys, ASM, Metals Park, Ohio, 1970, 134
146. R.J. Arsenault: Microplasticity, Interscience, New York, 1968, 91
147. H. Matsui, H. Kimura and A. Kimura: Mater. Sci. Eng., 40, 1979, 227
148. S. Moriya, H. Matsui and H. Kimura: Mater. Sci. Eng., 40, 1979, 217
149. E.W. Hart: Acta Met. 15, 1967, 351
150. I.H. Lin, J.P. Hirth and E.W. Hart: Acta Met., 29, 1981, 819
151. F.A. Nichols: Acta Met., 28, 1980, 663
152. A.K. Chakrabarti and J.W. Spretnak: Met. Trans., 7A, 1975, 733
153. A.K. Chakrabarti and J.W. Spretnak: Met. Trans., 7A, 1975, 737
154. C.A. Griffis and J.W. Spretnak: Met. Trans., 1, 1970, 550
155. J.W. Hutchinson and V. Tvergaard: Int. J. Mech. Soc., 22, 1980, 339
156. J.W. Rudnicki and J.R. Rice: J. Mech. Phys. Solids, 23, 1975, 371
157. R.J. Asaro and J.R. Rice: J. Mech. Phys. Solids, 25, 1977, 309
158. D. Peirce, R.J. Asaro and A. Needleman: Acta Met., 30, 1982, 1087
159. A.J. Bedford, A.L. Wingrove and K.R.L. Thompson: J. Austr. Inst. Metals, 19, 1974, 61
160. H.C. Rogers: Ann. Rev. Mater. Sci., 9, 1979, 283
161. F.A. McClintock, S.M. Kaplan and C.A. Berg: Int. J. Fract. Mech., 2, 1966, 614
162. H. Yamamoto: Inst. J. Frac. Mech., 14, 1978, 347
163. T.D. Lee, T. Goldenberg and J.P. Hirth: Fracture 1977, D.M.R. Taplin ed., vol.2, Pergamon, Oxford, 1977, 243
164. J. Lewandowski: Ph.D. Thesis, 1983, Carnegie-Mellon University

165. S. Chang: Ph.D. Thesis, 1981, Ohio State University
166. H.G.F. Wilsdorf: Mater. Sci. Eng., 59, 1983, 1
167. H.G.F. Wilsdorf: Acta Met., 30, 1982, 1247
168. R.N. Gardner and H.G.F. Wilsdorf: Met. Trans., 11A, 1980, 659
169. J. Ovejero Garcia, J. Chene and M. Aucouturier: Hydrogen in Metals, Proc. 2nd JIM Intern. Sym., Minakami, Gunma Pref., Japan, 1979, 525
170. Tuyen D. Le and B.E. Wilde: Current Solution to Hydrogen Problem in Steels, Proc. 1st Int. Conf., C.G. Interrante and G.M. Pressouyre eds., ASM, Metals Park, Ohio, 1982, 413
171. I.M. Bernstein and A.W. Thompson: Advanced Techniques for Characterizing Hydrogen in Metals, N.F. Fiore and B.J. Berkowitz eds., TMS-AIME, Warrendale, PA, 1981, 89
172. B.D. Cullity: Elements of X-Ray Diffraction: Addison-Wesley, Reading, MA, 1978
173. A.B. Greninger: Trans. AIME, 117, 1935, 61
174. J.C. Devaux, D. Dubois and J.B. Leblond: Current Solutions to Hydrogen Problems in Steels, C.G. Interrante and G.M. Pressouyre eds., ASM, Metals Park, Ohio, 1982, 45
175. J. Crank: The Mathematics of Diffusion, Oxford, Clarendon Press, 1956
176. M.A.V. Devanathan and Z. Stachurski: Proc. Roy. Soc. 270, 1962, 90
177. A.J. Kumnick and H.H. Johnson: Met. Trans., 5, 1974, 1199
178. F. Nakasato and I.M. Bernstein: Met. Trans., 9A, 1978, 1317
179. I.M. Bernstein and A.W. Thompson: Int. Metals Rev., 21, 1976, 269
180. I.M. Bernstein: Met. Trans., 1, 1970, 3143
181. A.S. Keh and S. Weissmann: Electron Microscopy and Strength of Crystals, New York, Interscience, 1963, 244

182. M. Bocek, D. Preininger and J. Bresser: Mater. Sci. Eng., 14, 1974, 67
183. G. Taylor and J.W. Christian: Phil. Mag., 15, 1967, 873
184. A. Lawley and H.L. Gaigher: Phil. Mag., 10, 1964, 15
185. A.S. Argon and S.R. Maloof: Acta Met., 14, 1966, 1449
186. M. Kurkela, G.S. Frenkel, R.M. Latanision, S Suresh and R.O. Ritchie: Scripta Met., 16, 1982, 455
187. W.J. McGregor Tegart: Elements of Mechanical Metallurgy, The Macmillan Co., NY, 1967
188. J.C.M. Li: Canad. J. Phys., 45, 1967, 493
189. R. Fuentes-Samaniego and J.P. Hirth: Phys. Stat. Sol.(b), 106, 1981, 359
190. T. Takeuchi: Trans. JIM, 9, 1968, 871
191. D.F. Stein and J.R. Low, Jr.: J. Appl. Phys. 31, 2, 1960, 362
192. J.P. Hirth and B. Carnahan: Acta Met., 26, 1978, 1795
193. J.P. Hirth: Met. Trans., 3, 1972, 3047
194. I. Gupta: Ph.D. Thesis, Columbia University, 1968
195. M.F. Stevens: Ph.D. Thesis, Carnegie-Mellon University, 1984
196. K. Hashimoto and M. Meshii: presented in 1984 TMS-AIME Fall Meeting
197. S. Mahajan: Acta Met., 23, 1975, 671
198. I.M. Bernstein: Scripta Met., 8, 1974, 343
199. S. Hinotani, F. Terasaki and F. Nakasato: Hydrogen in Metals, Proc. 2nd JIM Intern. Sym., Minakami. Gunma Pref., Japan, 1979, 421
200. T. Araki and Y. Kikuta: Hydrogen in Metals, Proc. 2nd JIM Intern. Sym., Minakami. Gunma Pref., Japan, 1979, 425.

201. K. Kitajima: Proc. Conf. Mechanism of Delayed Fracture Caused by Hydrogen, Tokyo, Japan, 1975, 35 (in Japanese)
202. F. Terasaki and F. Nakasato: Proc. Conf. Mechanism of Delayed Fracture Caused by Hydrogen, Tokyo, Japan, 1975, 165 (in Japanese)
203. A.S. Tetelman and W.D. Robertson: Trans. TMS-AIME, 224, 1962, 775

## Appendix A

### Model Calculation and Computer Programs

To establish the diffusion equation involving dislocation transport and trapping effects in addition to the lattice diffusion process, a small cube within the specimen, shown in Figure A-1, was chosen and a mass (hydrogen) balance on the cube was used to develop the diffusion equations. Only one dimensional flux will be considered in this model.

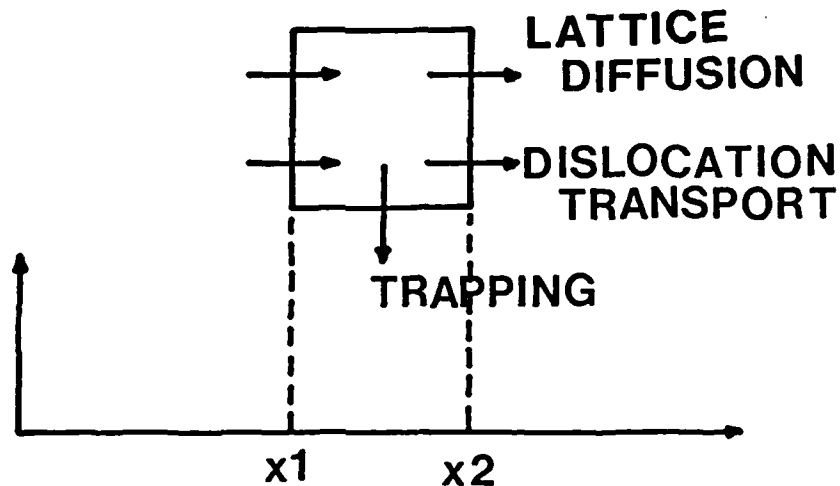


**Figure A-1:** A small cube within the specimen showing the constituents of its total hydrogen concentration.

There are three components which contribute to the total hydrogen concentration in the cube: lattice hydrogen concentration,  $C_L$ ; hydrogen concentration associated with mobile dislocations,  $C_m$ ; and hydrogen concentration associated with sessile dislocations,  $C_s$ . The hydrogen concentration associated with dislocations was assumed to have a Boltzmann's distribution:

$$C_m \text{ (or } s) = C_L * \exp(-E_B/kT). \quad (\text{A.1})$$

Within the cube, the changing rate of total hydrogen concentration,  $\partial C_{\text{tot}}/\partial t$ , is equal to

$$\frac{\partial C_{\text{tot}}}{\partial t} = \frac{\partial C_L}{\partial t} + \frac{\partial C_m \rho_m b^2}{\partial t} + \frac{\partial C_s \rho_s b^2}{\partial t}. \quad (\text{A.2})$$

Since mobile dislocation density,  $\rho_m$  is assumed constant.

$$\frac{\partial C_m \rho_m b^2}{\partial t} = \frac{\partial C_L}{\partial t} \rho_m b^2 \exp(-E_B/kT); \quad (\text{A.3})$$

and

$$\frac{\partial C_s \rho_s b^2}{\partial t} = \frac{\partial C_L \rho_s b^2}{\partial t} \exp(-E_B/kT); \quad (\text{A.4})$$

since  $\rho_s$  is a function of time. These variables have been defined in Section 5.5.

Now, consider the hydrogen flux flowing into this cube, which should be balanced with the changing rate of the total hydrogen concentration within the cube. The total hydrogen flux consists of lattice diffusion hydrogen flux and dislocation transport of hydrogen flux. The net lattice diffusion flux into the cube can be expressed as:

$$(-D \frac{\partial C_{L1}}{\partial t})_{x1} - (-D \frac{\partial C_{L2}}{\partial t})_{x2}, \quad (\text{A.5})$$

where  $C_{L1}$  and  $C_{L2}$  are the lattice hydrogen concentrations at  $x_1$  and  $x_2$  respectively (see Figure A-1). The net dislocation transport flux can be given as:

$$\rho_m b^2 v \exp(-E_B/kT) (C_{L1} - C_{L2}); \quad (\text{A.6})$$

so that, the net flux,  $J_{\text{net}}$  is the sum of Equation A.5 and Equation A.6.

Applying Fick's second law,

$$\frac{\partial C_{\text{tot}}}{\partial t} = - \frac{\partial J_{\text{net}}}{\partial x}, \quad (\text{A.7})$$

to equation A.2 and equation A.7, the mass balanced diffusion can then be given by:

$$\frac{\partial C_L}{\partial t} + \frac{\partial \rho_s C_L}{\partial t} b^2 \exp(-E_B/kT) + \frac{\partial C_L}{\partial t} \rho_m b^2 \exp(-E_B/kT) = D \frac{\partial^2 C_L}{\partial x^2} - \frac{\partial C_L}{\partial x} \rho_m b^2 v \exp(-E_B/kT). \quad (\text{A.8})$$

Based on equation A-8, trapping and transport effects can easily be separated, so that in the following, three cases will be examined: Trapping only, Transport only; and Combined Trapping and Transport.

### 1. Trapping only

The equation to be solved in this case is

$$\frac{\partial C_L}{\partial t} + \frac{\partial \rho_{\text{tot}} C_L}{\partial t} b^2 \exp(-E_B/kT) = D \frac{\partial^2 C_L}{\partial x^2} \quad (\text{A.9})$$

$$\text{where } \rho_{\text{tot}} = \rho_m + \rho_s. \quad (\text{A.10})$$

Using dimensionless variables:

$$C = C_L/C_0, \quad X = x/l \quad \text{and} \quad \tau = Dt/l^2 \quad (\text{A.11})$$

where  $C_0$  is the reference constant concentration,  $l$  is the specimen thickness and  $x$  is the distance, as shown in Figure A-1.  $C$ ,  $X$  and  $\tau$  are dimensionless variables.

Equation A-9 becomes

$$(a + \beta\tau) \frac{\partial C}{\partial \tau} = \frac{\partial^2 C}{\partial X^2} - \beta C, \quad (\text{A.12})$$

where

$$(a + \beta\tau) = 1 + \rho_{\text{tot}} b^2 \exp(-E_B/kT). \quad (\text{A.13})$$

### 2. Transport only

The equation to be solved in this case is

$$\frac{\partial C_L}{\partial t} + \frac{\partial C_L}{\partial t} \rho_m b^2 \exp(-E_B/kT) = D \frac{\partial^2 C_L}{\partial x^2} - \frac{\partial C_L}{\partial x} \rho_m b^2 v \exp(-E_B/kT). \quad (\text{A.14})$$

Using dimensionless variables in Equation A.11, Equation A.14 becomes

$$p \frac{\partial C}{\partial \tau} = \frac{\partial^2 C}{\partial x^2} - q \frac{\partial C}{\partial x} \quad (\text{A.15})$$

where

$$p = 1 + \rho_m b^2 \exp(-E_B/kT), \quad (\text{A.16})$$

$$q = \frac{\rho_m v l}{D} \exp(-E_B/kT). \quad (\text{A.17})$$

### 3. Combined Trapping and Transport

The equation to be solved is Equation A.8. Using dimensionless variables in equation A-11, Equation A.8 becomes

$$(\alpha + \beta \tau) \frac{\partial C}{\partial \tau} = \frac{\partial^2 C}{\partial x^2} - q \frac{\partial C}{\partial x} - \beta C \quad (\text{A.18})$$

where  $\alpha$ ,  $\beta$  and  $q$  were defined in Equations A.13 and A.17.

Equations A.12, A.15 and A.18 can then be solved by computer using finite difference method. The programs for doing these calculation are listed below:

Program 1. \*\*\*\*\*TRAPPING ONLY\*\*\*\*\*

```
dimension A(200),B(200),C(200),D(200),CI(200),CT(200)
OPEN(UNIT=12,DEVICE='DSK:',FILE='conc2.dat')
open(unit =3,device='dsk:',file='flux2.dat')
DT=0.01
DX=0.1
WRITE(5,25)DT,DX
25   FORMAT(1X,2F,/)

T=0.0
CI(1)=1.0
DO 30 J=2,11
```

```

      Y=DX*(J-1)
      CI(J)=1.0-Y
 30    CONTINUE
      WRITE(12,40)(CI(J), J=1,11)
 40    FORMAT(1X,5E)
      M=10
      DO 80 K=1,500,10
      T=DT*(K-1)
      DO 50 J=2,10
      A(J)=-DT/(DX**2)
      B(J)=1.0+((2*DT)/(DX**2)+(0.3125*DT))
      C(J)=A(J)
 50    CONTINUE
      D(2)=CI(2)-(CI(1)*A(2))
      DO 55 J=3,10
      D(J)=CI(J)
 55    continue
      CT(11)=0.
      call GAU(A,B,C,D,CT,M)
      CT(1)=1.
      write(12,40)(ct(J),J=1,11)
      flux=(CT(10)-CT(11))/DX
      write(3,57)T,FLUX
c57  format(1x,'time='E,5x,'flux='E)
 57  format(1x,5e)
      DO 70 J=1,11
      CI(J)=CT(J)
 70    CONTINUE
 80    CONTINUE
      STOP
      END
*****
***** SUBROUTINE GAU(XA,XB,XC,XD,TB,M)
      DIMENSION
      CXA(200),XB(200),XC(200),XD(200),TB(200),SB(200),SQ(200)
      SB(1)=XC(2)/XB(2)
      SQ(1)=XD(2)/XB(2)
      IA=M-2
      DO 12 J=2,IA
      SM=XB(J+1)-XA(J+1)*SB(J-1)
      SN=XD(J+1)-XA(J+1)*SQ(J-1)
      SB(J)=XC(J+1)/SM
      SQ(J)=SN/SM
 12    continue
      SQ(M-1)=(XD(M)-XA(M)*SQ(M-2))/(XB(M)-XA(M)*SB(M-2))
      TB(M)=SQ(M-1)
      do 16 K=1,IA
      J=M-K
 16    TB(J)=SQ(J-1)-SB(J-1)*TB(J+1)
      return
      end

Program 2.      *****TRANSPORT ONLY*****  

dimension A(200),B(200),C(200),D(200),CI(200),CT(200)
OPEN(UNIT=12,DEVICE='DSK:',FILE='conc3.dat')
open(unit =3,device='dsk:',file='flux3.dat')

```

```

DT=0.01
DX=0.1
WRITE(5,25) DT,DX
25   FORMAT(1X,2F,/)
T=0.0
CI(1)=1.0
DO 30 J=2,11
Y=DX*(J-1)
CI(J)=1.0-Y
30   CONTINUE
WRITE(12,40)(CI(J), J=1,11)
40   FORMAT(1X,5E)
M=10
DO 80 K=1,500,10
T=DT*(k-1)
DO 50 J=2,10
A(J)=-(DT/(DX**2))-((0.02*DT)/(2*DX))
B(J)=1.0+((2*DT)/(DX**2))
C(J)=-(DT/(DX**2))+((0.02*DT)/(2*DX))
50   CONTINUE
D(2)=CI(2)-(CI(1)*A(2))
DO 55 J=3,10
D(J)=CI(J)
55   continue
CT(11)=0.
CT(1)=1.
call GAU(A,B,C,D,CT,M)
write(12,40)(ct(J),J=1,11)
flux=(CT(10)-CT(11))/DX
write(3,57)T,FLUX
c57  format(1x,'time='E,5x,'flux='E)
57   format(1x,2e)
DO 70 J=1,11
CI(J)=CT(J)
70   CONTINUE
80   CONTINUE
STOP
END
*****
SUBROUTINE GAU(XA,XB,XC,XD,TB,M)
DIMENSION
CXA(200),XB(200),XC(200),XD(200),TB(200),SB(200),SQ(200)
SB(1)=XC(2)/XB(2)
SQ(1)=XD(2)/XB(2)
IA=M-2
DO 12 J=2,IA
SM=XB(J+1)-XA(J+1)*SB(J-1)
SN=XD(J+1)-XA(J+1)*SQ(J-1)
SB(J)=XC(J+1)/SM
SQ(J)=SN/SM
12   continue
SQ(M-1)=(XD(M)-XA(M)*SQ(M-2))/(XB(M)-XA(M)*SB(M-2))
TB(M)=SQ(M-1)
do 16 K=1,IA
J=M-K
16   TB(J)=SQ(J-1)-SB(J-1)*TB(J+1)
return

```

```
    end
```

```
Program 3.      ****COMBINED TRAPPING AND TRANSPORT****
```

```

dimension A(200),B(200),C(200),D(200),CI(200),CT(200)
OPEN(UNIT=12,DEVICE='DSK:',FILE='conc4.dat')
open(unit =3,device='dsk:',file='flux4.dat')
DT=0.01
DX=0.1
WRITE(5,25) DT,DX
25   FORMAT(1X,2F,/)
T=0.0
CI(1)=1.0
DO 30 J=2,11
Y=DX*(J-1)
CI(J)=1.0-Y
30   CONTINUE
WRITE(12,40)(CI(J), J=1,11)
40   FORMAT(1X,5E)
M=10
DO 80 K=1,500,10
T=DT*(k-1)
DO 50 J=2,10
A(J)--(DT/(DX**2))-((0.02*DT)/(2*DX))
B(J)=1.0+((2*DT)/(DX**2)+(0.3125*DT))
C(J)--(DT/(DX**2))+((0.02*DT)/(2*DX))
50   CONTINUE
D(2)=CI(2)-(CI(1)*A(2))
DO 55 J=3,10
D(J)=CI(J)
55   continue
CT(11)=0.
CT(1)=1.
call GAU(A,B,C,D,CT,M)
write(12,40)(ct(J),J=1,11)
flux=(CT(10)-CT(11))/DX
write(3,57) T,FLUX
c57  format(1x,'time='E,5x,'flux='E)
57  format(1x,2e)
DO 70 J=1,11
CI(J)=CT(J)
70   CONTINUE
80   CONTINUE
STOP
END
*****
SUBROUTINE GAU(XA,XB,XC,XD,TB,M)
DIMENSION
CXA(200),XB(200),XC(200),XD(200),TB(200),SB(200),SQ(200)
SB(1)=XC(2)/XB(2)
SQ(1)=XD(2)/XB(2)
IA=M-2
DO 12 J=2,IA
SM=XB(J+1)-XA(J+1)*SB(J-1)
SN=XD(J+1)-XA(J+1)*SQ(J-1)
SB(J)=XC(J+1)/SM
SQ(J)=SN/SM

```

```
12    continue
SQ(M-1)=(XD(M)-XA(M)*SQ(M-2))/(XB(M)-XA(M)*SB(M-2))
TB(M)=SQ(M-1)
do 16 K=1,IA
J=M-K
16  TB(J)=SQ(J-1)-SB(J-1)*TB(J+1)
return
end
```

## Appendix B

### Dislocation Line Direction and Burgers Vector Orientation Determination

#### B.1. Dislocation Line Direction Determination

To determine the primary dislocation line direction, two zone axes:  $(\bar{1}\bar{1}0)$  and  $(\bar{1}\bar{1}1)$  were used to perform trace analysis on dislocation images. The dislocation images obtained from these two zone axes, together with the orientation information from the diffraction patterns are shown in Figure B-1. It is clear that on the  $(\bar{1}\bar{1}0)$  zone axis, the dislocation line is parallel to the  $[1\bar{1}1]$  direction, and on the  $(\bar{1}\bar{1}1)$  zone axis, the dislocation line is parallel to the  $[\bar{2}\bar{1}\bar{1}]$  direction. Since the dislocation line is the intersection of two planes consisting of  $[\bar{1}\bar{1}0]$ ,  $[1\bar{1}1]$  directions and of  $[\bar{1}\bar{1}1]$ ,  $[\bar{2}\bar{1}\bar{1}]$  directions respectively, the calculation can be easily carried out to determine the dislocation line direction, as follows:

The vector product is taken to find the plane containing the  $[\bar{1}\bar{1}0]$  and  $[1\bar{1}1]$  direction:

$$[\bar{1}\bar{1}0] \times [1\bar{1}1] = [\bar{1}12]$$

Similarly, to find the plane containing  $[\bar{1}\bar{1}1]$  and  $[\bar{2}\bar{1}\bar{1}]$ ,

$$[\bar{1}\bar{1}1] \times [\bar{2}\bar{1}\bar{1}] = [0\bar{1}\bar{1}]$$

The dislocation line is then the intersection of  $(\bar{1}12)$  and  $(0\bar{1}\bar{1})$  planes, which is

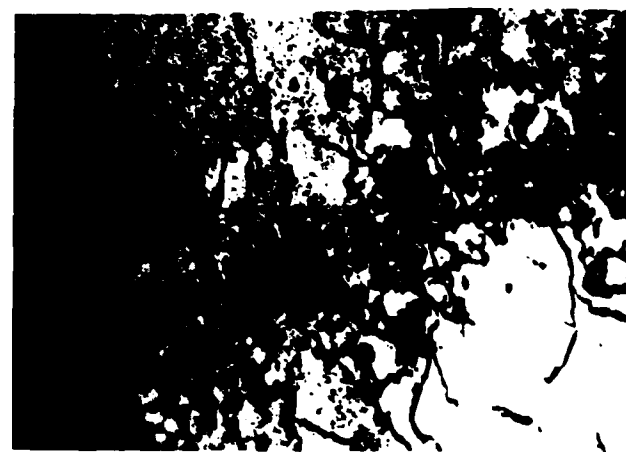
$$[\bar{1}12] \times [0\bar{1}\bar{1}] = [1\bar{1}1].$$

From Schmid's law, the primary slip system is predicted  $(\bar{1}12)-[1\bar{1}1]$ . Since the dislocation line is parallel to the Burgers vector, the dislocation is



$\begin{smallmatrix} \bar{1} & 1 \\ 1 & 1 \end{smallmatrix}$   $\begin{smallmatrix} 0 & 0 \\ 2 & \end{smallmatrix}$  Z.A.  $\bar{1}\bar{1}0$

(a)



$\begin{smallmatrix} 1 & 2 \\ 2 & 1 \end{smallmatrix}$   $\begin{smallmatrix} 1 & 1 \\ 2 & \end{smallmatrix}$  Z.A.  $\bar{1}\bar{1}1$

(b)

Figure B-1: TEM bright field image of dislocation tangled structure associated with spherical particles. (a)  $(\bar{1}\bar{1}0)$  zone axis, (b)  $(\bar{1}\bar{1}1)$  zone axis.

thus screw in character. It is also noted that since the dislocation line is on a  $(\bar{1}\bar{1}0)$  plane, which is also the single crystal foil surface plane in this particular case, the dislocation line direction can actually be determined by using the  $(\bar{1}\bar{1}0)$  zone axis alone, as can be easily recognized in the above calculation since the dislocation line direction projected on the  $(\bar{1}\bar{1}0)$  plane is the actual dislocation line direction.

### B.2. Burgers Vector Determination

It is obvious that within the dislocation tangled structure, there are other dislocations besides the primary dislocations, as can be seen in Figure B-2. Different  $\vec{g}$  vectors have been used to examine the  $\vec{g} \cdot \vec{b} = 0$  criterion, in order to differentiate and identify different Burgers vectors.

The images in Figure B-2 were taken from a zone axis close to  $[\bar{1}\bar{1}1]$ , however, a few degrees of tilting was added to obtain a good two beam condition for  $\vec{g}$  vector analysis. Dislocations with different Burgers vectors have been indicated in the Figures by A, B, and C, which are the three major distinguishable types of dislocations. The Burgers vectors for these was shown to be:

dislocation A:  $[111]$  (twinning direction)

dislocation B:  $[1\bar{1}1]$  (primary, antitwinning direction)

dislocation C:  $[\bar{1}11]$  (twinning direction)

The dislocation line directions for dislocations A and C can also be determined by the same technique used in the previous section. It was found that the majority of dislocations in these three systems are screws, because most of the dislocation lines in each case were parallel to its Burgers vector. The slip planes from the other two Burgers vector's dislocations, besides the primary slip dislocation, can also be determined from Schmid's law as shown in Figure 2-1. The results are listed as follows:

**Table B-1:** Three different slip systems identified in the dislocation tangled structure

| Dislocation | Slip Plane      | Burgers Vector | Schmid's Factor |
|-------------|-----------------|----------------|-----------------|
| A           | ( $\bar{2}11$ ) | [111]          | 0.21            |
| B           | ( $\bar{1}12$ ) | [111]          | 0.45            |
| C           | ( $1\bar{1}2$ ) | [111]          | 0.21            |

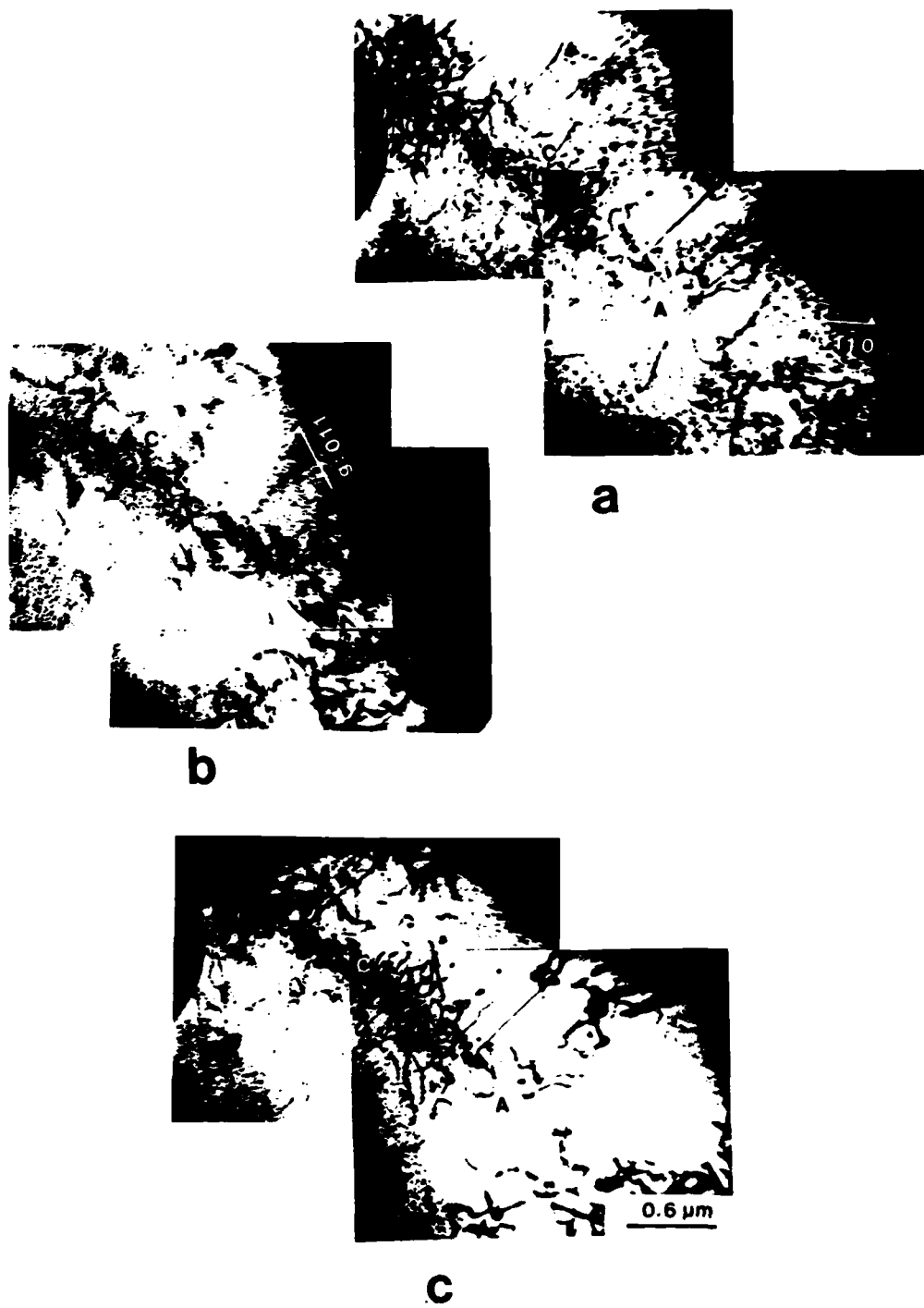


**Figure B-2:** TEM bright field image of dislocation tangled structure associated with spherical particles. (a)  $\vec{g} = [1\bar{1}0]$ , (b)  $\vec{g} = [011]$ , (c)  $\vec{g} = [101]$

SECURITY CLASSIFICATION OF THIS PAGE (When Data Entered)

| REPORT DOCUMENTATION PAGE   |  | READ INSTRUCTIONS BEFORE COMPLETING FORM  |  |
|---|--|---|--|
| 1. REPORT NUMBER<br>036-099-18  | 2. GOVT ACCESSION NO.<br><i>AD-A148143</i> | 3. RECIPIENT'S CATALOG NUMBER   |  |
| 4. TITLE (and Subtitle)<br><br>The Fundamentals of Dislocation Transport of Hydrogen in BCC Iron  |  | 5. TYPE OF REPORT & PERIOD COVERED<br><br>Technical Report  |  |
| 7. AUTHOR(s)<br><br>C. Hwang and I.M. Bernstein   |  | 6. PERFORMING ORG. REPORT NUMBER<br>NR 036-099-18<br>8. CONTRACT OR GRANT NUMBER(s)<br>N00014-75-C-0265 |  |
| 9. PERFORMING ORGANIZATION NAME AND ADDRESS<br>Dept. of Metallurgical Engineering & Mat. Science<br>Carnegie-Mellon University<br>Pittsburgh, PA 15213  |  | 10. PROGRAM ELEMENT, PROJECT, TASK AREA & WORK UNIT NUMBERS   |  |
| 11. CONTROLLING OFFICE NAME AND ADDRESS<br>ONR<br>Code 471 Arlington, VA 22217  |  | 12. REPORT DATE<br>October, 1984<br>13. NUMBER OF PAGES   |  |
| 14. MONITORING AGENCY NAME & ADDRESS (if different from Controlling Office)   |  | 15. SECURITY CLASS. (of this report)<br><br>Unclassified<br>15a. DECLASSIFICATION/DOWNGRADING SCHEDULE  |  |
| 16. DISTRIBUTION STATEMENT (of this Report)<br><br><table border="1"><tr><td>DISTRIBUTION STATEMENT A<br/><br/>Approved for public release;<br/>Distribution Unlimited</td></tr></table>  |  |   | DISTRIBUTION STATEMENT A<br><br>Approved for public release;<br>Distribution Unlimited |
| DISTRIBUTION STATEMENT A<br><br>Approved for public release;<br>Distribution Unlimited  |  |   |  |
| 17. DISTRIBUTION STATEMENT (of the abstract entered in Block 20, if different from Report)<br><br>Unlimited   |  |   |  |
| 18. SUPPLEMENTARY NOTES   |  |   |  |
| 19. KEY WORDS (Continue on reverse side if necessary and identify by block number)<br><br>microstructure, hydrogen embrittlement, hydrogen transport, traps, diffusion, dislocation dynamics, single crystals, work hardening strain localization.  |  |   |  |
| 20. ABSTRACT (Continue on reverse side if necessary and identify by block number)<br><br>The detailed characteristics of hydrogen transport by mobile dislocations during plastic deformation in bcc single crystal and polycrystal pure iron has been studied. Single crystals with a proper combination of surface orientation and tensile axis were used to separately study the hydrogen transport rates by screw, edge and mixed dislocations. This study was carried out experimentally through the use of a pair of sophisticated electrochemical cells incorporated with a _____ (continued) <span style="float: right;">7</span> |  |   |  |

specially constructed slow strain rate tensile testing device. The experimental uncertainties involved in the measurement of hydrogen flux have also been carefully analyzed and reduced to a minimum, so that the data obtained were able to be accurately interpreted. Parameters such as strain rate, lattice hydrogen concentration and temperature were varied to systematically study their functional relationships to dislocation transport.

It was found that qualitatively the hydrogen flux transported by dislocations intimately reflects the dislocation egression on the monitored crystal surface. Quantitatively, the hydrogen transport rate increases with decreasing strain rate; the edge kinks appeared to possess the greatest capability of transporting hydrogen at the lowest strain rate ( $1.6 \times 10^{-8}$  sec<sup>-1</sup>) employed. In addition, an insignificant effect of lattice hydrogen concentration on dislocation transport was observed, and was attributed to the kinetic nature of this transport process where equilibrium between hydrogen concentration on the dislocations and in the lattice is unlikely to be established. A minimal temperature effect on dislocation transport rate was also observed within a narrow temperature range, from 12°C to 78°C, consistent with the expectation that the extra thermal energy provided by increased temperature was too small to alter the interaction between hydrogen and mobile dislocations.

A competition between hydrogen transport by mobile dislocations and the trapping effect by newly generated sessile dislocations was studied, primarily by using polycrystal iron specimens. A simple model describing this combined effect of trapping and transport was also developed, which showed that transport can co-exist with the trapping even at the early strain history of the material when the dislocation multiplication rate is very high. However, the combined flux indicates that at small strains the trapping effect is dominant.

Dislocation structures formed with and without the presence of dislocation transported hydrogen in single crystals were also examined by transmission electron microscopy. The former case was found to greatly enhance the tendency for strain localization associated with inclusion particles, which are believed to be strong hydrogen traps. Dislocation structures associated with this strain localization phenomenon were analyzed; the origin of this localized strain was then studied and related to the role of hydrogen supersaturation due to dislocation transport. The consequent crack initiation associated with the interaction of hydrogen during straining was also studied. The complex and as yet incompletely understood interrelationships between dislocation transport of hydrogen, hydrogen supersaturation, strain localization and hydrogen-induced crack initiation were presented and discussed.

**END**

**FILMED**

**12-84**

**DTIC**